The Finite Element Ocean Model and its aspect of vertical discretization

Qiang Wang

Universität Bremen 2007

Universität Bremen

AWI
Alfred-Wegener-Institut
für Polar- und Meeresforschung
in der Helmholtz-Gemeinschaft

The Finite Element Ocean Model and its aspect of vertical discretization

Vom Fachbereich für Physik und Elektrotechnik
der Universität Bremen

zur Erlangung des akademischen Grades eines
Doktor der Naturwissenschaften (Dr. rer. nat.)
genehmigte Dissertation

von

Qiang Wang

1. Gutachter: Prof. Dr. D. Olbers
2. Gutachter: Prof. Dr. R. Gerdes

Abstract

The ocean bottom topography influences the general ocean circulation through a variety of processes. They can be of dynamical origin like topographic Rossby waves and topographic steering of the circulation through the bottom pressure torque, or of geometrical origin like sills and ridges that determine the pathways and properties of water masses. A faithful representation of the bottom topography and relevant physical processes is required in numerical ocean models. The ability of a model to resolve the bottom topography is mainly determined by the choice of vertical coordinates or vertical grids, which is one of the most important aspects of the model design.

This work is focused on a systematic study of the performance of different vertical grids in a set of numerical experiments performed with the Finite Element Ocean circulation Model (FEOM). This model supports several types of vertical discretization within a single numerical core, which allows the effects of vertical discretization to be isolated from other numerical issues.

A new version of FEOM is developed during the course of this work. Its discretization is based on unstructured triangular meshes on the surface and prismatic elements in the volume. The model uses continuous linear representation for the horizontal velocity, surface elevation, temperature and salinity, and solves the standard set of hydrostatic primitive equations. The characteristic-based split (CBS) scheme is used to suppress computational pressure modes and to stabilize momentum advection. With this split method the cost of solving the dynamic equations is reduced by uncoupling velocity from surface elevation. An algorithm for calculating pressure gradient forces is introduced to reduce pressure gradient errors on σ or hybrid grids. Different advection schemes are implemented and tested for tracer equations. The model as a whole is built with the hope of providing an efficient and versatile numerical tool for ocean sciences. It is capable of representing boundaries faithfully and allows flexible local mesh refinement without nesting.

The grids explored in this work include: the full cell z-level grid, the σ grid, the combined $z + \sigma$ grid and the modified z grids with partly or fully shaved bottom cells. Three numerical experiments are carried out to illustrate the performance of these types of grids. The first one deals with a steadily forced flow past an isolated seamount, the second one simulates topographic waves over sloping bottom in a rotating stratified channel, while the third one studies the dense water overflows in an idealized configuration. It is shown

that representing the bottom with shaved cell grids improves representation of ocean dynamics significantly compared to the full cell case. However, the σ and $z + \sigma$ grids are still better suited for representing bottom intensified currents and bottom boundary layer physics, as they can provide necessary vertical resolution in addition to continuous bottom representation. Taking into account the issue of pressure gradient errors, $z + \sigma$ grids are the promising approach for realistic simulations.

Intercomparison of our results with those published in the literature validates the performance of FEOM. With the development effort through the current work, FEOM has become a versatile tool for general oceanographic applications.

Contents

Chapter 1

Introduction

The understanding of the general ocean circulation is important for monitoring and predicting climatic changes. Both observations and numerical modelling are required to gain it and to be able to judge the role of the ocean in the Earth Climate System. The progress in numerical modelling of the ocean general circulation over the last decades is overwhelming and today many groups are able to simulate the general circulation of the world ocean at eddy resolving scales.

Growing attention is being payed to proper modelling of physical processes accompanying large-scale ocean dynamics in ocean general circulation models (OGCM). This requires careful selection of numerical algorithms and research into parameterizations of unresolved processes, and also involves the search for techniques capable of representing the important solid earth boundary of the ocean (including complex bottom topography and coastlines) in a physically relevant way. Continuous representation of coastlines and bottom topography is required in order to correctly set boundary conditions, as stepwise boundaries can lead to numerical artifacts and affect the ocean circulation on large time and spatial scales (Dupont et al., 2003; Adcroft and Marshall, 1998).

There are numerous situations where the bottom topography influences the ocean dynamics. Perhaps the best known example is the Antarctic Circumpolar Current (ACC), where the bottom formstress plays a decisive role in setting the momentum balance (Munk and Palmen, 1951; Hughes and Killworth, 1995; MacCready and Rhines, 2001; Borowski et al., 2002; Olbers et al., 2004, 2007). Other examples, to mention just a few, include the separation of the boundary currents like the Gulf Stream (Özgökmen et al., 1997; Tansley and Marshall, 2000), watermass transformation and thermohaline circulation in marginal seas (Spall, 2004), overflow processes in which dense water masses flow along and down slopes and get entrained by the ambient water (Price and Baringer, 1994), barotropic and baroclinic Rossby waves which are modified by topography can be important messengers in providing teleconnections in the ocean (Hallberg and Rhines, 1996; Ivchenko et al., 2006). Recent sensitivity studies by Losch and Heimbach (2007) show that scalar diagnostics such as

the transport through the Drake Passage, the strength of the North Atlantic
meridional overturning circulation, the Deacon cell and the heat transport are
sensitive to moderate changes in bottom topography as much as to changes in
surface forcing in a coarse resolution model.

Numerical modellers have long recognized the role of bottom topography.
The model's ability to accurately represent topography by modifying vertical
and/or horizontal discretization is one of the major concerns in model devel-
opment (Griffies et al., 2000a; Gorman et al., 2006). The current work has the
focus in this direction. It describes the recent further development of the Fi-
nite Element Ocean circulation Model (FEOM) and explores the performance
of several different vertical discretization supported by FEOM. Before formu-
lating the goals in more details, a brief review of relevant aspects of ocean
models is given below.

1.1   Vertical discretization in OGCMs

The three basic types of vertical discretization most commonly used in OGCMs
working on structured grids (finite difference (FD) and structured finite volume
(FV) models) are z-, σ- and isopycnal coordinates. Each of them has its own
advantages and disadvantages (Haidvogel and Beckmann, 1999; Willebrand
et al., 2001; Griffies, 2004). The choice of vertical coordinates or vertical grids
is one of the most important aspects in the design of an ocean circulation
model.

The first approach is to discretize the ocean into geopotential or z-levels.
Z-level ocean models have a long history of development since the pioneering
work of Bryan (1969) and Cox (1984). They are currently most widely used in
studies of ocean climate (Griffies et al., 2000a). They possess many attractive
advantages such as simple numerics, natural parameterization of the surface
mixing layer, and free of pressure gradient errors (to be explained later). How-
ever, standard z-level models with full cells represent the bottom topography
as "staircase" and thus have difficulties in resolving both steep and gentle
(with respect to the grid aspect ratio) bottom slopes with the currently afford-
able horizontal and vertical resolution (Adcroft et al., 1997; Pacanowski and
Gnanadesikan, 1998). Similarly, representing bottom boundary layer (BBL)
dynamics in z-level models is far from being straightforward (e.g., Beckmann
and Döscher, 1997; Winton et al., 1998; Ezer and Mellor, 2004).

Approaches to better represent bottom topography in the framework of z-
level models have been proposed by Maier-Reimer et al. (1993), Adcroft et al.
(1997) and Pacanowski and Gnanadesikan (1998). These methods employ
partial or shaved bottom cells as illustrated in Fig. 1.1, thus realizing a more
faithful representation of the bottom topography. However, even with these
methods, representing the bottom intensified flows still requires much effort in
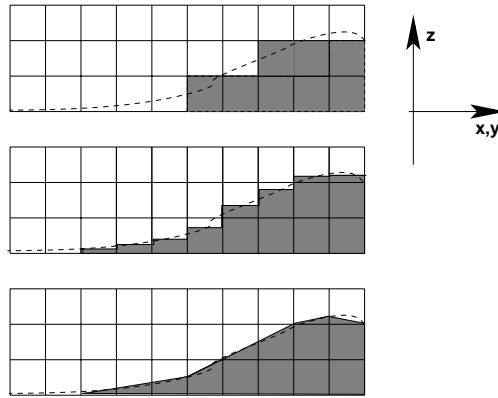z-level models.

Figure 1.1: Comparing representations of the ocean bottom in z-level models. Top: The *full cell* approach in which vertical size of cells does not change within the layer. Middle: The *partial cell* approach introduced to the ocean modelling by Maier-Reimer et al. (1993), Adcroft et al. (1997) and Pacanowski and Gnanadesikan (1998), in which the vertical resolution of the bottom cells can vary according to topographic features. Bottom: The *shaved cell* approach of Adcroft et al. (1997), in which bottom cells are cut to fit the topography. Both full and partial cells result in discontinuous representation of the bottom topography, whereas the shaved cells allow for a continuous (piecewise linear) bottom representation. The figure is reproduced from Griffies (2004).

The second type of vertical discretization is the so-called σ or terrain-following coordinate (Blumberg and Mellor, 1987; Haidvogel et al., 1991), which involves dividing the water column into a fixed number of vertical layers and then using a coordinate transformation of the water depth into an interval of (0, 1). Although σ coordinate models were originally designed mainly for coastal simulations, their applications have expanded to basin-scale and climate-scale modelling (Ezer and Mellor, 1997, 2000; Ezer, 1999, 2001; Haidvogel et al., 2000). Sigma models can accurately represent the bottom topography and BBL, and their vertical resolution can easily be refined locally. However, they suffer from pressure gradient errors (Haney, 1991; Beckmann and Haidvogel, 1993; Mellor et al., 1994, 1998), especially in regions of steep topography (see Greatbatch and Mellor, 1999; Ezer et al., 2002 for reviews of developments in σ coordinate models).

The third type of vertical discretization is dealing with isopycnal coordinates and involves dividing the water column into a stack of layers of constant density (Bleck and Smith, 1990). Isopycnal coordinate models respect adiabaticity of ocean dynamics in the interior of the ocean and provide a natural enhancement of resolution in regions where density gradients are tight. However, implementing the full equation of state and parameterizations of the surface boundary layer in realistic climate simulations adds complexity to such

models.

The performance of models based on different types of vertical discretization was studied under the framework of several projects coordinated between different research groups, for example, DYNAMO (Willebrand et al., 2001), DAMEE-NAB (Chassignet et al., 2000), and DOME (see `www.rsmas.miami.edu/personal/tamay/DOME/dome.html`). The advantages and disadvantages of the different types of vertical discretization were carefully assessed yet no single approach was qualified as ideal for wide-ranging oceanic applications in reality.

Each of the three vertical grids briefly described above can be optimal only in certain parts of the ocean and for describing specific ocean dynamics. The ocean surface boundary layer is well mixed in the vertical. A proper parameterization of physical processes in this layer is necessary and can be naturally realized in z-level grids. In the interior of the ocean the adiabatic process dominates and isopycnal coordinates are well suited to describe it. The bottom topography and BBL physics can be naturally and accurately represented with σ grids.

Several generalized or hybrid models have been developed (Gerdes, 1993a; Song and Haidvogel, 1994; Bleck, 2002; Mellor et al., 2002; Pietrzak et al., 2002) in the course of continuous ocean model development. These models try to combine benefits of different vertical discretization types within a single framework, and allow grids which are optimally tailored in different parts of the model domain. A brief introduction to the general-coordinate primitive equations and illustration of some features of particular coordinate formulations is given in Appendix A.

1.2   Using unstructured meshes

An alternative to the FD method is the finite element (FE) method, which allows a flexible unstructured discretization of the computational domain and local mesh refinements without nesting. A faithful representation of coastlines and bottom topography is natural with the FE method (for studies of the influence of coastline representation see Adcroft and Marshall, 1998; Dupont et al., 2003). FE formulation facilitates the use of hybrid vertical grids in one model, so models based on the FE method can be flexible tools for studying the effect of vertical grid discretization.

Since the early work of Fix (1975) on the use of the FE method in ocean modeling, most of the applications of FE ocean models have been focused on coastal and shelf regions (Lynch and Gray, 1979; Lynch et al., 1996; Platzman, 1981; Walters and Werner, 1989; Le Provost et al., 1995; Le Roux et al., 1998, 2000; Walters, 2005, 2006; Labeur and Pietrzak, 2005) and stationary-state ocean inverse problems (Brasseur, 1991; Schlichtholz and Houssais, 1999; Dobrindt and Schröter, 2003; Nechaev et al., 2003; Losch et al., 2005). Only a few

FE ocean general circulation models that employ unstructured meshes have been developed (Danilov et al., 2004; Ford et al., 2004a; White et al., 2007). The model described in this work has grown up from earlier efforts presented by Danilov et al. (2004, 2005).

Note that the FV method (e.g., Casulli and Walters, 2000; Chen et al., 2003; Ham et al., 2005; Stuhne and Peltier, 2006; Fringer et al., 2006) and the spectral element method (e.g., Haidvogel et al., 1997; Iskandarani et al., 2003) also offer the possibility of using unstructured meshes. Both the FE and FV methods are able to faithfully represent the geometry of the computational domain. The FE method generally provides better accuracy on unstructured grids, while the finite volume method is better suited to describe advectively dominated processes and facilitates using a wide palette of flux limiters which are an essential element of high-order advection schemes (see Zienkiewicz and Taylor, 2000 and Blazek, 2001 for an introduction into FE and FV techniques).

1.3 Pressure gradient errors

Pressure gradient errors in FD σ coordinate ocean (also atmospheric) models have been an issue of concern for a long time. The pressure gradient force in the horizontal momentum equation should take the horizontal gradient of pressure p along geopotential surfaces. It can be computed in the x, y, σ coordinates via

$$\frac{1}{\rho_0} \nabla_z p = \frac{1}{\rho_0} \nabla_\sigma p + \frac{g\rho}{\rho_0} \nabla_\sigma z, \tag{1.1}$$

where subscripts z and σ indicate that the gradient is taken along surfaces of constant z or σ, ρ and ρ_0 are density and its mean value, respectively. It turns out that the two terms on the right-hand side (rhs) of the above expression are almost compensating each other especially in the vicinity of steep topography. Due to finite accuracy of their discretization, significant errors could exist in the resulting pressure gradient forces.

Although the FE method features the attractiveness of natural treatment of boundary conditions, its application to ocean modelling is still facing many challenges (for a review see Pain et al., 2005). Formally, the FE method allows working with meshes unstructured in all three dimensions. This implies a full freedom in resolving the coastlines and bottom topography. In practice, however, using meshes unstructured in all three directions does not prove to be a good choice because of the associated problem of pressure gradient errors. These errors appear when the vertical discretization is not following the geopotential surfaces and the order of basis functions is not high enough to accurately approximate pressure (or density).

Many approaches have been tried to reduce the pressure gradient errors. The most commonly used remedies are removing a mean vertical density profile and smoothing bottom topography. In FD models, approaches including high

order differencing schemes (McCalpin, 1994; Chu and Fan, 1997), interpolation to z-levels (Kliem and Pietrzak, 1999), and the cubic spline reconstruction method (Shchepetkin and McWilliams, 2003) have been tested, and promising results have been obtained. For a comparison of different schemes see Ezer et al. (2002).

With the FE method, the question of how to deal with pressure gradient errors depends on the type of grids and basis functions used. The combination of linear basis functions is quite often used in 3D ocean modelling in order to obtain a computationally efficient model. Generally, pressure and density in realistic situations cannot be accurately interpolated with linear basis functions. However, using vertically aligned grids provides some flexibility for treating horizontal pressure gradient forces. The model of Lynch et al. (1996) is formulated on such grids and employ σ grids in the vertical. The approach to deal with pressure gradient errors in their model is to interpolate density field to fixed z-level grids, compute gradients of density on these level surfaces and then interpolate them back to σ grids. Ford et al. (2004a) used the idea of interchanging the order of integration and differentiation and the technique of discontinuous Galerkin method in the computation of pressure gradients in order to reduce pressure gradient errors on unstructured grids.

FEOM uses meshes with vertically aligned nodes too. Such meshes are unstructured only in the horizontal. Its early version (Danilov et al., 2004, 2005) employed tetrahedral elements within the z-level framework to resolve topography. The generation of tetrahedra can be controlled to have grid points at only two z-levels, this was done by putting nodes of surface grid to horizontal locations defined by the intersection of the specified z-levels and bottom topography. In this case, the pressure gradient errors are fully absent but this can only be done at the expense of very high resolution across regions of steep slopes (e.g., continental slopes).

A more general approach to deal with pressure gradient errors was desirable in order to make possible the use of generalized vertical grids with FEOM. The remedies commonly used in FD models, like removing a mean density profile and smoothing bottom topography can be used. But to rely solely on them is usually not enough in real oceanographic applications. This is because vertical density profiles change from region to region, and smoothing bottom topography could deteriorate the ocean dynamics. An approach using nonlocal interpolation and FD method is suggested to tackle the problem of pressure gradient errors in this work. It works with prismatic elements, and proves to have errors at a level that does not exceed the errors of the FD σ models that employ state-of-the-art techniques (see section 2.10).

1.4 Vertical grids supported by FEOM

With an efficient scheme of suppressing pressure gradient errors, σ grids are supported in FEOM. Additionally, other types of vertical discretizations become possible as explained below.

Besides the full cell z-level (Fig. 1.2a) and σ (Fig. 1.2b) grids, FEOM supports the $z + \sigma$ grids (Fig. 1.2c) and z-level grids with shaved bottom elements (Fig. 1.2d). A $z + \sigma$ grid combines a few σ levels close to the bottom with z-levels above them. The number of σ layers and level thicknesses can be adjusted depending on the application. For the shaved cell approach used in this work, we only permit one layer of deformed and shaved elements at the bottom for a direct comparison with shaved or partial cell approaches used in models formulated on structured grids. Using any number of layers with shaved elements is supported.

Any two adjacent elements always share the same face on a FE grid, so only the counterpart of the shaved cell approach shown in Fig. 1.1 can be realized, while true partial cells are not possible. Instead, shaved cell grids can be of two types in FEOM (Fig. 1.3). When the surface mesh is generated without a proper account for bottom topography, full cell elements (and vertical walls) might still be required in regions of steep slopes where the grid cell aspect ratio ($\Delta z/\Delta x$) is less than the local bottom slope (Fig. 1.3a). Such a grid is termed *partly shaved cell grid*. Clearly, the partly shaved cell grid follows closer the real bottom topography than the full cell grid (cf. 1.3a and 1.4a).

If the generation of surface meshes is controlled by increasing the horizontal resolution locally and adjusting the locations of surface nodes, the bottom topography can be represented piecewise linearly, even in regions of steep slopes (Fig. 1.3b). This is a *fully shaved cell grid*, or simply *shaved cell grid*. However, a caveat should be mentioned that designing such a grid for a realistic ocean topography may require introducing too small horizontal scales (for a fixed set of vertical levels), which may entail additional numerical difficulties. So in regions of steep slopes this approach is only applied when resolving small scale topographic features is really necessary. In regions of gentle slopes both modified z-level grids can accurately resolve the bottom topography and there is no essential difference between them (cf. 1.3a,b).

In contrast, Fig. 1.4 demonstrates that the full cell approach has difficulty in approximating both gentle and steep slopes, and the full cell grid misses the topographic variations over the gentle slopes almost completely. Even if the horizontal resolution is increased (with fixed vertical resolution) the full cell representation does not improve significantly.

In the current implementation FEOM does not support isopycnal grids. In principle, moving meshes to follow the isopycnal surfaces can be realized, but in practice doing it is not always beneficial. This is not only because moving meshes requires more CPU time, but also because using grids aligned with isopycnals in the framework of z coordinates can lead to the problem of pressure
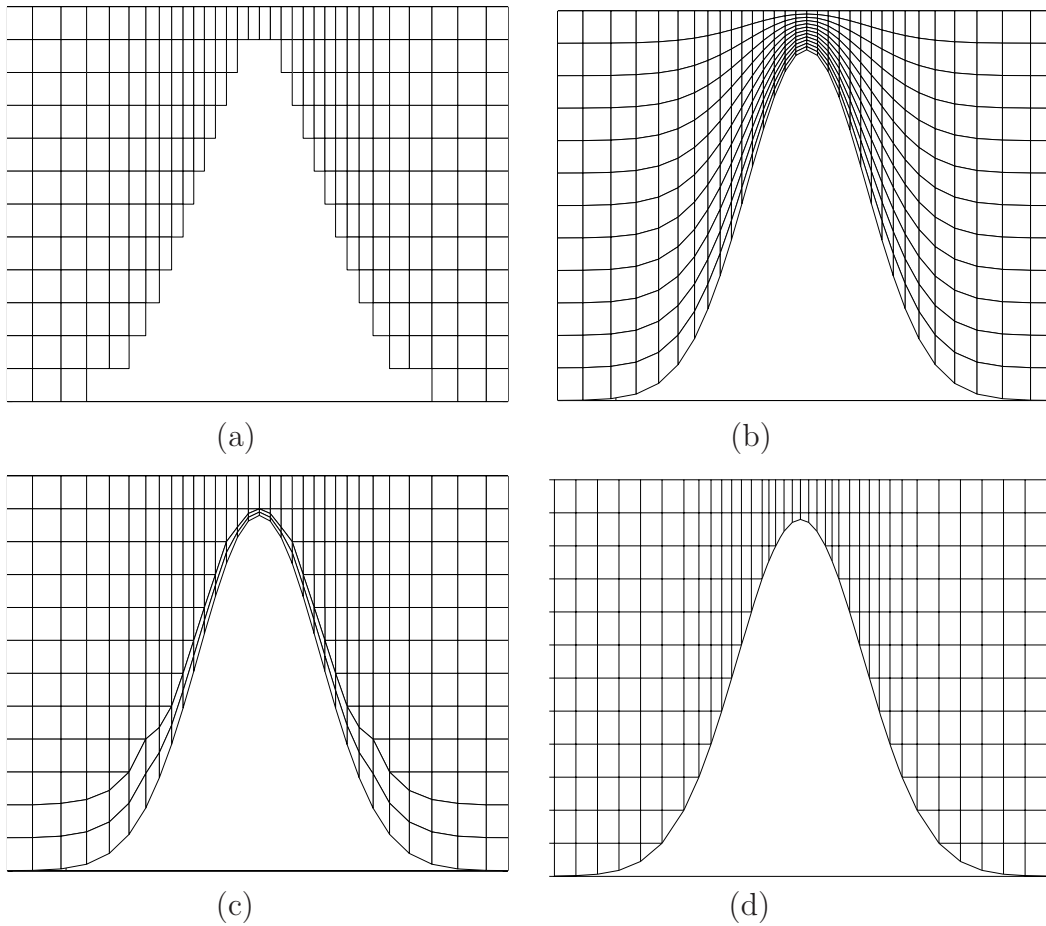
Figure 1.2: Examples showing (a) full cell, (b) sigma, (c) $z + \sigma$, and (d) shaved cell grids.

gradient errors as discussed above. A true isopycnal coordinate model based on coordinate transformation does not suffer from the difficulty in dealing with pressure gradients, at least in the case of linear equation of state. In FEOM neutral physics is treated with the isoneutral diffusion based on the small slope approximation (Gent and McWilliams, 1990; Griffies et al., 1998) and the skew diffusion scheme of Griffies (1998) as commonly used in z coordinate models. There is spurious diapycnal mixing associated with advection of temperature and salinity in z- or σ coordinate models (Griffies et al., 2000b). To efficiently reduce it without introducing too much computational load requires further research in the future.
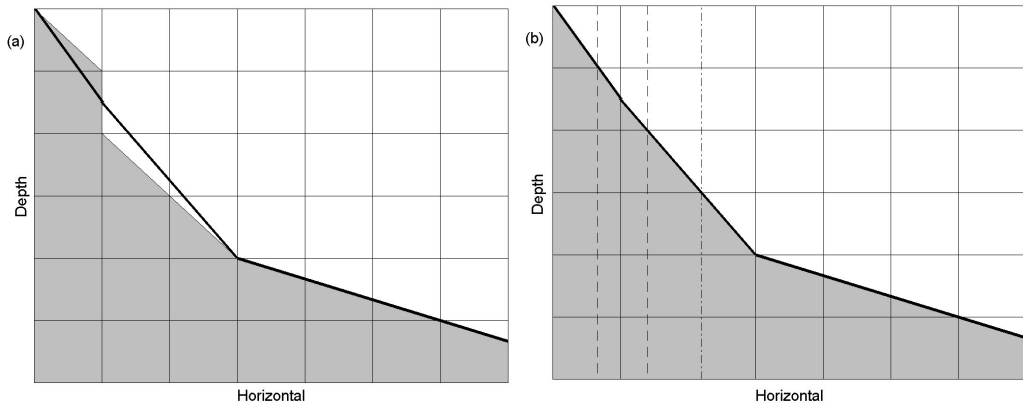
Figure 1.3: Comparison between bottom topography representation for (a) partly shaved cell and (b) fully shaved cell grids. The actual bottom is indicated with thick solid line, and the discretized bottom is indicated with gray color. Partly shaved bottom is obtained when the bottom slope exceeds the grid aspect ratio (a). By increasing the horizontal resolution locally (two new locations introduced instead the old one are shown by dash lines) and varying location of surface nodes (dot-dash line) the more accurate representation of topography is realized in (b).
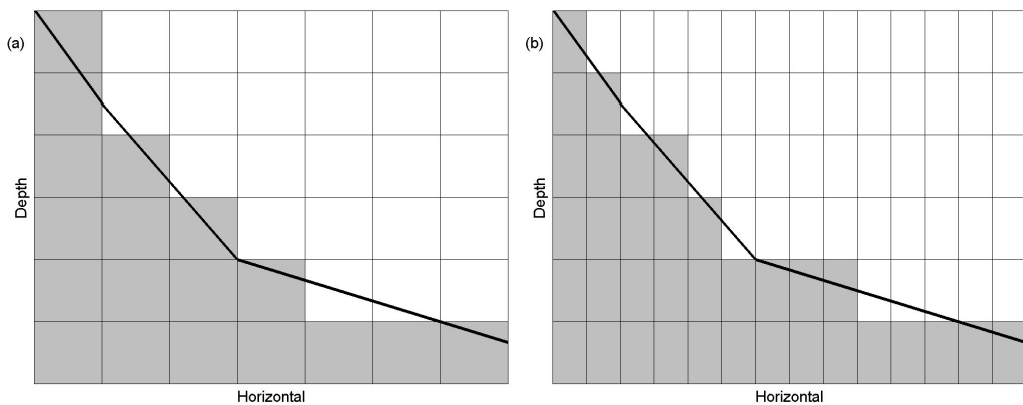
Figure 1.4: Actual and discretized bottom topography for the full cell approach using (a) low and (b) doubled horizontal resolution. Note that increasing horizontal resolution cannot improve bottom representation significantly in the full cell grid.

Remarks on numerics for realizing hybrid models

It is worth emphasizing that the philosophy of using σ grids in z-coordinate FE models like FEOM or ICOM (Ford et al., 2004a) is different from that in traditional σ coordinate FD models. The traditional sigma coordinate introduced

by Phillips (1957) for atmospheric modelling, which has later been adopted and developed in ocean modelling, is based on coordinate transformations (see Appendix A). The ocean or atmosphere is mapped to a regular rectangular computational domain. Modified equations under coordinate transformations are discretized and solved (for background materials see Haidvogel and Beckmann, 1999, and references therein).

The σ grids used in z coordinate FE models (see e.g., Ford et al., 2004a,b) are only named so to emphasize their similarity to the spatial discretization of traditional sigma models. Coordinate transformations are not necessarily required in order to permit using σ or hybrid grids in FE models. Grid type is set during the mesh generation stage while the model numerical core remains untouched. This property stems from the mathematical basis of the FE method. In the FE formulation, an equation for a given point is derived from the sum of contributions from neighbouring *elements*, which can have different shapes, thus allowing different vertical discretization. So FE models using z coordinate can be considered as a kind of hybrid models. However, since coordinate transform is not performed they are in reality only *hybrid-grid* models.

Remarks on dissipation operators

The lateral property gradients are taken along the surface of constant vertical coordinate, so σ coordinate FD models and z coordinate FE models using σ grids have different basic expressions of dissipation operators. This is an important issue in oceanographic applications. Lateral diffusion is naturally written in terms of along-σ operators in σ coordinate FD models. In order to avoid spurious diapycnal mixing, a transformation of along-σ diffusion to isoneutral or horizontal directions is desirable in many applications (e.g., Beckmann and Döscher, 1997).

In z coordinate FE models like FEOM, lateral diffusion is basically oriented along the horizontal direction even if σ or hybrid grids are used. This can also be suboptimal for some applications. Mixing is mainly going along isoneutral surfaces in the interior of the ocean, so the transformation of horizontal diffusion to be along the isoneutral direction, as used in structured z-level models, is also desirable in FE models. Accordingly, options of transforming dissipation to isoneutral and along-σ directions are introduced in FEOM.

1.5   Motivation and goals

The ability of a model to represent bottom topography on sigma, $z + \sigma$ and (partly) shaved cell grids is accompanied with the problem of pressure gradient errors. The main question is which approach provides the best choice. One issue here is that $z + \sigma$ and (partly) shaved cell grids supported by FEOM

have pressure gradient errors only within a small part of the computational domain. Do they achieve the full functionality of σ grids? How do they compare with FD structured grid models having a long history of development and application in ocean modelling?

The focus of the current work is centered on a systematic study of the performance of different types of grids with respect to simulations of a set of phenomena of oceanographic relevance. We exploit the fact that different grid types are supported by FEOM within the same numerical core. In this way the effect of vertical discretization can be explored in an almost clean form. The cases considered and described in more details below include an impulsively started flow past a Gaussian seamount, topographic waves in a rotating stratified channel, and dense water overflows.

An important task solved in this work is to provide FEOM with all the functionality of hybrid vertical grids. Doing this involved writing a new version of FEOM based on prismatic elements, implementing and testing the pressure gradient force algorithm for reducing pressure gradient errors, providing support for rotated diffusion (Gent and McWilliams, 1990; Griffies et al., 1998) and Gent-McWilliams (GM) parameterization (Griffies, 1998), and support for the quadrature integration of contributions from irregular elements. The total numerical approach of FEOM was put under scrutiny, and as a result, a numerically much more efficient code has been developed, which deviates substantially from the earlier version of FEOM. The characteristic-based split (CBS) formulation is now used to solve the dynamic equations. Namely, the split, or pressure projection, method is used to solve the momentum and vertically integrated continuity equations, with the characteristic-Galerkin (CG) method for the momentum advection. For tracer equations, three different schemes are available. With all the functionality added, FEOM was transformed to a versatile tool for ocean circulation modelling.

The set of problems considered in this work includes those that have being extensively studied and are sufficiently well documented, thus facilitating intercomparisons. The first set of experiments are based on the isolated seamount geometry. Using this setup, the formation of Taylor cap on an isolated seamount and the generation of internal lee waves over tall seamounts were investigated by Chapman and Haidvogel (1992, 1993), who examined the importance of parameters such as stratification and seamount height. The semispectral primitive equation model SPEM (Haidvogel et al., 1991; Beckmann and Haidvogel, 1993) was used in these studies. That model uses second-order finite differences in the horizontal and Chebyshev polynomials based on σ coordinates in the vertical.

This seamount geometry was also used by Adcroft et al. (1997) to demonstrate the improvement of simulation results by employing shaved cell method. The MITgcm (Marshall et al., 1997) used in their work is based on the finite volume method, and uses structured grids with z-level coordinates in the vertical. The eddy formation and shedding process was found to be better dupli-

cated when topography was represented with shaved cells than with full cells. Ford et al. (2004b) took this experiment setup to validate their nonhydrostatic finite element model (ICOM, Ford et al., 2004a), where intercomparison and examination of sensitivity to resolution were conducted. Their model employs hexahedral finite elements, and uses trilinear basis functions and a σ type of discretization in the vertical. The collection of these work based on the seamount geometry provides an excellent reference upon which an easy intercomparison with results from the current work can be made.

The simulation of stratified topographic waves in a rotating channel is taken as the second set of experiments. A similar model simulation has been taken by Pacanowski and Gnanadesikan (1998) to explore the effect of partial cell bottom representation on transient response using GFDL MOM. This is an ideal problem to demonstrate the effect of bottom representation, because there exist a linear analytical solution (Rhines, 1970), with which the dispersion relation from numerical model can be compared. Different vertical grid types (σ and shaved cell grids) which can easily represent a gentle slope accurately are expected to resolve this topographic wave well.

The DOME experiments was designed to investigate the dynamics of density driven down-slope overflows. This idealized model configuration, patterned mainly after the overflow in the Denmark Strait, set up a standard test bed for model intercomparisons. The properties of dense plume and entrainment have been studied with this configuration by Ezer and Mellor (2004); Ezer (2005); Legg et al. (2006); Tseng and Dietrich (2006) using different vertical grids in different ocean models, including the generalized-coordinate model POM (Mellor et al., 2002), the z-coordinate model MITgcm (Marshall et al., 1997), the isopycnal coordinate model HIM (Hallberg and Rhines, 1996), and the z-coordinate version of DieCAST (Dietrich/Center for Air Sea Technology ocean model, Dietrich, 1998). The DOME configuration is taken in the current work to compare the performance of five different vertical grids supported by FEOM.

The structure of the thesis is as follows. Chapter 2 describes the numerical approach adopted by FEOM to solve the primitive equations. It presents a relatively complete summary of what the current numerical core of FEOM is, and also explains, among other issues, the treatment of irregular elements, the implementation of the algorithm of computing pressure gradients, and the implementation of rotated dissipation operators. It also describes performance of different advection schemes existing in the current version of FEOM. Chapters 3 to 5 present intercomparison studies with problems outlined above. Their common result is that $z + \sigma$ grids are capable of producing results almost indistinguishable from pure σ grids. The partly and fully shaved cell approach is also a good choice, yet to approach the quality of solutions on σ grids, finer horizontal and vertical resolution is required, especially when BBL dynamics is of essential importance. The final chapter summarizes the main findings obtained for specific problems and concludes the work.

Chapter 2

Model numerics

This section presents the major numerical principles used in FEOM. Although the basic strategy of solving primitive equations in FEOM has very much in common with many ocean circulation models employing implicit free surface, the FE discretization introduces many specific issues that are to be explored. Mostly they are linked to the fact that FE discretization leads to systems of linear equations that are to be solved at every time step. For the sake of convenience, a list of symbols is given in Appendix B.

2.1 Governing equations

The hydrostatic primitive equations with the Boussinesq and traditional approximations are solved by splitting the dynamical and thermodynamical parts in FEOM. The dynamical part includes the momentum equations and the vertically integrated continuity equation:

$$\partial_t \mathbf{u} + \mathbf{v} \cdot \nabla_3 \mathbf{u} + f\mathbf{k} \times \mathbf{u} + \frac{1}{\rho_0}\nabla p + g\nabla\eta = \nabla \cdot A_h \nabla \mathbf{u} + \partial_z A_v \partial_z \mathbf{u}, \qquad (2.1)$$

$$\partial_t \eta + \nabla \cdot \int_{z=-H}^{z=\eta} \mathbf{u} \mathrm{d}z = 0, \qquad (2.2)$$

$$\partial_z p = -g\rho, \qquad (2.3)$$

where $\mathbf{v} \equiv (\mathbf{u}, w) \equiv (u, v, w)$ represents velocity in the spherical coordinate system, ρ and ρ_0 are density and its mean value, respectively, p is the hydrostatic (or baroclinic) pressure obtained through integrating the hydrostatic relation (2.3) from $z = 0$, η is the sea surface elevation, f is the Coriolis parameter, $\mathbf{k}$ is the vertical unit vector, the lateral and vertical viscosities are denoted by A_h and A_v, g stands for the gravitational acceleration, and ∇_3 and ∇ stand for 3D and 2D gradient or divergence operators, respectively. The upper limit of integration in (2.2) is set to 0 in the current version of FEOM, which implies that it uses linear free surface approximation. Consistent with this, the upper boundary of the computational domain is at $z = 0$, and surface

boundary conditions in the momentum and tracer equations are formulated there. Notice that the fresh water flux term is neglected in (2.2).

The physical domain can contain four types of boundaries $\partial\Omega = \cup_{i=1}^{4}\Gamma_i$, where $\Gamma_1 : \{z = 0\}$ is the ocean surface, $\Gamma_2 : \{z = -H\}$ stands for the ocean bottom, Γ_3 denotes the vertical rigid walls, and Γ_4 is the vertical open boundary. The open boundary line, which is the 2D projection of the vertical open boundary, is denoted by S_o.

The boundary conditions at the surface and the bottom are:

$$A_v\partial_z\mathbf{u} = \tau, \ p = 0 \text{ on } \Gamma_1, \tag{2.4}$$

$$A_v\partial_z\mathbf{u} + A_h\nabla H \cdot \nabla\mathbf{u} = C_d\mathbf{u}|\mathbf{u}| \text{ on } \Gamma_2, \tag{2.5}$$

where τ is the wind stress, and C_d is the bottom drag coefficient. On the vertical rigid walls, the boundary condition of no normal flow

$$\mathbf{u} \cdot \mathbf{n} = 0 \text{ on } \Gamma_3, \tag{2.6}$$

is always applied. Here $\mathbf{n}$ stands for the 2D normal unit vector. With no-slip boundary conditions, the tangential velocity on rigid walls is set to zero. For free-slip boundary conditions, the tangential component of the viscous stress is set to zero. Vertically integrated velocity in the direction normal to the boundary is prescribed at the open boundary line S_o, and the viscous stress is set to zero at the open boundary surface.

The vertical velocity is diagnosed via the continuity equation:

$$\partial_z w = -\nabla \cdot \mathbf{u}, \tag{2.7}$$

for which the kinematic boundary conditions at the surface and the bottom are:

$$w = \partial_t\eta + \mathbf{u} \cdot \nabla\eta \text{ on } \Gamma_1, \tag{2.8}$$

$$w = -\nabla H \cdot \mathbf{u} \text{ on } \Gamma_2. \tag{2.9}$$

The second term on the rhs of (2.8) disappears under the approximation of linear free surface. These kinematic boundary conditions are not independent. For example, by combining (2.2) and (2.7) and enforcing the bottom kinematic boundary condition (2.9), one can get the surface kinematic boundary condition (2.8).

In the thermodynamical part, the tracer equations are solved for potential temperature T and salinity S, and density ρ is computed via the equation of state (Jackett and McDougall, 1995):

$$\partial_t C + \mathbf{v} \cdot \nabla_3 C - \nabla \cdot K_h\nabla C - \partial_z K_v\partial_z C = 0, \tag{2.10}$$

$$\rho = \rho(T, S, p), \tag{2.11}$$

where C can be T or S, and K_h and K_v are lateral and vertical diffusivity, respectively. When rotated diffusion is used, diffusion is written in a more general form in terms of the diffusivity tensor.

The boundary conditions for tracers are:

$$K_v \partial_z C = -q \text{ on } \Gamma_1, \tag{2.12}$$

$$(\nabla C, \; \partial_z C) \cdot \mathbf{n}_3 = 0 \text{ on } \Gamma_2 \cup \Gamma_3, \tag{2.13}$$

where q is the surface flux for T or S, and $\mathbf{n}_3$ is the 3D unit vector normal to the respective surface. At the open boundary Γ_4 tracers are restored to climatological values.

2.2 Meshes and basis functions

2.2.1 Meshes

To solve the dynamic and thermodynamic equations given above, we will approximate continuous fields of variables by values at a finite set of discrete points within the computational domain. These discrete points form finite elements. The *mesh* (or grid) is the set of nodes together with the rules of forming elements. The main motivation for the use of the FE method is the usage of unstructured meshes. Prismatic elements are used in the current model. First a 2D unstructured triangular grid is generated on surface $z = 0$ and the model domain is divided into vertical columns. Then the columns are cut into layers to construct prismatic elements. In such a mesh, 3D nodes are always aligned vertically below corresponding 2D surface nodes. This allows a convenient and consistent realization of FE formulation of the hydrostatic primitive equations and an efficient and accurate method to calculate pressure gradient forces (to be discussed in details later).

The 2D triangular mesh can be generated with a variety of currently available free software packages, such as Triangle (Shewchuk, 1996) and Distmesh (Persson and Strang, 2004). The latter is used in the current work. The mesh quality, i.e. the extent to which the mesh triangles are close to equilateral triangles, can be quite high in many cases by using these generators. Care is required in order to provide smooth transition between subdomains with different resolution. The degree to which bottom topography can be resolved with shaved cells also depends on the surface mesh design.

Different vertical grids can be generated depending on how the model domain is cut in the vertical. If the domain is divided by geopotentially aligned levels, z-level grids are implemented. If the domain is divided vertically into an equal number of layers, σ grids are generated. Depending on applications, uniform or nonuniform placement of levels can be used in sigma grids. To create nonuniform σ layers in a convenient way, the transformation relation

proposed by Song and Haidvogel (1994) is adopted in the 3D generator:

$$z(x, y) = h_{min}\sigma + (h(x, y) - h_{min}) F(\sigma), \tag{2.14}$$

where h_{min} is the minimum depth inside the model domain, and

$$F(\sigma) = (1 - \theta_2)\frac{\sinh(\theta_1\sigma)}{\sinh(\theta_1)} + \frac{\theta_2}{2}\left[\frac{\tanh[\theta_1(\sigma + 1/2)]}{\tanh(\theta_1/2)} - 1\right],$$

where θ_1 and θ_2 are parameters controlling the vertical level stretching, and $-1 \leq \sigma \leq 0$ is discretized uniformly into desired number of vertical layers. For large θ_1, the vertical layers crowd near the surface, and when θ_2 approaches 1, resolution near to the bottom boundary is enhanced. Note once again that there is no coordinate transformation in our model, and (2.14) is only used to simplify the σ grid generation.

In the $z + \sigma$ and (partly) shaved cell grids there could be degenerated prism elements, which contain five or four nodes instead of six nodes of standard prisms. This requires a technique which deals with degeneration, it will be briefly described later.

2.2.2   Basis function expansions

In the FE formulation, variables are approximated as sums over a finite set of basis functions. We employ the combination of piecewise linear basis functions in two dimensions for surface elevation and in three dimensions for velocity and tracers. Because continuous linear basis functions are used for both the horizontal velocity and elevation ($P_1 - P_1$ discretization), stabilization for pressure modes is required. Details of the stabilization method are given further in section 2.4.

The numerical approximations of velocity and tracers are represented using a finite set of basis functions denoted by $\{N_j\}$:

$$\mathbf{u} \simeq \sum_{j=1}^{N}(u_j, \ v_j)N_j, \quad C \simeq \sum_{j=1}^{N}C_jN_j, \tag{2.15}$$

and sea surface elevation is represented using 2D basis functions $\{M_j\}$:

$$\eta \simeq \sum_{j=1}^{M}\eta_jM_j. \tag{2.16}$$

The basis functions N_j and M_j are equal to one at node j and go linearly to zero at neighbouring nodes. They equal zero outside the stencil formed by neighbor nodes. With adopted spatial discretization and basis functions, N

and M are the total numbers of 3D and 2D mesh nodes, respectively. The vectors representing nodal values are defined as:

$$
\begin{aligned}
\bar{\mathbf{u}} &= [u_1, \cdots, u_j, \cdots, u_{\mathrm{N}}, v_1, \cdots, v_j, \cdots, v_{\mathrm{N}}]^{\mathrm{T}} \\
\bar{C} &= [C_1, \cdots, C_j, \cdots, C_{\mathrm{N}}]^{\mathrm{T}} \\
\bar{\eta} &= [\eta_1, \cdots, \eta_j, \cdots, \eta_{\mathrm{M}}]^{\mathrm{T}}
\end{aligned}
\tag{2.17}
$$

The length of the velocity vector $\bar{\mathbf{u}}$ is 2N, as it combines u and v components of the horizontal velocity, $\bar{C}$ is a vector of length N, and $\bar{\eta}$ is a vector of length M.

Because 3D nodes are generated by dropping vertical lines starting from the surface 2D nodes, the 2D basis functions $\{M_j\}$ and the 3D basis functions $\{N_j\}$ have the following properties:

$$
\sum_{j \in J} N_j = M_J, \quad \sum_{j \in J} \frac{\partial N_j}{\partial z} = 0,
\tag{2.18}
$$

where $j \in J$ means that the sum is over basis functions associated with 3D nodes aligned vertically with 2D node J. This basic property is commonly required in hydrostatic ocean models based on the FE method as in the early version of FEOM (Danilov et al., 2004). The necessity to maintain this property will be clarified in section 2.5.

2.2.3   Elements with variable numbers of nodes

The FE formulation involves the projection of governing equations on an appropriate set of test functions, which implies taking integration over prisms and triangles. Since prisms can be deformed or shaved in general cases, the coordinate transformation technique is required to facilitate the integration, which maps a given prismatic element into the standard prism as shown in Fig. 2.1. This standard prism is often called the parent domain. The coordinates of a point in a prismatic element in the physical domain (Ω) are related to the coordinates of a point in the parent domain with the mapping:

$$
\boldsymbol{x}(\boldsymbol{\xi}) = \sum_{a=1}^{6} N_a^e(\boldsymbol{\xi}) \boldsymbol{x}_a^e,
\tag{2.19}
$$

where $\boldsymbol{x}_a^e$, $a = 1, ..., 6$ denotes the locations of the six nodal points of the prismatic element Ω^e, $\boldsymbol{\xi}$ represents the coordinates in the parent domain, the so-called natural coordinates, and N_a^e is the basis function within the element Ω^e for its node a. They are the same basis functions as those used to interpolate tracer and horizontal velocity fields, and they have been introduced as $\{N_i\}$ in equation (2.15) using global index instead of elemental notations. When such interpolation functions are used, the element is termed isoparametric.
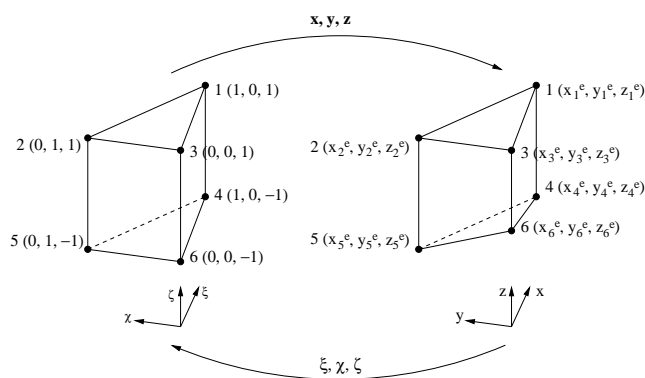
Figure 2.1: Schematic explanation of coordinate transformation. The left prism is the parent domain, and the right one is the element in physical coordinates (x, y, z).

Using isoparametric elements generally helps to satisfy convergence conditions (Hughes, 1987).

With the basic concept of mapping given above, the implementation of the aforementioned technique of *degeneration* to prisms with coalesced nodes is to be explained below. Fig. 2.2 shows an example of a degenerated prism. Nodes 3 and 6 are coalesced and $\boldsymbol{x}_3^e = \boldsymbol{x}_6^e$. In this case the mapping defined in (2.19) is

$$
\begin{aligned}
\boldsymbol{x} &= \sum_{a=1}^{6} N_a^e \boldsymbol{x}_a^e \\
&= N_1^e \boldsymbol{x}_1^e + N_2^e \boldsymbol{x}_2^e + (N_3^e + N_6^e)\boldsymbol{x}_3^e + N_4^e \boldsymbol{x}_4^e + N_5^e \boldsymbol{x}_5^e \qquad (2.20) \\
&= \sum_{a=1}^{5} N_a^{e,\text{new}} \boldsymbol{x}_a^e,
\end{aligned}
$$

where

$$
N_a^{e,\text{new}} = \begin{cases} N_a^e & a = 1, 2, 4, 5 \\ N_a^e + N_{a+3}^e & a = 3 \end{cases} \qquad (2.21)
$$

which defines the new basis functions for the five node element in Fig. 2.2.

The integration over elements is performed in their parent domain. The Jacobian of the mapping $j = \det(\partial \boldsymbol{x}/\partial \boldsymbol{\xi})$ enters then into integrands due to the coordinate transformation, and it is also required for computing derivatives with respect to physical coordinates. The Jacobian determinant vanishes at the coalesced nodes, but this does not create problems as appropriate quadrature rules are used for computations. The quadrature points are always selected where the coordinate mapping is not singular, and it can be shown that convergence conditions are still satisfied (Hughes, 1987).
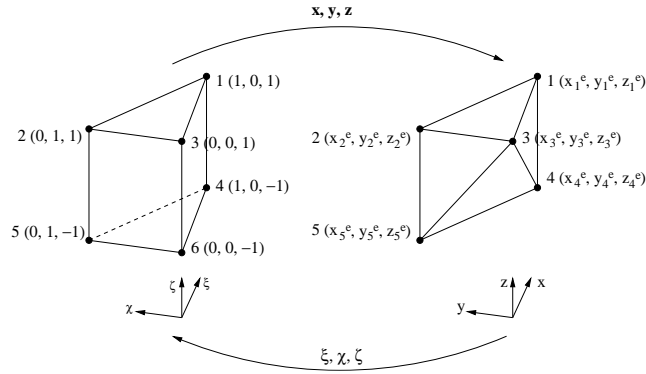
Figure 2.2: The same as Fig. 2.1 but for the case when there are coalesced nodes.

2.3 Solution method

2.3.1 Problems and strategy

The dynamical part

We obtain the discretized equations by the Galerkin method, which implies that the test functions that are used to project the equations coincide with the basis functions. It ensures that the residual of equations is orthogonal to any of the basis functions, in this sense one gets optimal discretization. However, solving the incompressible flow problem described by equations (2.1), (2.2) and (2.3) with the standard Galerkin method has two major numerical problems.

The first one is associated with advection-dominated flows in which the cell Reynolds number is high. In such cases dispersion errors in advective terms may lead to spurious oscillations on the grid scale, which can severely degrade solutions. This problem is common for FD models too, it is typically circumvented by using some high-order or upwind advection schemes. In the FE case, it can be solved either by using different spaces for test and basis functions, the so-called Petrov-Galerkin method, or by introducing some stabilization terms in the FE formulation.

The second problem is that the basis functions for velocity and surface elevation (pressure in the nonhydrostatic case) should meet the so-called LBB condition (Ladyzhenskaya, 1969; Babuska, 1973; Brezzi, 1974), otherwise spurious surface elevation modes can appear and lead to instability. In FD models staggered grids (Arakawa, 1966) are usually used to avoid a problem of the similar kind. The basis functions used in our model do not satisfy this condition, so standard Galerkin method can not be applied directly to solve the system of (2.1) and (2.2).

Different stabilization methods have been suggested to overcome these problems in the FE community. In the tetrahedral version of FEOM (Danilov

et al., 2004) the Galerkin least-squares (GLS) method (Codina and Soto, 1997) has been used to resolve both difficulties. To achieve a more consistent and efficient solution with the aforementioned two numerical difficulties also resolved, the CBS scheme is employed in the current work (for reviews see Zienkiewicz et al., 1999; Nithiarasu et al., 2006, and references therein).

This split method belongs to the family of projection methods, in which the cost of solving the dynamical part is reduced by uncoupling the velocity from the pressure (surface elevation in our hydrostatic case). The LBB condition is circumvented by the classical splitting technique, and the advection is stabilized by using discretization along the characteristics, i.e., the CG method. Comparisons between the CBS method and subgrid scale (SGS) methods (Codina and Zienkiewicz, 2002; Codina et al., 2006) show that these different formulations display similar stabilization mechanisms provided the stabilization parameter of the SGS methods is identified with the time step of the CBS approach. Both explicit and implicit time stepping can be applied to the CBS method, and the resulting discrete equations can be solved efficiently.

The thermodynamical part

In the ocean the evolution of temperature and salinity is mainly governed by advection, indicated by large cell Peclet numbers. So the same numerical problem as in solving momentum equations with large cell Reynolds numbers is also encountered here, hence stabilization is required. The CG method can also be employed to solve the tracer equations, resulting in mass matrix (matrix of the time derivative operator) equations which can be efficiently solved. An alternative advection scheme using the (explicit) flux-corrected transport (FCT) method (Löhner et al., 1987) is also implemented in the current model. This is motivated by some applications in which eliminating overshoots is crucial. The GLS scheme implemented by Danilov et al. (2004) is maintained as an optional scheme in the current model.

2.3.2   Characteristic Galerkin method

The CG method Zienkiewicz and Taylor (2000) will be briefly explained here, leaving its implementation to the primitive equations to be described in the next section. The basic idea is to discretize equations in time along characteristics and apply FE discretization afterwards.

For simplicity the one dimensional advection equation

$$\partial_t \phi + U \partial_x \phi - Q = 0 \tag{2.22}$$

will be used here to derive the CG formulation, and its extension to multidimensional problems is straightforward. In equation (2.22), ϕ could denote one of the velocity components or one tracer field, U is the one dimensional velocity, and Q contains other terms that exist in momentum or tracer equations.
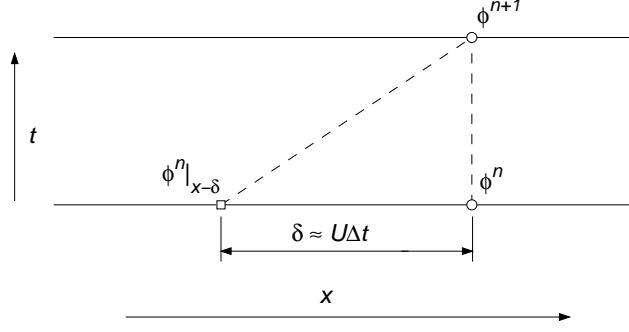
Figure 2.3: Schematic explanation for the characteristic Galerkin procedure.

If the coordinate system is 'advected' with velocity U, that is, along the *characteristics* of the problem described by equation (2.22), this equation can be written as

$$\frac{\partial \phi}{\partial t}(x'(t), t) - Q(x') = 0, \tag{2.23}$$

where x' denotes a moving coordinate in which the advection term disappears, and Q represents averaged quantities along the characteristic. The time discretization of (2.23) along the characteristic (Fig. 2.3) gives

$$\frac{1}{\Delta t}\left(\phi^{n+1} - \phi^n|_{(x-\delta)}\right) \approx \theta Q^{n+1} + (1-\theta)Q^n|_{(x-\delta)}, \tag{2.24}$$

where θ is equal to zero for explicit forms, and between zero and unity for semi- and fully implicit forms.

Taking Taylor expansion one gets

$$\phi^n|_{(x-\delta)} \approx \phi^n - \delta\frac{\partial \phi^n}{\partial x} + \frac{\delta^2}{2}\frac{\partial^2 \phi^n}{\partial x^2} + O(\delta^3), \tag{2.25}$$

$$Q|_{(x-\delta)} \approx Q^n - \delta\frac{\partial Q^n}{\partial x} + O(\delta^2), \tag{2.26}$$

where δ is the distance traveled by the particle in the x direction (Fig. 2.3):

$$\delta = \bar{U}\Delta t. \tag{2.27}$$

Different approximations can be applied to $\bar{U}$, the average velocity along the characteristic, which can lead to different stabilization terms, but the difference is small (Zienkiewicz and Taylor, 2000). We take the approximation

$$\bar{U} = \frac{U^{n+1} + U^n|_{x-\delta}}{2}, \tag{2.28}$$

where the last term can be approximated using the Taylor expansion:

$$U^n|_{(x-\delta)} \approx U^n - \Delta t U^n\frac{\partial U^n}{\partial x} + O(\Delta t^2). \tag{2.29}$$

Substituting (2.25)-(2.29) into (2.24), and taking $\theta = 0.5$, we have

$$
\begin{aligned}
\frac{\phi^{n+1} - \phi^n}{\Delta t} \quad = \quad &-U^{n+1/2}\frac{\partial \phi^n}{\partial x} + \frac{\Delta t}{2}U^n\frac{\partial U^n}{\partial x}\frac{\partial \phi^n}{\partial x} + \frac{\Delta t}{2}U^{n+1/2}U^{n+1/2}\frac{\partial^2 \phi^n}{\partial x^2} \\
&+Q^{n+1/2} - \frac{\Delta t}{2}U^{n+1/2}\frac{\partial Q^n}{\partial x},
\end{aligned}
\tag{2.30}
$$

where

$$
U^{n+1/2} = \frac{U^{n+1} + U^n}{2}, \ \text{ and } Q^{n+1/2} = \frac{Q^{n+1} + Q^n}{2}.
\tag{2.31}
$$

Note that (2.30) is second order accurate and higher-order terms have been neglected. To get the explicit scheme with respect to U a further approximation

$$
U^{n+1/2} = U^n + O(\Delta t)
\tag{2.32}
$$

will be taken in second order terms, leading to the final form of the CG formulation

$$
\frac{\phi^{n+1} - \phi^n}{\Delta t} = -U^n\frac{\partial \phi^n}{\partial x} + Q^{n+\theta} + \frac{\Delta t}{2}U^n\frac{\partial}{\partial x}\left[U^n\frac{\partial}{\partial x}\phi^n - Q^{n+\theta}\right].
\tag{2.33}
$$

Here the Q term is written with the superscript θ to indicate that different temporal forms could be required by different terms in the momentum equation. For example, the surface elevation term often requires the fully implicit form to damp fast gravity waves. The overall temporal accuracy of the equation depends on the temporal form of Q.

This semi-discrete form (2.33) for tracer equations can be solved directly after applying standard Galerkin method (hence the name of CG method in a whole), but for the momentum equation the projection method will be firstly employed before taking spatial discretization in order to stabilize pressure modes. The solution of momentum and tracer equations is described in details in the following sections.

The CG method is identical to the second-order Taylor Galerkin approach for scalar variables (also for each velocity component) with respect to the final formulation, but the former has sound mathematical justification according to Zienkiewicz and Taylor (2000). Both methods are based on taking temporal discretization using Taylor expansion before applying spatial discretization.

With this method the leading-order error in an advection equation is second order and generates numerical dispersion, and the permissible time step is limited by $|\mu| \leq 1/\sqrt{3}$ in the one dimensional case, where $\mu = U\Delta t/\Delta x$ is the Courant number (Durran, 1999).

2.4   Solving for velocity and sea surface elevation

2.4.1   Solution procedure

After employing the CG procedure to the momentum equation (2.1), the semi-discrete equation is:

$$\frac{\mathbf{u}^{n+1} - \mathbf{u}^n}{\Delta t} = -(\mathbf{v} \cdot \nabla_3 \mathbf{u})^n + Q^{n+\theta} + \frac{\Delta t}{2} \mathbf{v}^n \cdot \nabla_3 \left[(\mathbf{v} \cdot \nabla_3 \mathbf{u})^n - Q^{n+\theta} \right], \quad (2.34)$$

where Q represents the terms except for the time derivative and advection terms in (2.1). Different values of θ could be applied to different constituents of Q, giving explicit, semi-implicit or implicit forms.

Viscous terms are computed explicitly at time level n, the Coriolis force and the hydrostatic pressure are taken at time level $n + 1/2$, and surface elevation is taken at time level $n + 1$. The hydrostatic pressure is updated via (2.3) after tracer equations are solved, so is automatically half time step staggered (at $n + 1/2$) from the new velocity field. The second order Adams-Bashforth scheme is applied to the Coriolis force. Using implicit surface elevation together with implicit barotropic flow divergence (in equation (2.2)) helps to damp fast waves which are not resolved. With fully implicit surface elevation the temporal accuracy of the method is degraded to the first order. The second order accuracy can be easily recovered by using the Crank-Nickolson temporal form for the elevation and the divergence at no cost when it is required for some particular purposes.

Explicit Coriolis force and vertical viscosity can limit permissible time steps in some situations, so the method to employ (semi-) implicit Coriolis and vertical viscosity terms is also introduced in the current model. For an easy explanation we leave their implementation to be discussed in section 2.4.4.

Writing out all the terms in $Q^{n+\theta}$ one gets

$$\frac{\mathbf{u}^{n+1} - \mathbf{u}^n}{\Delta t} + g\nabla\eta^{n+1} =$$
$$-(\mathbf{v} \cdot \nabla_3 \mathbf{u})^n - f\mathbf{k} \times \mathbf{u}^{n+1/2} - \frac{1}{\rho_0}\nabla p^{n+1/2}$$
$$+\nabla \cdot A_h \nabla \mathbf{u}^n + \partial_z A_v \partial_z \mathbf{u}^n \qquad\qquad (2.35)$$
$$+\frac{\Delta t}{2}\mathbf{v}^n \cdot \nabla_3 \left[(\mathbf{v} \cdot \nabla_3 \mathbf{u})^n + f\mathbf{k} \times \mathbf{u}^{n+1/2} + \frac{1}{\rho_0}\nabla p^{n+1/2} + g\nabla\eta^n \right],$$

where terms containing third order derivatives are neglected as we are working with linear basis functions. The Coriolis force is computed with the approximation:

$$\mathbf{u}^{n+1/2} = (3/2 + \epsilon_{AB})\mathbf{u}^n - (1/2 + \epsilon_{AB})\mathbf{u}^{n-1}, \qquad (2.36)$$

where ϵ_{AB} is a small but finite value used to stabilize the second-order Adams-Bashforth method.

The next step is to employ the projection method. First, an auxiliary velocity $\mathbf{u}^*$ is introduced such that

$$\frac{\mathbf{u}^* - \mathbf{u}^n}{\Delta t} = -\gamma g \nabla \eta^n + \mathbf{R}, \qquad (2.37)$$

where $\mathbf{R}$ represents the rhs of (2.35), and γ is a tunable parameter with a range between (0, 1). A term with the contribution from surface elevation at time level n has been introduced to the rhs of (2.37), it does not exist in (2.35). This equation can be easily solved after applying Galerkin discretization, as the rhs is explicitly computed.

The correct velocity is determined using the equation

$$\frac{\mathbf{u}^{n+1} - \mathbf{u}^*}{\Delta t} = -g \nabla (\eta^{n+1} - \gamma \eta^n), \qquad (2.38)$$

which is derived by subtracting (2.37) from (2.35). Here η^{n+1} is the still unknown elevation at the new time step.

Before taking this correction step the surface elevation η^{n+1} should be determined. The temporal discretization of equation (2.2) is

$$\frac{\eta^{n+1} - \eta^n}{\Delta t} = -\nabla \cdot \int_{-H}^{0} \mathbf{u}^{n+1} \mathrm{d}z, \qquad (2.39)$$

where the divergence of the barotropic flow is treated implicitly. Substituting (2.38) into (2.39) one gets the equation for computing the surface elevation:

$$\frac{\eta^{n+1} - \eta^n}{\Delta t} - \Delta t g \nabla \cdot \int_{-H}^{0} \nabla (\eta^{n+1} - \gamma \eta^n) \mathrm{d}z = -\nabla \cdot \int_{-H}^{0} \mathbf{u}^* \mathrm{d}z. \qquad (2.40)$$

Note that the surface elevation is treated fully implicitly. The partial contribution from surface elevation at time level n in (2.37) is only introduced to decrease the temporal 'distance' between $\mathbf{u}^{n+1}$ and $\mathbf{u}^*$, thus controlling the strength of stabilization for the pressure mode. When γ is set to 1 the stabilization effects will be fully eliminated, and $\gamma = 0$ gives the strongest stabilization for a fixed time step. The next section will further explain the role of the parameter γ together with the justification of the stabilization mechanism of the splitting method. Here we only emphasize that taking the pressure splitting procedure before taking spatial discretization is essential for having stabilization effects (Zienkiewicz and Taylor, 2000).

The procedure to solve the dynamical governing equations can be summarized as: first, solve (2.37) to obtain the auxiliary velocity $\mathbf{u}^*$; then solve (2.40) to obtain η^{n+1}; the last step, solve (2.38) to obtain the correct velocity $\mathbf{u}^{n+1}$. In this respect, the procedure is very similar to FD models which use implicit free surface, for instance, MITgcm.

The auxiliary and full velocity share the same numerical approximation:

$$\mathbf{u}^* \simeq \sum_{j=1}^{N} (u_j^*, \ v_j^*) N_j$$

$$\bar{\mathbf{u}}^* = \left[u_1^*, \ \cdots, \ u_j^*, \ \cdots, \ u_N^*, \ v_1^*, \ \cdots, \ v_j^*, \ \cdots, \ v_N^* \right]^{\mathrm{T}},$$

(2.41)

where the length of the velocity vector $\bar{\mathbf{u}}^*$ is 2N. For compactness of notation all the nodal value vectors will be represented without overlines below, and this will not cause confusion, as it is clear that they are referred to vectors in fully discrete equations.

2.4.2 Matrix form of equations

To solve the semi-discrete equations (2.37), (2.40) and (2.38) the standard Galerkin FE procedure is used. Approximations (2.15), (2.16) and (2.41) are substituted into these equations. Equations (2.37) and (2.38) are weighted by test functions $\{N_i\}$ and integrated over the model domain Ω, and (2.40) is weighted by test functions $\{M_i\}$ and integrated over the surface Γ_1. The matrix form of the first step is

$$
\begin{aligned}
\mathbf{M}_u \Delta \mathbf{u}^* = \\
&- \Delta t \left(\mathbf{N}(\mathbf{v}^n) \mathbf{u}^n + \mathbf{L} \mathbf{u}^{n+1/2} + \mathbf{K} \mathbf{u}^n + \mathbf{C} p^{n+1/2} + \gamma g \mathbf{G} \eta^n \right) \\
&+ \Delta t \left(\mathbf{S} \boldsymbol{\tau}^{n+1} - \mathbf{B}(\mathbf{u}^n) \mathbf{u}^n \right) \\
&- \frac{\Delta t^2}{2} \left(\mathbf{N}_s(\mathbf{v}^n) \mathbf{u}^n + \mathbf{L}_s(\mathbf{v}^n) \mathbf{u}^{n+1/2} + \mathbf{C}_s(\mathbf{v}^n) p^{n+1/2} + g \mathbf{G}_s(\mathbf{u}^n) \eta^n \right),
\end{aligned}
$$

(2.42)

where $\Delta \mathbf{u}^* = \mathbf{u}^* - \mathbf{u}^n$, and the viscous and stabilization terms have been integrated by parts. The left-hand side (lhs) denotes the time derivative term. The first row on the rhs represents the advection, Coriolis force, viscous, hydrostatic pressure and surface pressure terms. The second row on the rhs gives the boundary integration arising from integrating by parts the viscous term. The last row is the stabilization contribution after integration by parts. The associated boundary contributions from stabilization terms are neglected, as the residual on the boundaries is negligible.

The mass matrix $\mathbf{M}_u$ is given by

$$\mathbf{M}_u \equiv \begin{pmatrix} M' & 0 \\ 0 & M' \end{pmatrix}, \text{ where } M'_{ij} = \int_\Omega N_i N_j \mathrm{d}\Omega, \text{ for } 1 \leq i,j \leq N. \quad (2.43)$$

The advection term results in matrix $\mathbf{N}$:

$$\mathbf{N}(\tilde{\mathbf{v}}) \equiv \begin{pmatrix} N'(\tilde{\mathbf{v}}) & 0 \\ 0 & N'(\tilde{\mathbf{v}}) \end{pmatrix}, \quad (2.44)$$

$$N'_{ij}(\tilde{\mathbf{v}}) = \int_\Omega N_i \tilde{\mathbf{v}} \cdot \nabla_3 N_j \mathrm{d}\Omega, \text{ for } 1 \leq i,j \leq N. \quad (2.45)$$

The matrix in the Coriolis term is given by

$$\mathbf{L} \equiv f \begin{pmatrix} 0 & -L' \\ L' & 0 \end{pmatrix}, \text{ where } L' = M'. \tag{2.46}$$

The matrix in the viscous term is

$$\mathbf{K} \equiv \begin{pmatrix} K' & 0 \\ 0 & K' \end{pmatrix}, \tag{2.47}$$

$$K'_{ij} = \int_\Omega (A_h \nabla N_i \cdot \nabla N_j + A_v \partial_z N_i \partial_z N_j) \mathrm{d}\Omega, \text{ for } 1 \leq i, j \leq \text{N}. \tag{2.48}$$

The boundary integral on rigid walls is zero, and on the surface and at the bottom it gives the terms with matrices $\mathbf{S}$ and $\mathbf{B}$ respectively:

$$\mathbf{S} \equiv \begin{pmatrix} S' & 0 \\ 0 & S' \end{pmatrix}, \mathbf{B}(\tilde{\mathbf{u}}) \equiv \begin{pmatrix} B'(\tilde{\mathbf{u}}) & 0 \\ 0 & B'(\tilde{\mathbf{u}}) \end{pmatrix}, \tag{2.49}$$

$$S'_{ij} = \int_{\Gamma_1} N_i M_j \mathrm{d}\Gamma_1, \ B'_{ij}(\tilde{\mathbf{u}}) = \int_{\Gamma_2} C_d |\tilde{\mathbf{u}}| N_i N_j \, \mathrm{d}\Gamma_2, \tag{2.50}$$

where the surface integration is taken on proper boundary surfaces, and only associated matrix entries are non-zero. Note that each component of the surface wind stress has been approximated in the same way as for the surface elevation (2.16), so totally $\boldsymbol{\tau}$ is of length 2M. The contribution from the surface elevation is $\gamma g \mathbf{G} \eta^n$, where

$$\mathbf{G} \equiv \begin{pmatrix} G^1 \\ G^2 \end{pmatrix}, \tag{2.51}$$

$$G^q_{ij} = \int_\Omega N_i \frac{\partial M_j}{\partial x_q} \mathrm{d}\Omega, \text{ for } 1 \leq i \leq \text{N}; \ 1 \leq j \leq \text{M}; \ q = 1, 2. \tag{2.52}$$

The matrices with subscript s in the last row of (2.42) correspond to terms for stabilizing advection. Their matrix structures are similar to their counterparts in the first row of the rhs, so only their matrix entries are shown here:

$$N'_{s,ij}(\tilde{\mathbf{v}}) = \int_\Omega \tilde{\mathbf{v}} \cdot \nabla_3 N_i \, \tilde{\mathbf{v}} \cdot \nabla_3 N_j \mathrm{d}\Omega, \text{ for } 1 \leq i, j \leq \text{N}, \tag{2.53}$$

$$L'_{s,ij}(\tilde{\mathbf{v}}) = \int_\Omega \tilde{\mathbf{v}} \cdot \nabla_3 N_i \, N_j \mathrm{d}\Omega, \text{ for } 1 \leq i, j \leq \text{N}, \tag{2.54}$$

$$G^q_{s,ij}(\tilde{\mathbf{u}}) = \int_\Omega \tilde{\mathbf{u}} \cdot \nabla N_i \, \frac{\partial M_j}{\partial x_q} \mathrm{d}\Omega, \text{ for } 1 \leq i \leq \text{N}; \ 1 \leq j \leq \text{M}; \ q = 1, 2. \tag{2.55}$$

The discretization form for the hydrostatic pressure will be discussed separately in section 2.10.

The discrete form of the second step (2.40) is

$$(\mathbf{M}_\eta + \Delta t^2 \mathbf{H})\Delta\eta = \Delta t \left(\mathbf{G}^\mathrm{T}\mathbf{u}^* - \Delta t(1-\gamma)\mathbf{H}\eta^n - \mathbf{O}_\eta \mathbf{U}_{OB}^\perp \right), \qquad (2.56)$$

where $\Delta\eta = \eta^{n+1} - \eta^n$. The last term on the rhs of (2.56) contains the open boundary contribution, which appears after taking integration by parts the divergence terms in (2.40). $\mathbf{U}_{OB}^\perp$ is a vector of length M, with entries on open boundaries filled with specified vertically integrated normal velocity (positive is out of the domain) and zero elsewhere. The matrix for the time stepping term is

$$\mathbf{M}_\eta \equiv \left(M'_\eta\right), \ M'_{\eta,ij} = \int_{\Gamma_1} M_i M_j \, \mathrm{d}\Gamma_1, \ \text{for } 1 \le i, j \le \mathrm{M}. \qquad (2.57)$$

The matrix $\mathbf{H}$ is

$$\mathbf{H} \equiv (H'), \ H'_{ij} = g \int_\Omega \nabla M_i \cdot \nabla M_j \, \mathrm{d}\Omega, \ \text{for } 1 \le i, j \le \mathrm{M}. \qquad (2.58)$$

The matrix of the open boundary term contains the line integral:

$$\mathbf{O}_\eta \equiv \left(O'_\eta\right), \ O'_{\eta,ij} = \int_{S_o} M_i M_j \, \mathrm{d}S_o, \ \text{for } i, j \text{ on } S_o, \qquad (2.59)$$

where matrix entries that are not on open boundaries are filled with zero.

The final matrix form of the correction step (2.38) is

$$\mathbf{M}_u \Delta\mathbf{u} = \mathbf{M}_u \Delta\mathbf{u}^* - \Delta t g \mathbf{G}(\eta^{n+1} - \gamma\eta^n), \qquad (2.60)$$

where $\Delta\mathbf{u} = \mathbf{u}^{n+1} - \mathbf{u}^n$. To summarize, the procedure of solution for the horizontal velocity and elevation consists of three steps. One begins with the prediction step to solve for $\mathbf{u}^*$, then finds elevation η^{n+1}, and finally corrects the velocity field $\mathbf{u}^{n+1}$ so that it satisfies the vertically integrated continuity equation at the end of each time step.

2.4.3 Circumventing the LBB restrictions

To see how the restrictions on the choice of the basis function pairs for velocity and pressure is lifted by the split method, we can simply examine the equation (2.42), (2.56), and (2.60) in steady-state conditions. For simplicity we only keep the viscosity term and surface elevation term in the momentum equation, then the three steps of the splitting method are:

$$\Delta\mathbf{u}^* = -\Delta t \mathbf{M}_u^{-1}[\mathbf{K}\mathbf{u}^n + \gamma g \mathbf{G}\eta^n - \mathbf{f_1}], \qquad (2.61)$$

$$\Delta\eta = (\mathbf{M}_\eta + \Delta t^2 \mathbf{H})^{-1} \Delta t[\mathbf{G}^\mathrm{T}\mathbf{u}^n + \mathbf{G}^\mathrm{T}\Delta\mathbf{u}^* - \Delta t(1-\gamma)\mathbf{H}\eta^n - \mathbf{f_2}], \quad (2.62)$$

$$\Delta\mathbf{u} = \Delta\mathbf{u}^* - \Delta t g \mathbf{M}_u^{-1}\mathbf{G}(\Delta\eta + (1-\gamma)\eta^n), \qquad (2.63)$$

where $\mathbf{f_1}$ and $\mathbf{f_2}$ are used to represent the boundary forcing in the momentum equation and surface elevation equation, respectively. In steady state $\Delta\eta =$

0, and $\Delta \mathbf{u} = 0$. Substituting (2.61) into (2.63) and dropping the superscript n one gets

$$\mathbf{Ku} + g\mathbf{G}\eta = \mathbf{f_1}, \tag{2.64}$$

and combining (2.62) and (2.63) one gets

$$\mathbf{G}^{\mathrm{T}}\mathbf{u} + \Delta t(1 - \gamma)[g\mathbf{G}^{\mathrm{T}}\mathbf{M}_u^{-1}\mathbf{G} - \mathbf{H}]\eta = \mathbf{f_2}. \tag{2.65}$$

Finally, we get a system for $\mathbf{u}$ and η which can be written in the form

$$\begin{pmatrix} \mathbf{K} & g\mathbf{G} \\ \mathbf{G}^{\mathrm{T}} & \Delta t(1 - \gamma)[\mathbf{G}^{\mathrm{T}}\mathbf{M}^{-1}\mathbf{G} - \mathbf{H}] \end{pmatrix} \left\{ \begin{matrix} \mathbf{u} \\ \eta \end{matrix} \right\} = \left\{ \begin{matrix} \mathbf{f_1} \\ \mathbf{f_2} \end{matrix} \right\}. \tag{2.66}$$

This system is always positive definite for $\gamma \in [0, 1)$ and leads to a non-singular solution for any combination of basis functions $\{N_j\}$ and $\{M_j\}$. The reason for which the LBB condition is circumvented is that the non-zero lower-right block matrix entry in (2.66) is introduced by the splitting procedure. This matrix block is equivalent to the difference between the so-called fourth-order and second-order approximations of the Laplacian operators. A FD analog in one dimension is the difference between five point and three point Laplacian operators which is equivalent to biharmonic friction.

The procedure to justify the stabilization mechanism employed here is essentially that of Codina et al. (1998) but modified to the hydrostatic case. Another viewpoint (Rannacher, 1992) was taken by Codina and Zienkiewicz (2002) and Codina et al. (2006) who identified the similarity between stabilization mechanisms from the CBS method and different SGS methods. The difference between the two viewpoints is that the approach adopted here is to analyze the problem for the end-of-step velocity, while Rannacher (1992) explains the stabilization in terms of the intermediate velocity. For details about how to employ the second viewpoint one can refer to Codina et al. (2006).

The γ factor in (2.66) can be regarded as a coefficient to combine the two splitting methods described in Zienkiewicz and Taylor (2000). When $\gamma = 0$ the 'split A' is recovered which provides the largest stabilization to the pressure modes for a fixed temporal/spatial discretization, and $\gamma = 1$ recovers 'split B' which has no stabilization effects on pressure modes. Introducing the γ parameter gives freedom in adjusting the stabilization strength in practice. The value of γ should be adjusted so that the spurious pressure modes can be filtered out but the numerical diffusion is as small as possible. A value very close to unity is found sufficient to stabilize pressure in many applications.

We are working with the fully implicit scheme for the surface elevation and divergence of the vertically integrated flow in most applications, so the situation for the semi-implicit form is not discussed above. But following the procedure presented above it can also be shown that only the temporal form of the divergence of the vertically integrated velocity in the vertically integrated continuity equation influences stabilization.

2.4.4 Implicit temporal form

One wants to use large time steps when the model resolution is coarse. Explicit treatment of the Coriolis force can be a limiting factor in this case, especially in polar regions where the Coriolis parameter is large. In many oceanographic applications the explicit form of vertical viscosity can be the limiting factor for time step through the criteria $A_v \Delta t / \Delta z^2 \leq 2$, especially in surface and bottom boundary layers where fine vertical resolution is often used. In this section modifications to the solution procedure described above will be introduced, which permit implicit or semi-implicit treatment to the Coriolis force and vertical viscosity.

We employ the general θ method on the Coriolis force (implying that it is estimated as a weighted sum over steps $n + 1$ and n) and the implicit form on the viscosity term, so that the semi-discrete momentum equation (2.35) becomes

$$\frac{\mathbf{u}^{n+1} - \mathbf{u}^n}{\Delta t} + f\theta \mathbf{k} \times (\mathbf{u}^{n+1} - \mathbf{u}^n) + g\nabla\eta^{n+1} - \partial_z A_v \partial_z \mathbf{u}^{n+1} =$$

$$-(\mathbf{v} \cdot \nabla_3 \mathbf{u})^n - f\mathbf{k} \times \mathbf{u}^n - \frac{1}{\rho_0}\nabla p^{n+1/2} + \nabla \cdot A_h \nabla \mathbf{u}^n \qquad (2.67)$$

$$+\frac{\Delta t}{2}\mathbf{v}^n \cdot \nabla_3 \left[(\mathbf{v} \cdot \nabla_3 \mathbf{u})^n + f\mathbf{k} \times \mathbf{u}^n + \frac{1}{\rho_0}\nabla p^{n+1/2} + g\nabla\eta^n\right],$$

where $\theta = 1$ or 0.5 gives a fully implicit or semi-implicit schemes for the Coriolis force, respectively. Both of them, and the vertical viscosity as well, are unconditionally stable.

The first step of the CBS procedure given by (2.37) in this case is

$$\frac{\mathbf{u}^* - \mathbf{u}^n}{\Delta t} + f\theta \mathbf{k} \times (\mathbf{u}^* - \mathbf{u}^n) - \partial_z A_v \partial_z \mathbf{u}^* = -\gamma g\nabla\eta^n + \mathbf{R}, \qquad (2.68)$$

where $\mathbf{R}$ represents the rhs of (2.67).

The correction step similar to (2.38) is

$$\frac{\mathbf{u}^{n+1} - \mathbf{u}^*}{\Delta t} + f\theta \mathbf{k} \times (\mathbf{u}^{n+1} - \mathbf{u}^*) = -g\nabla(\eta^{n+1} - \gamma\eta^n), \qquad (2.69)$$

which now contains the Coriolis term on the lhs. In the above expression, the vertical viscosity contribution has been neglected, which is a necessary approximation for proceeding the split method. If the implicit vertical viscosity contribution were maintained in (2.69), we would not be able to obtain the algebraic expression of $\mathbf{u}^{n+1}$ in terms of η^{n+1}, which is required to get the equation for surface elevation. This approximation, also used in MITgcm, corresponds to the requirement that the implicit vertical viscosity should not alter the barotropic flow, that is, it can only redistribute momentum in the vertical. This requirement is enforced in the strong statement.

Then $\mathbf{u}^{n+1} \equiv (u^{n+1}, v^{n+1})$ can be expressed analytically from (2.69). Substituting it into (2.39) one gets the equation for η^{n+1}:

$$\frac{\eta^{n+1} - \eta^n}{\Delta t} - g\nabla \cdot \int_{-H}^{0} (\alpha\nabla + \beta\nabla_s)(\eta^{n+1} - \gamma\eta^n)\mathrm{d}z = -\nabla \cdot \int_{-H}^{0} \mathbf{u}^*\mathrm{d}z, \quad (2.70)$$

where $\nabla_s = (\partial_y, -\partial_x)$ is the skewed gradient operator, $\alpha = 1/(d\Delta t)$ and $\beta = f\theta/d$ with $d = f^2\theta^2 + 1/\Delta t^2$.

Solving (2.68) and (2.69) with iterative solvers could be difficult if $\theta f \Delta t$ exceeds one because the Coriolis term corresponds to the antisymmetric part of the operator. For this reason we invert the operator $(1/\Delta t + f\theta\mathbf{k}\times)$ analytically before taking spatial FE discretization. It does not involve any approximations and results in

$$\Delta\mathbf{u}^* = \alpha \begin{pmatrix} V_x + R_x \\ V_y + R_y \end{pmatrix} + \beta \begin{pmatrix} V_y + R_y \\ -V_x - R_x \end{pmatrix} - \gamma g \left(\alpha\nabla + \beta\nabla_s\right)\eta^n, \qquad (2.71)$$

$$\Delta\mathbf{u} = \Delta\mathbf{u}^* - g\left(\alpha\nabla + \beta\nabla_s\right)\left(\eta^{n+1} - \gamma\eta^n\right), \qquad (2.72)$$

where $V_x \equiv \partial_z A_v \partial_z u^*$, $V_y \equiv \partial_z A_v \partial_z v^*$.

With this manipulation, the final matrix of the operator on the lhs (called stiffness matrix) from discretizing (2.72) is simply the mass matrix, while viscous terms will make the stiffness matrix from discretizing (2.71) nonsymmetric. The contribution from the viscous terms is small in most places (with the exception in the mixed layer), so the final matrix problem is better suited to iterative solvers than taking the original form.

The final Galerkin formulation of (2.71) is given by

$$\begin{aligned} (\mathbf{M}_u + \mathbf{K}_V^{\mathrm{i}})\Delta\mathbf{u}^* = \\ - \left(\mathbf{N}^{\mathrm{i}}(\mathbf{v}^n) + \mathbf{L}^{\mathrm{i}} + \mathbf{K}_V^{\mathrm{i}} + \mathbf{K}_H^{\mathrm{i}}\right)\mathbf{u}^n \\ - \left(\mathbf{C}^{\mathrm{i}}p^{n+1/2} + \gamma g\mathbf{G}^{\mathrm{i}}\eta^n\right) + \mathbf{S}^{\mathrm{i}}\tau^{n+1} - \mathbf{B}^{\mathrm{i}}(\mathbf{u}^n)\mathbf{u}^n \\ - \frac{\Delta t}{2}\left(\mathbf{N}_s^{\mathrm{i}}(\mathbf{v}^n)\mathbf{u}^n + \mathbf{L}_s^{\mathrm{i}}(\mathbf{v}^n)\mathbf{u}^n + \mathbf{C}_s^{\mathrm{i}}(\mathbf{v}^n)p^{n+1/2} + g\mathbf{G}_s^{\mathrm{i}}(\mathbf{u}^n)\eta^n\right), \end{aligned} \qquad (2.73)$$

where superscript i is used for matrices that are different from those in (2.42) due to implicit time stepping. The difference comes from the β terms in (2.71). For example, different to (2.44), the matrix of the advection term is

$$\mathbf{N}^{\mathrm{i}}(\tilde{\mathbf{v}}) \equiv \begin{pmatrix} \alpha N'(\tilde{\mathbf{v}}) & \beta N'(\tilde{\mathbf{v}}) \\ -\beta N'(\tilde{\mathbf{v}}) & \alpha N'(\tilde{\mathbf{v}}) \end{pmatrix}. \qquad (2.74)$$

Matrices $\mathbf{L}^{\mathrm{i}}$, $\mathbf{S}^{\mathrm{i}}$, $\mathbf{B}^{\mathrm{i}}$, $\mathbf{N}_s^{\mathrm{i}}$, $\mathbf{L}_s^{\mathrm{i}}$ have similar changes to their matrix structures, and for simplicity are not presented here. The matrix for the surface elevation term is

$$\mathbf{G}^{\mathrm{i}} \equiv \begin{pmatrix} \alpha G^1 + \beta G^2 \\ \alpha G^2 - \beta G^1 \end{pmatrix}, \qquad (2.75)$$

and the two matrices for viscosity are

$$\mathbf{K}_V^i \equiv \begin{pmatrix} \alpha K_V' & \beta K_V' \\ -\beta K_V' & \alpha K_V' \end{pmatrix}, \quad \mathbf{K}_H^i \equiv \begin{pmatrix} \alpha K_H' & \beta K_H' \\ -\beta K_H' & \alpha K_H' \end{pmatrix}, \tag{2.76}$$

where

$$K_{V,ij}' = \int_\Omega A_v \partial_z N_i \partial_z N_j \, d\Omega, \quad \text{for } 1 \le i,j \le N, \tag{2.77}$$

$$K_{H,ij}' = \int_\Omega A_h \nabla N_i \cdot \nabla N_j \, d\Omega, \quad \text{for } 1 \le i,j \le N. \tag{2.78}$$

The weak statement for the surface elevation equation (2.70) is

$$\frac{1}{\Delta t} \int_{\Gamma_1} M_i \left(\eta^{n+1} - \eta^n \right) \, d\Gamma_1 =$$
$$+ \int_\Omega \nabla M_i \cdot \left(\mathbf{u}^* - g \left(\alpha \nabla + \beta \nabla_s \right) \left(\eta^{n+1} - \gamma \eta^n \right) \right) \, d\Omega$$
$$- \int_{S_o} M_i \mathbf{U}_{OB}^\perp \, dS_o. \tag{2.79}$$

Its matrix form can be written as

$$(\mathbf{M}_\eta + \Delta t \mathbf{H}^i) \Delta \eta = \Delta t \left(\mathbf{G}^\mathrm{T} \mathbf{u}^* - (1-\gamma) \mathbf{H}^i \eta^n - \mathbf{O}_\eta \mathbf{U}_{OB}^\perp \right), \tag{2.80}$$

where matrix $\mathbf{H}^i \equiv ((H^i)')$, to which the matrix entry is

$$(H^i)_{ij}' = g \int_\Omega (\alpha \nabla M_i \cdot \nabla M_j + \beta \nabla M_i \cdot \nabla_s M_j) \, d\Omega,$$
$$\text{for } 1 \le i,j \le M. \tag{2.81}$$

The matrix form of the last correction step (2.72) is

$$\mathbf{M}_u \Delta \mathbf{u} = \mathbf{M}_u \Delta \mathbf{u}^* - g \mathbf{G}^i (\eta^{n+1} - \gamma \eta^n). \tag{2.82}$$

The procedure of solution remains the same as in the case of the explicit temporal form, namely one first solves for $\mathbf{u}^*$, then for elevation η^{n+1}, and finally does the correction step to recover velocity field $\mathbf{u}^{n+1}$ to satisfy the vertically integrated continuity equation.

2.4.5   Boundary conditions on rigid walls

When no-slip boundary conditions are employed, the two components of the horizontal velocity on rigid walls can simply be set to zero and no extra efforts are required. But when free-slip boundary conditions are used, only the velocity component normal to the boundaries should be set to zero. Therefore, applying free-slip boundary conditions requires to transform the x and y (zonal

and meridional) momentum equations to the tangential and normal (with respect to the boundaries) momentum equations when rigid wall boundaries are not aligned with the coordinate system.

Let $\mathbf{Mu} = \mathbf{R}$ be the discrete momentum equation to be solved. To transform this equation to the tangential and normal equation on rigid walls, we simply pre-multiply the mass matrix and the rhs vector with a rotation matrix R and then post-multiply the mass matrix by its transpose R^{T}:

$$\left(R\mathbf{M}R^{\mathrm{T}}\right)\mathbf{u}^{rot} = R\mathbf{R}, \tag{2.83}$$

where $\mathbf{u}^{rot} \equiv (\mathbf{u}_t, \mathbf{u}_n)^{\mathrm{T}}$ coincide with the tangential and normal directions, R has a size of $2\mathrm{N} \times 2\mathrm{N}$. After taking this transformation, the no-normal-flow boundary condition can be easily applied. Once $\mathbf{u}^{rot}$ is solved, it can be converted to velocity along x and y directions for each boundary node i by

$$\begin{pmatrix} u_x^i \\ u_y^i \end{pmatrix} = \begin{pmatrix} -n_y^i & n_x^i \\ n_x^i & n_y^i \end{pmatrix} \begin{pmatrix} u_t^i \\ u_n^i \end{pmatrix}, \tag{2.84}$$

where $\mathbf{n}^i \equiv (n_x^i, n_y^i)$ is the outward pointing unit normal vector at node i. The 2×2 orthogonal nodal rotation matrix for node i enters the whole rotation matrix R and R^{T} in the following way:

$$R_{ii} = -n_y^i, \ R_{i,i+\mathrm{N}} = n_x^i, \ R_{i+\mathrm{N},i} = n_x^i, \ R_{i+\mathrm{N},i+\mathrm{N}} = n_y^i. \tag{2.85}$$

Except for rows associated with boundary nodes, there is only a unity on the diagonal of matrix R.

The mass consistent normal vector (Engelman et al., 1982) can be calculated by

$$\mathbf{n}^i = \frac{1}{n^i} \int_{\Gamma_1} \nabla M_i \mathrm{d}\Gamma_1, \ \text{where} \ n^i = \left| \int_{\Gamma_1} \nabla M_i \mathrm{d}\Gamma_1 \right|. \tag{2.86}$$

The integration is simply necessary on the surface mesh because only *vertical* closed boundaries are treated as rigid walls.

2.5   Updating vertical velocity

After the horizontal velocity and surface elevation are solved at every time step, the vertical velocity w can be diagnosed via (2.7). The solution of vertical velocity is realized by introducing a new variable, as described in Danilov et al. (2004). The original problem involves first order derivatives, which leads to difficulties when using iterative solvers. To facilitate using them, a potential Φ is introduced:

$$\partial_z\partial_z\Phi = -\nabla \cdot \mathbf{u}^{n+1}, \ \text{where} \ \partial_z\Phi = w. \tag{2.87}$$

Now the problem with Φ as the variable is the second order one (with two boundary conditions (2.8) and (2.9)), and its discrete equation involves a symmetric matrix which is much better suited to iterative solvers. In the following

discussion we only consider the situation when the implicit form (section 2.4.4) is used to solve for the horizontal velocity and surface elevation. The result can easily be extended to the explicit case.

Since the two boundary conditions are both of the von Neumann type the solvability conditions should be satisfied by the rhs of the discrete continuity equation. To satisfy the solvability, two conditions should be met: first, the vertically integrated continuity equation (elevation equation) and the continuity equation should be projected on consistent sets of test functions, that is, they should satisfy relation (2.18); second, the velocity expression (2.72) should be substituted into (2.87) before applying Galerkin discretization to it. These points will be clarified later in this section.

Substituting (2.72) into (2.87) leads to

$$\partial_z\partial_z\Phi = -\nabla\cdot\mathbf{u}^* + g\nabla\cdot(\alpha\nabla + \beta\nabla_s)\left(\eta^{n+1} - \gamma\eta^n\right). \qquad (2.88)$$

The potential Φ is approximated as

$$\Phi \simeq \sum_{j=1}^{N}\Phi_j N_j$$
$$\bar{\Phi} = [\Phi_1, \cdots, \Phi_j, \cdots, \Phi_N]^{\mathrm{T}}. \qquad (2.89)$$

With the convention used before, the vector $\bar{\Phi}$ will be represented without the overline later for brevity.

Weighting (2.88) by $\{N_j\}$ and integrating it by parts over the domain one gets

$$\int_\Omega \partial_z N_i \partial_z \Phi^{n+1}\,\mathrm{d}\Omega = -\int_\Omega \nabla N_i \cdot \left(\mathbf{u}^* - g\left(\alpha\nabla + \beta\nabla_s\right)\left(\eta^{n+1} - \gamma\eta^n\right)\right)\,\mathrm{d}\Omega$$
$$+ \frac{1}{\Delta t}\int_{\Gamma_1} N_i(\eta^{n+1} - \eta^n)\,\mathrm{d}\Gamma_1 + \int_{\Gamma_4} N_i\mathbf{u}_{OB}^\perp\,\mathrm{d}\Gamma_4, \qquad (2.90)$$

where the boundary conditions (2.8) and (2.9) have been enforced. The open boundary velocity $\mathbf{u}_{OB}^\perp$ is simply taken as velocity at open boundary nodes. It satisfies the same transport conditions as those imposed when solving for elevation. Substituting (2.89) into (2.90) leads to the matrix form:

$$\mathbf{M}_\Phi\Phi^{n+1} = -\mathbf{D}_\Phi\mathbf{u}^* + \mathbf{E}_\Phi(\eta^{n+1} - \gamma\eta^n) + \mathbf{S}_\Phi(\eta^{n+1} - \eta^n) + \mathbf{O}_\Phi\mathbf{u}_{OB}^\perp, \qquad (2.91)$$

where

$$\mathbf{M}_\Phi \equiv (M'_\Phi), \qquad M'_{\Phi,ij} = \int_\Omega \partial_z N_i \partial_z N_j \, \mathrm{d}\Omega, \text{ for } 1 \le i, j \le \mathrm{N}, \qquad (2.92)$$

$$\mathbf{D}_\Phi \equiv \left(D^1_\Phi \ D^2_\Phi\right), \qquad D^q_{\Phi,ij} = \int_\Omega \frac{\partial N_i}{\partial x_q} N_j \, \mathrm{d}\Omega, \text{ for } i \le i, j \le \mathrm{N}; \ \mathrm{q=1,2}, \quad (2.93)$$

$$\mathbf{E}_\Phi \equiv (E'_\Phi), \qquad E'_{\Phi,ij} = \int_\Omega g \nabla N_i \cdot (\alpha \nabla + \beta \nabla_s) M_j \, \mathrm{d}\Omega, \qquad (2.94)$$
$$\text{for } 1 \le i \le \mathrm{N}, 1 \le j \le \mathrm{M},$$

$$\mathbf{S}_\Phi \equiv (S'_\Phi), \qquad S'_{\Phi,ij} = \frac{1}{\Delta t} \int_{\Gamma_1} N_i M_j \, \mathrm{d}\Gamma_1, \text{ for } i, j \text{ on } \Gamma_1, \qquad (2.95)$$

$$\mathbf{O}_\Phi \equiv (O'_\Phi), \qquad O'_{\Phi,ij} = \int_{\Gamma_4} N_i N_j \, \mathrm{d}\Gamma_4, \text{ for } i, j \text{ on } \Gamma_4. \qquad (2.96)$$

The solvability condition for (2.91) requires that the sums of its right-hand side over nodes aligned vertically be zero. If the solution for η^{n+1} were exact, this requirement would hold automatically. Indeed, by summing up the equations in (2.90) that are associated with 3D nodes under a 2D node I, and applying the relation (2.18), one gets

$$0 = - \int_\Omega \nabla M_I \cdot \left(\mathbf{u}^* - g\left(\alpha \nabla + \beta \nabla_s\right)\left(\eta^{n+1} - \gamma \eta^n\right)\right) \, \mathrm{d}\Omega$$
$$+ \frac{1}{\Delta t} \int_{\Gamma_1} M_I(\eta^{n+1} - \eta^n) \, \mathrm{d}\Gamma_1 + \int_{\Gamma_4} M_I \mathbf{u}^\perp_{OB} \, \mathrm{d}\Gamma_4, \qquad (2.97)$$

which means that the solvability requirement is satisfied. As a result of consistent discretization, equation (2.97) exactly recovers the discretized elevation equation (2.79) because $\int_{\Gamma_4} M_I \mathbf{u}^\perp_{OB} \mathrm{d}\Gamma_4 = \int_{S_o} M_I \mathbf{U}^\perp_{OB} \mathrm{d}S_o$ is also enforced.

Now it is also clear why (2.88) instead of (2.87) should be used to determine the vertical velocity: using (2.87) will not lead to consistent discrete formulation for the continuity equation and the elevation equation.

Small errors can be present up to solver precision, so before solving (2.91) its rhs is still summed over vertically aligned nodes and the residual is removed.

2.6   Solving tracer equations

2.6.1   Numerical advection schemes

Characteristic Galerkin scheme

The tracer evolution equation (2.10) can be solved with the CG method. The semi-discrete equation is

$$\frac{C^{n+1} - C^n}{\Delta t} = -(\mathbf{v} \cdot \nabla_3 C)^n + \nabla \cdot K_h \nabla C^n + \partial_z K_v \partial_z C^n$$
$$+ \frac{\Delta t}{2} \mathbf{v}^n \cdot \nabla_3 (\mathbf{v} \cdot \nabla_3 C)^n, \qquad (2.98)$$

which is an explicit scheme. Using the approximation (2.15) the matrix form of (2.98) is given by

$$\mathbf{M}'\Delta C = -\Delta t(\mathbf{N}'C^n + \mathbf{K}'C^n) - \frac{\Delta t^2}{2}\mathbf{N}'_s C^n + \Delta t\mathbf{S}'q, \qquad (2.99)$$

where q is the flux of tracer C on the surface (2.12) when the von Neumann boundary condition is employed. It is linked to the heat flux for the temperature equation and the freshwater flux for the salinity equation. The flux is approximated here as $\sum q_j M_j$. Note that the flux q_j usually consists of two contributions, one due to climatological fluxes and the other due to restoring of surface temperature and salinity to climatological values. The entries to the matrices in (2.99) are the same as defined before for the momentum equation, except that the viscosity should be replaced with diffusivity in the diffusion term.

Flux-corrected transport scheme

In many cases it is desirable that the advection scheme preserves monotonicity to eliminate over- and undershoots. The FCT scheme based on explicit time stepping can produce promising results with respect to both stabilization effects and computation efficiency (for a review on the history and development of FCT schemes see Kuzmin et al., 2005). A variation to FCT, the pointwise-corrected transport (PCT) scheme (Kuzmin, 2000) has been adopted by Kliem (2004) into QUODDY (Lynch et al., 1996) and appears to be very useful. Although PCT is less expensive than FCT, it does not prevent the formation of local extremes entirely (Kliem, 2004). The classical FCT scheme following Löhner et al. (1987) is adopted in the current model, since it works well for transient problems and provides a compromise between the CPU cost and quality (Kuzmin, personal communication). It should be noted that the spectrum of advection schemes possible with the FE method is very limited compared to the FD method, there is a variety of schemes that can be conveniently used in FD ocean models.

A brief summary for the implementation of the FCT scheme in the current model is given below. The procedure can be formulated as a sequence of the following operations:

1. Solve (2.99), which in this case is called a high-order scheme.

2. Perform mass matrix lumping (replace it with a diagonal matrix whose entries are row sums of the original matrix) on the left-hand side and add a discrete diffusion operator to the rhs of the high-order scheme to transform it into a low-order non-oscillatory scheme. Solve the modified equations to get the low-order solution.

3. Compute the antidiffusive flux contributed from each element to its nodes.

4. Limit the antidiffusive flux to guarantee local extremum diminishing. A limiting factor for each element is calculated at this stage.

5. Update the solution by adding limited antidiffusive fluxes to the low-order solution.

The FCT procedure starts from solving the CG formulation (2.99). For simplicity we rewrite it in a compact form as

$$\mathbf{M}\Delta C = \mathbf{R}, \tag{2.100}$$

where $\mathbf{M}$ denotes the mass matrix and $\mathbf{R}$ the sum of the rhs of (2.99).

In the first step (2.100) is solved to get the high-order solution:

$$\mathbf{M}_C \Delta C^H = \mathbf{R}, \tag{2.101}$$

where $\mathbf{M}_C$ is used to emphasize that the consistent mass matrix is used, and ΔC^H represents the increment of tracer solved by inverting the consistent mass matrix.

To obtain a low-order method, one lumps the mass matrix and adds a mass diffusion term into (2.100):

$$\mathbf{M}_L \Delta C^L = \mathbf{R} + \varepsilon(\mathbf{M}_C - \mathbf{M}_L)C^n, \tag{2.102}$$

where $\mathbf{M}_L$ is the lumped mass matrix, ε is an experimentally chosen parameter, which controls the amount of added diffusion. The excess in diffusion will be removed where possible, when antidiffusive fluxes are added back.

Rewriting the high-order equation (2.101) as

$$\mathbf{M}_L \Delta C^H = \mathbf{R} + (\mathbf{M}_L - \mathbf{M}_C)\Delta C^H, \tag{2.103}$$

and subtracting (2.102) from it we get the difference between the high-order and low-order solutions:

$$\Delta C^H - \Delta C^L = \mathbf{M}_L^{-1}(\mathbf{M}_L - \mathbf{M}_C)(\Delta C^H + \varepsilon C^n). \tag{2.104}$$

It is the antidiffusive flux that makes the high-order solution different from the low-order one. The antidiffusive flux contributed from the individual element e to its node i can be denoted as

$$F_{e,i} = (\mathbf{M}_L^{-1})_i \sum_j \left[(\mathbf{M}_L - \mathbf{M}_C)_{e,ij} \left(\Delta C^H + \varepsilon C^n \right)_j \right], \tag{2.105}$$

where i and j are local indices of nodes of element e. Note that the matrix entries are only the components from the considered element.

The next step is to limit the antidiffusive fluxes in each element. This involves the following steps:

(a) Find for every node i the admissible solution range by taking the maximum and minimum over all neighbor nodes of node i

$$C_i^+ = \max\{C_k^L\}, \ C_i^- = \min\{C_k^L\}, \ k \in N_{n,i}, \qquad (2.106)$$

where $N_{n,i}$ is the set of neighbor nodes of node i, and for simplicity maximum and minimum are denoted with '+' and '-', respectively. Löhner et al. (1987) take the admissible range from two fields, both the new low-order solution C^L and the solution from the last time step C^n. But Kuzmin and Turek (2002) pointed out that this could produce numerical ripples if advection is due to variable velocity field, so only the new low-order solution is used here to get the maximum and minimum values.

(b) Compute the admissible increment for node i

$$Q_i^\pm = C_i^\pm - C_i^L. \qquad (2.107)$$

(c) Compute the sum of all positive/negative antidiffusive element contributions to node i

$$P_i^\pm = \sum_e \ {}^{\max}_{\min}\{0, F_{e,i}\}, \qquad (2.108)$$

where the sum is over all elements that contribute to node i.

(d) Compute the nodal bounds for limiting factors:

$$R_i^\pm = \begin{cases} \min\{1, Q_i^\pm/P_i^\pm\} & \text{if } P_i^\pm \neq 0 \\ 0 & \text{if } P_i^\pm = 0 \end{cases} \qquad (2.109)$$

(e) Compute the limiting factors by

$$\alpha_e = \min_i \{R_i^+ (\text{ if } F_{e,i} \geq 0), \ R_i^- (\text{ if } F_{e,i} < 0)\}, \qquad (2.110)$$

where the minimum is sought for over nodes of element e.

After the limiting factors are calculated, the final solution for time level $n+1$ can be updated for each node i as

$$C_i^{n+1} = C_i^L + \sum_e \alpha_e F_{e,i}, \qquad (2.111)$$

where the sum is over all elements that contribute to node i. Note that the FCT method in the FE implementation is more expensive compared to the FD implementation because of increased number of neighboring elements.
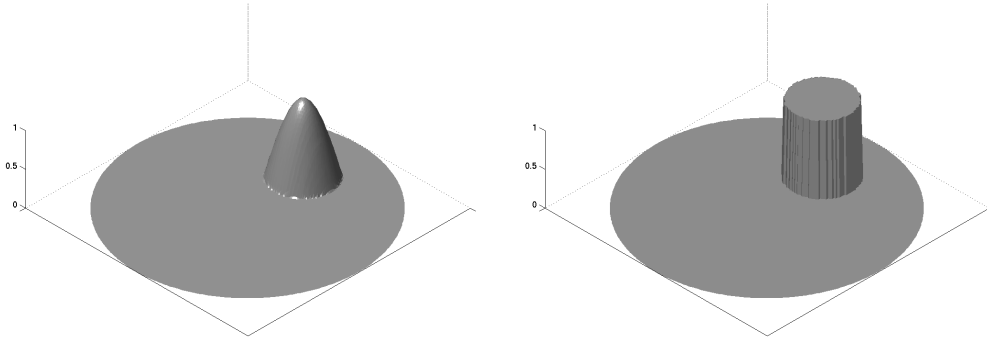
Figure 2.4: Initial fields of the cosine cone (left) and cylindrical (right) distribution used in the advection scheme tests.

Galerkin least-square method

Besides the CG method and FCT method, the GLS method employed in Danilov et al. (2004) is also implemented in the current model. It is semi-implicit and second-order in time. The details of its implementation will not be repeated here. Testing the performance of different schemes is to be described in the next subsection.

2.6.2   Testing advection schemes

The advection schemes are tested in a 2D domain. The pure advection equation is solved, that is, there is no explicit diffusion applied in these tests. The model domain is circular with a radius of 10 km, and the coordinate origin is at the circle center. The velocity field is specified to make one rotation in 24 h:

$$\mathbf{u}(x,y) = \frac{2\pi}{86400 \text{ sec}} \, \mathbf{k} \times (x,y)^{\mathrm{T}}. \qquad (2.112)$$

Two different initial fields are used (Fig. 2.4). The first is a cosine cone distribution with the maximum concentration of unity at the center, and the second a cylindrical distribution with the concentration of unity. The radius of both the cone and the cylinder is 2.5 km and their center is located at (5 km, 0 km). Initial concentration outside of the cone and cylinder is zero. Such standard configurations are often used to test advection schemes (e.g., Kliem, 2004).

Two different resolutions are used in the simulations. The coarse resolution is 250 m with 4834 nodes and 9439 elements, and the fine resolution is 125 m with 19343 nodes and 38242 elements. The mesh elements are of high quality (quite close to equilateral triangles). The resolution used in the current work is defined as the height of the triangle. The time step is 150 s for the coarse resolution case, and 60 s for the fine resolution case.

All the simulations are performed for 24 h (one rotation), so the analytical solution is identical to the initial fields. The results are summarized in Table 2.1, in which C_{max} and C_{min} are the maximum and minimum concentration after the simulations, and RMS is the root mean square of the difference between the simulated concentration and the analytical solution. The concentration fields are shown in Figs. 2.5 and 2.6. In the FCT scheme, the ε parameter in (2.102) is set to 0.5, which is found sufficient to give smooth low-order solution and to fully eliminate overshoots and undershoots. The stabilization coefficient for the GLS method is chosen following the analysis in the appendix of Danilov et al. (2004).

For each scheme the RMS errors decrease with an increase in resolution. Both the CG and GLS schemes produce overshoots and/or undershoots. The CG scheme gives the largest range of tracer concentration associated with largest overshoots and undershoots, while the GLS scheme has slightly larger RMS errors. A wake can be observed in the CG solutions when resolution is coarse or the gradient of fields is sharp, yet it is not clearly observed in the GLS solutions. The FCT solutions are free of small-scale noise and under-/overshoots.

The CG scheme works well in the case of rotating cones (Fig. 2.5a,b), producing a maximum concentration very close to the analytical solution. Some noise upstream of the cone exists because this scheme's leading error (second-order) is in form of dispersion. But explicit dissipation used in practical applications can suppress it, as it is weak in such situations. So the CG scheme can be used when the field is relatively smooth.

Dispersion errors are not clearly observed both up- and downstream the cone in the GLS runs (Fig. 2.5c,d). Using smaller stabilization coefficient in the GLS scheme can reduce the implicit diffusion effects, but noise as observed in the CG solutions will appear (not shown). The GLS method allows larger time steps than the other two schemes, as it is semi-implicit.

Noise is fully eliminated in the FCT scheme simulations (Fig. 2.5e,f), but the cone maximum is slightly reduced, especially at the coarse resolution. Although the FCT scheme is more diffusive at coarse resolution, its advantage of being monotonic is beneficial when limiting overshoots and undershoots is crucial. One more advantage is that it can work stably even without any explicit diffusion. Its permissible largest time step is found to be about 50% more than that of the CG scheme.

The case of rotating cylinder serves to compare the performance of different advection schemes when the tracer field is not smooth. It is clearly observed that the FCT scheme gives much better results than others. Not only are the extrema limited, but also the cylindrical shape is well represented in the FCT simulations. The CG solution clearly has both overshoots above the cylinder and a wake. Adding extra diffusion does not help to improve the solution in this case, because it will diffuse the solution field too much to give a cone-shaped distribution. The GLS scheme also produces large overshoots around

Table 2.1: Summary of the advection test cases.

	$\Delta x(m)$	$\Delta t(s)$	Scheme	C_{max}	C_{min}	RMS
cone	250	150	CG	0.996	-0.027	0.006
			FCT	0.928	0.000	0.006
			GLS	0.996	-0.026	0.007
	125	60	CG	0.999	-0.015	0.002
			FCT	0.973	0.000	0.002
			GLS	1.000	-0.014	0.003
cylinder	250	150	CG	1.125	-0.166	0.060
			FCT	0.999	0.000	0.059
			GLS	1.116	-0.073	0.064
	125	60	CG	1.146	-0.157	0.045
			FCT	1.000	0.000	0.044
			GLS	1.096	-0.073	0.050

CG, characteristic Galerkin method; FCT, flux-corrected transport scheme; GLS, Galerkin least-square method.

the edge of the cylinder, but dispersive noise up- and downstream the cylinder is eliminated. It can be concluded that only the FCT scheme can accurately represent fields with sharp gradients. By comparison with the results shown in figure 5 of Kliem (2004), the FCT scheme has less implicit diffusion than the PCT scheme.

The FCT and GLS schemes require similar CPU time, about 3 times that required by the CG scheme (comparison based on one-processor runs). But the GLS scheme is semi-implicit and allows to use larger time steps. Implicit FCT scheme is not implemented in the current model, and studies on it are left for future work. A scheme which can be recommended for any situation does not exist, since one has to consider both accuracy and efficiency. Which scheme to choose depends on applications and research interest.

2.6.3   Tracer conservation

The property of global tracer conservation can be seen by integrating the tracer equation (2.10) over volume:

$$\int_\Omega \partial_t C\, d\Omega = -\int_{\partial\Omega} (\mathbf{v}C)\cdot \mathbf{n}_3\, d\Gamma + \int_\Omega C\nabla_3\cdot \mathbf{v}\, d\Omega - \int_{\Gamma_1} q\, d\Gamma, \qquad (2.113)$$

where integration by parts and the divergence theorem have been applied to the advection term, thus leading to the first two integrals on the rhs. The divergence theorem and the boundary conditions for tracers (2.12) and (2.13)
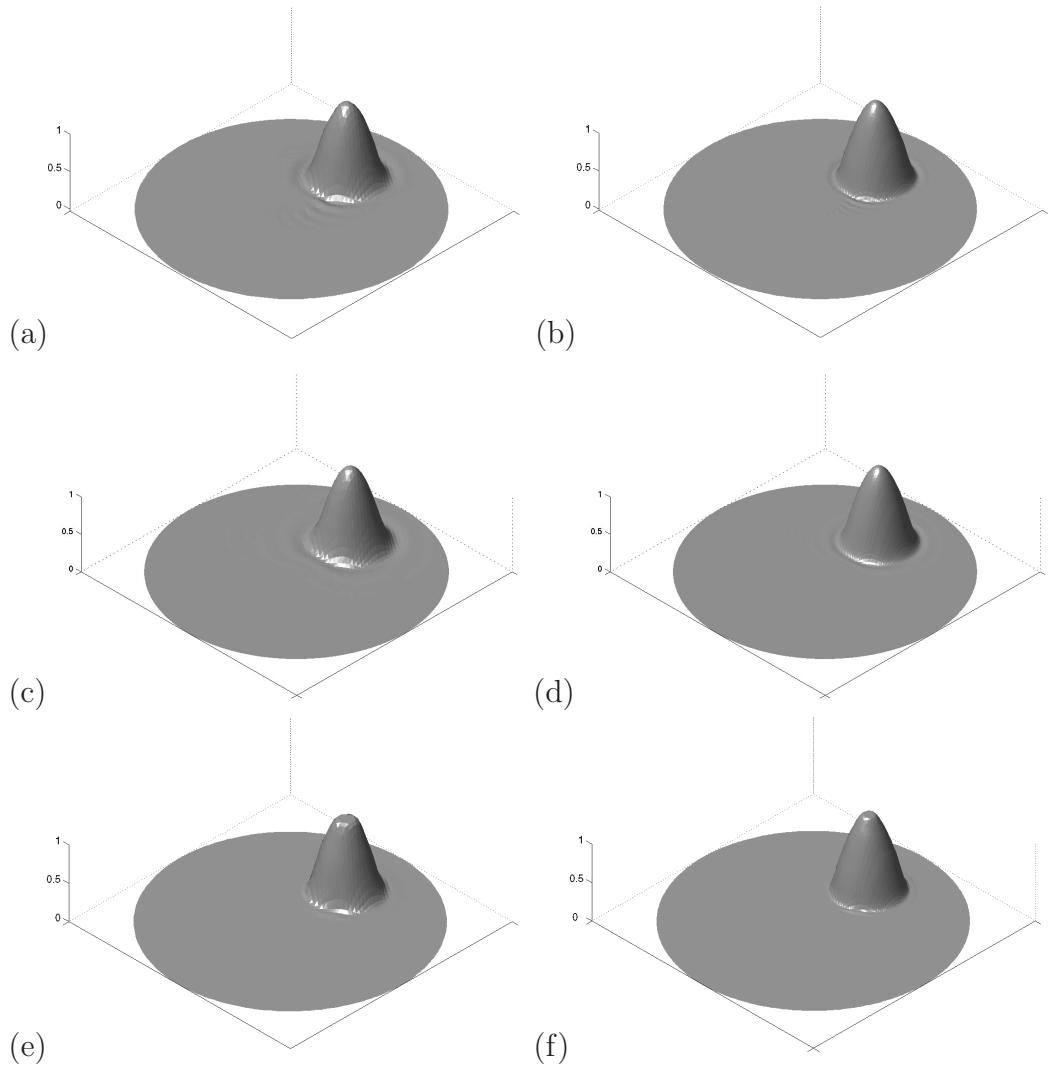
tp

Figure 2.5: Tracer concentration after one rotation in case of cosine cone distribution for (a)(b) CG, (c)(d) GLS, (e)(f) FCT schemes. The left show the results at 250 m resolution, and the right at 125 m resolution. All these schemes represent smooth tracer fields well. Weak dispersion errors can be observed in the CG solutions. The FCT scheme has slightly larger implicit diffusion, especially at coarse resolution.

have been applied to the diffusion term, thus leading to the last integral. Enforcing the boundary conditions (2.6), (2.8) and (2.9) and introducing the continuity equation (2.7) to the above expression one gets

$$\int_{\Omega} \partial_t C \, \mathrm{d}\Omega = - \int_{\Gamma_1} C \partial_t \eta \, \mathrm{d}\Gamma - \int_{\Gamma_1} q \, \mathrm{d}\Gamma, \qquad (2.114)$$

tp
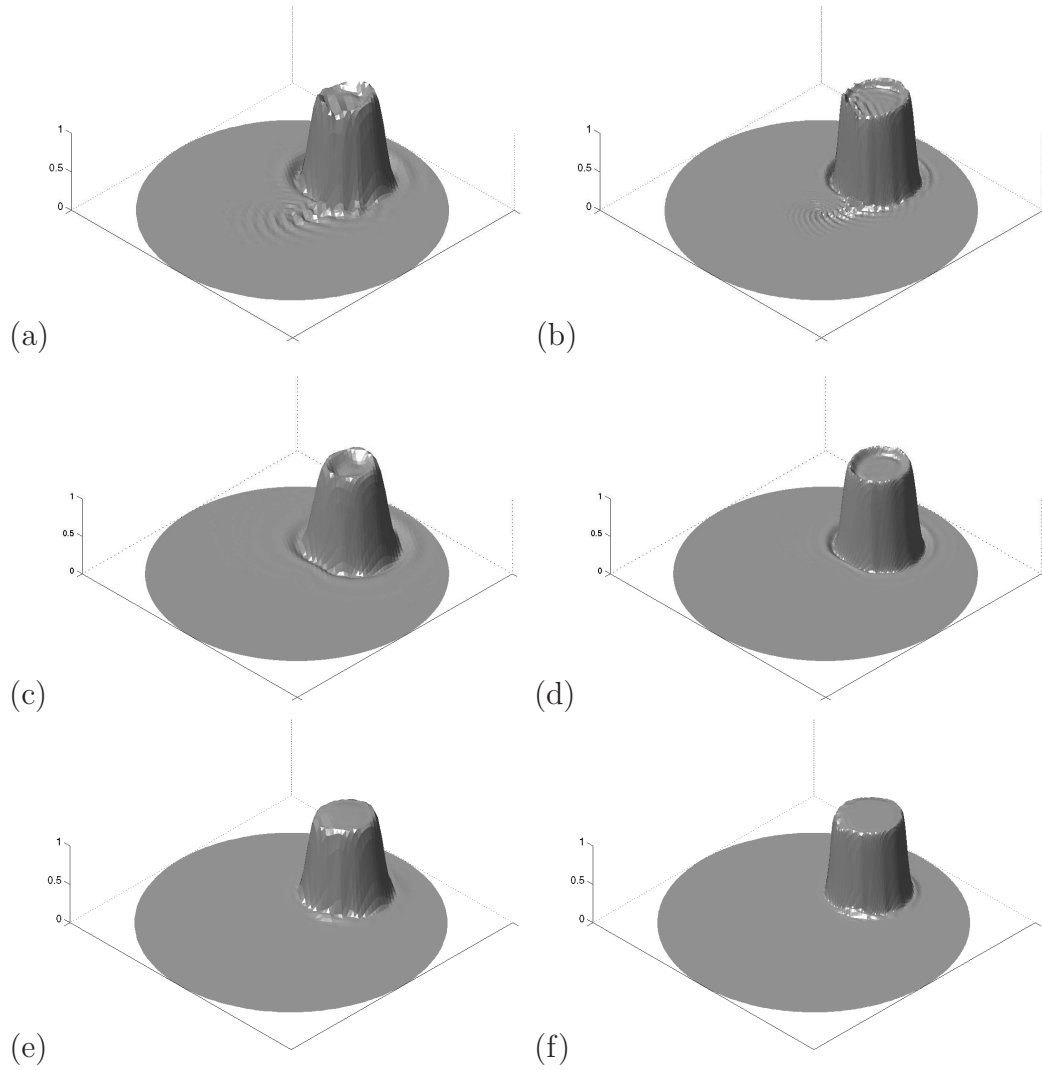
Figure 2.6: Same as in Fig. 2.5 but for cases of cylinder distribution. Both the CG and GLS solutions are featured with large overshoots around the edge of the cylinder, but the CG solutions also show clear dispersion errors. The FCT scheme is suitable for simulating tracer fields with sharp gradients.

provided that there is no open boundary. The Reynolds transport theorem leads the first integral in the above expression to

$$\int_\Omega \partial_t C \, \mathrm{d}\Omega = \frac{\mathrm{d}}{\mathrm{d}t} \int_\Omega C \, \mathrm{d}\Omega - \int_{\Gamma_1} C \partial_t \eta \, \mathrm{d}\Gamma, \qquad (2.115)$$

where the boundary condition $w = \partial_t \eta$ is used. Then one can rewrite (2.114) as

$$\frac{\mathrm{d}}{\mathrm{d}t} \int_\Omega C \,\mathrm{d}\Omega = -\int_{\Gamma_1} q \,\mathrm{d}\Gamma. \qquad (2.116)$$

So tracers are conserved provided that no tracer flux is supplied.

It is important to ensure that the discrete tracer equation (2.99) maintains the property of global tracer conservation, especially when simulations are to run over climatic timescales. Setting the test function $N_i = 1$ in (2.99) one obtains

$$\int_\Omega \Delta C \,\mathrm{d}\Omega = -\Delta t \int_\Omega (\mathbf{u} \cdot \nabla + w\partial_z)C \,\mathrm{d}\Omega, \qquad (2.117)$$

where the diffusion and stabilization terms vanish because they contain derivatives of N_i. The global tracer conservation can be guaranteed if the rhs integral in (2.117) vanishes. This is ensured by a consistent discretization for tracer and continuity equations.

Consistent discretization means: first, the test functions used in (2.90) and the basis functions interpolating C in (2.117) are the same ($\{N_i\}$); second, the velocities used to advect tracers in (2.117) are represented in the same way as they appear in the continuity equation (2.90). Under such conditions, combining (2.90) and (2.117) leads the rhs of (2.117) to be the surface integral of wC plus the integral of the tracer flux through the open boundary. This is the conservation law for a linear free surface model. The remaining advective tracer flux through the ocean surface is the consequence of considering the surface at $z = 0$ as the upper boundary. It disappears when the rigid lid approximation is used, or if the change in the volume of the upper layer is taken into account (nonlinear free surface).

As shown above, the stabilization terms in the tracer equation do not affect the global tracer conservation property. It is the same when the GLS stabilization method is used (Danilov et al., 2004) because the stabilization term contains spatial derivatives of test functions. The FCT method does not violate the tracer conservation either (Kuzmin et al., 2005).

Remark

To avoid using virtual salinity flux, moving the surface boundary to follow the elevation η instead of fixing it to $z = 0$ is one useful strategy. The arbitrary Lagrangian Eulerian (ALE) formulation can be used to realize moving model boundaries (see e.g., Farhat et al., 2001; Formaggia and Nobile, 2004; Nithiarasu, 2005; Badia and Codina, 2006, also see White et al., 2007 for an example of its application in ocean modelling). But the ALE formulation involves re-computing Jacobians at every time step and requires more CPU time when mesh geometry is updated.

2.7   Full time-stepping algorithm

The full time-stepping algorithm is shown in Fig. 2.7. The dynamics and thermodynamics are staggered in time with a half time step. First, density and hydrostatic pressure gradients are diagnosed from potential temperature and salinity at time level n. Then, the dynamic variables u, v, and η are stepped forward from time level $n - 1/2$ to time level $n + 1/2$ using the pressure projection (split) method. The vertical velocity is diagnosed from the horizontal velocity. The last step is updating tracer fields from time level n to time level $n + 1$ using the velocity field at time level $n + 1/2$. This algorithm allows internal gravity waves to leapfrog in time, thus giving more stability. If surface forcing is applied, forcing data are read before each iteration step.
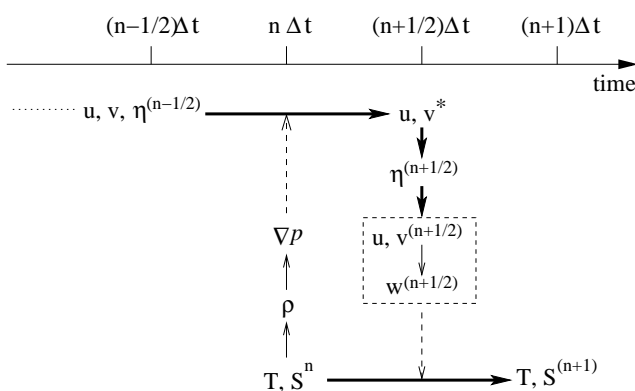
Figure 2.7: Schematic explanation of the overall time-stepping algorithm. The prognostic processes are indicated with thick solid arrow-lines, and the diagnostic processes are indicated with thin solid arrow-lines. The dash arrow-lines present the connection between the dynamical and thermodynamical parts, which are staggered in time.

2.8   Solution of linear equation systems

The stiffness matrix in the momentum equations (2.42), (2.60) and tracer equation (2.99) in the case of explicit temporal forms reduces to only the mass matrix. It can efficiently be inverted with an iterative procedure using the lumped matrix as a pre-conditioner. Taking the tracer equation (2.100) as an example, the solution can be approximated as $\mathbf{M}_L^{-1}\mathbf{R}$ in the first step. Then the iterative procedure can be started by substituting it to the rhs of (2.103). This solution process has been widely used (e.g., Löhner et al., 1987) because it converges very rapidly. The iteration number can be determined by checking the error norms, and a few iterations are usually sufficient.

When (semi-) implicit Coriolis and vertical viscous terms are employed, the

final stiffness matrix after diagonalization in equation (2.73) contains contribution from the vertical viscosity. Since the asymmetric component is usually small in most regions of the ocean, this matrix problem is well suited to iterative solvers.

To solve the surface elevation equation (2.56) the standard iterative solver is used (Frickenhaus et al., 2005). This equation can be efficiently solved because its stiffness matrix is symmetric and has only a dimension of surface node number M.

2.9 Isoneutral diffusion and GM skew flux

As mentioned in the introduction, neutral physics is not naturally represented in z coordinate models. So explicit treatment of neutral physics is required in FEOM. This section is devoted to the implementation of the isoneutral diffusion and GM skew flux.

Redi (1982) applied a straightforward rotation to the diffusion tensor to allow z-level models to use physically realistic isoneutral diffusive fluxes. The diffusion tensor based on the small slope approximation was given by Gent and McWilliams (1990). Gent and McWilliams (1990) and Gent et al. (1995) suggested a closure to represent the adiabatic stirring effects from ocean mesoscale eddies. The stirring, which acts to reduce the isoneutral slopes and available potential energy, can be parameterized by a divergence-free advective flux (Gent et al., 1995), or by a skew flux (Griffies, 1998). The Redi diffusive flux and GM skew flux contribute to the symmetric and antisymmetric components of the SGS tracer transport operator, respectively. Some practical issues associated with the implementation of the Redi/GM closures based on applications in MOM are discussed by Griffies et al. (1998) and Griffies (1998).

2.9.1 Isoneutral diffusion

Fluid particles moving along neutral directions do not experience buoyancy forces. Therefore, neutral directions are preferred and mesoscale eddies tend to mix tracers along them. Analysis (e.g., Ledwell et al., 1993; Kunze and Sanford, 1996) indicates that on large scales the dianeutral to neutral mixing can be at the level of 10^{-8} in the interior of the ocean. This anisotropy can be represented by ϵ, the ratio of the dianeutral to neutral diffusivities

$$\epsilon = K_D/K_I \approx 10^{-8}, \qquad (2.118)$$

where K_D and K_I are the dianeutral and isoneutral diffusivities, respectively.

We rewrite the tracer equation (2.10) as

$$\partial_t C + \mathbf{v} \cdot \nabla_3 C + \nabla \cdot \mathbf{F} = 0, \qquad (2.119)$$

where the SGS Redi diffusive flux $\mathbf{F}$ is given by

$$\mathbf{F} = -\mathbf{K}_{Redi}\nabla_3 C. \tag{2.120}$$

The Redi diffusion tensor (Redi, 1982) is given by

$$\mathbf{K}_{Redi} = \frac{K_I}{1 + S^2}\begin{pmatrix} 1 + S_y^2 + \epsilon S_x^2 & (\epsilon - 1)S_x S_y & (1 - \epsilon)S_x \\ (\epsilon - 1)S_x S_y & 1 + S_x^2 + \epsilon S_y^2 & (1 - \epsilon)S_y \\ (1 - \epsilon)S_x & (1 - \epsilon)S_y & \epsilon + S^2 \end{pmatrix}, \tag{2.121}$$

where S_x and S_y are the x and y components of $\mathbf{S}$, respectively, and $S^2 = S_x^2 + S_y^2$.

The neutral slope is defined as

$$\begin{aligned} \mathbf{S} &\equiv \nabla_\rho z \\ &= -\left(\frac{\nabla\rho}{\rho_{,z}}\right) \\ &= -\left(\frac{-\alpha'\nabla T + \beta'\nabla S}{-\alpha'T_{,z} + \beta'S_{,z}}\right), \end{aligned} \tag{2.122}$$

where ∇_ρ represents the lateral gradient taken along the neutral direction, and α' and β' are thermal expansion and saline contraction coefficients. The nodal values of α' and β' can be calculated at each time level following the method given by McDougall (1987). The isoneutral slopes $\mathbf{S}$ are then calculated on elements.

In the bulk of the ocean the neutral slopes $|\mathbf{S}|$ usually are less than $1/100$, thus a small slope assumption to the diffusion tensor (2.121) is usually adopted. Under the small slope assumption, $|S| << 1$, the following approximation for (2.121) is valid (Gent and McWilliams, 1990):

$$\mathbf{K}_{Redi} = K_I\begin{pmatrix} 1 & 0 & S_x \\ 0 & 1 & S_y \\ S_x & S_y & \epsilon + S^2 \end{pmatrix}. \tag{2.123}$$

The horizontal and vertical components of the mixing flux under the small slope approximation are then given by

$$\begin{aligned} \mathbf{F}^{(h)} &= -K_I\nabla_\rho C, & (2.124) \\ F^{(z)} &= -K_I\mathbf{S}\cdot\nabla_\rho C - K_D C_{,z}, & (2.125) \end{aligned}$$

where

$$\nabla_\rho = \nabla + \mathbf{S}\partial_z \tag{2.126}$$

2.9.2 GM scheme

The GM scheme parameterizes the advective flux due to bolus velocity, $\mathbf{v}^*$, in addition to the model's resolved scale velocity. The advective bolus flux suggested by Gent and McWilliams (1990) and Gent et al. (1995) is in the form of $\mathbf{v}^*C$, where

$$\mathbf{v}^* = -\partial_z(\kappa\mathbf{S}) + \hat{\mathbf{z}}\nabla\cdot(\kappa\mathbf{S}), \tag{2.127}$$

which is non-divergent. Here κ stands for the skew diffusivity. Deriving the bolus flux is based on an assumption: the mesoscale eddies, which modify isopycnals so as to locally provide adiabatic sink of available potential energy, also act on all tracers in the same fashion.

Discretization of bolus velocities involves derivatives of κ and $\mathbf{S}$, which can potentially lead to discretization errors. Griffies (1998) suggested a skew flux form by separating the bolus flux as follows

$$
\begin{aligned}
\mathbf{v}^*C &= \begin{pmatrix} -\partial_z(\kappa S_x)C \\ -\partial_z(\kappa S_y)C \\ (\partial_x(\kappa S_x) + \partial_y(\kappa S_y))C \end{pmatrix} \\[2mm]
&= \begin{pmatrix} -\partial_z(\kappa S_x C) \\ -\partial_z(\kappa S_y C) \\ \partial_x(\kappa S_x C) + \partial_y(\kappa S_y C) \end{pmatrix} + \begin{pmatrix} \kappa S_x C_{,z} \\ \kappa S_y C_{,z} \\ -\kappa S_x C_{,x} - \kappa S_y C_{,y} \end{pmatrix}
\end{aligned}
\tag{2.128}
$$

The first term is divergence-free and has no effect on the tracer field. So it is only necessary to keep the second term, leading to the skew flux:

$$
\begin{aligned}
\mathbf{F}_{skew} &= \kappa\left(\mathbf{S}C_{,z} - \hat{\mathbf{z}}\mathbf{S}\cdot\nabla C\right) \\
&= -\mathbf{K}_{GM}\nabla_3 C,
\end{aligned}
\tag{2.129}
$$

where

$$\mathbf{K}_{GM} = \kappa\begin{pmatrix} 0 & 0 & -S_x \\ 0 & 0 & -S_y \\ S_x & S_y & 0 \end{pmatrix} \tag{2.130}$$

The combination of GM skew flux (2.129) and diffusive mixing (2.124), (2.125) leads to the full SGS flux:

$$\mathbf{F} = -\begin{pmatrix} K_I & 0 & (K_I-\kappa)S_x \\ 0 & K_I & (K_I-\kappa)S_y \\ (K_I+\kappa)S_x & (K_I+\kappa)S_y & K_D + K_I S^2 \end{pmatrix}\begin{pmatrix} C_{,x} \\ C_{,y} \\ C_{,z} \end{pmatrix}, \tag{2.131}$$

which gives the following flux components

$$
\begin{aligned}
\mathbf{F}^{(h)} &= -K_I\nabla C - (K_I-\kappa)\mathbf{S}C_{,z} \tag{2.132} \\
F^{(z)} &= -(K_D + K_I S^2)C_{,z} - (K_I+\kappa)\mathbf{S}\cdot\nabla C. \tag{2.133}
\end{aligned}
$$

Note that the diffusion part remains exactly symmetric while the GM part is exactly antisymmetric. In the case when $K_I = \kappa$, the tensor entries (1,3) and (2,3) of the tensor in (2.131) are simply zero. As a key practical result of Griffies (1998), applying skew flux scheme does not introduce extra cost to the existing Redi scheme, while the advective flux form (2.127) does.

2.9.3   Tapering

The small slope approximation to isoneutral slope is typically used in z model simulations. The tensor in (2.131), however, is not bounded as the neutral slopes increase. Hence, numerical instability will be incurred when the slopes are very steep. Such a situation typically occurs in the mixed layer, where isopycnals are nearly vertical. The possibility of infinite slopes makes even an implicit scheme numerically sensitive. In addition to numerical reasons for tapering neutral physics schemes, there are also kinematic reason for applying tapering near boundaries, as discussed in details by Griffies (2004). The study by Gnanadesikan et al. (2007) suggests that not only the diffusivity associated with the neutral physics closure, but also the details of tapering schemes can influence simulation results in a climate model.

The slope clipping scheme of Cox (1987) has shown to be inappropriate because of substantial spurious diffusion. The quadratic tapering scheme proposed by Gerdes et al. (1991) is the first method aiming to preserve the neutral orientation of the flux regardless of the slopes. More details of the work discussed here are studied by Griffies (2004). The following schemes have been implemented in FEOM.

Scheme I: *DM95*

The tapering scheme used by Danabasoglu and McWilliams (1995) is similar to that of Gerdes et al. (1991) but uses a hyperbolic tangent tapering function

$$f_1(S) = 1 + \tanh(\frac{S_{max} - |S|}{S_d}),\qquad(2.134)$$

where $S_d = 0.001$ is the scale of the width of the transition region, and $S_{max} = 0.01$ is the cut-off slope. This tapering function f_1 is inserted in front of the whole GM/Redi tensor in (2.131) with only the K_D term unaffected. So the diagonal neutral part in tensor element (3,3) can also be exponentially tapered to zero.

Scheme II: *Large97*

Based on the DM95 tapering scheme, Large et al. (1997) suggested to use a function of depth d additional to f_1:

$$f_2(S) = \left(1 + \sin \pi(\frac{\mathrm{d}}{\lambda_1 |\mathbf{S}|} - 1/2)\right)/2\qquad(2.135)$$

where the first baroclinic Rossby radius is given by $\lambda_1 = c_1/f$, with f the Coriolis parameter and $c_1 = 2$ m/s an approximate first baroclinic gravity wave speed. To handle the singularity at the equator, Large et al. (1997) restrict λ_1 to the range 15 km $\leq \lambda_1 \leq$ 100 km. This tapering was originally introduced

to fix some spurious interaction with the mixed-layer KPP parameterization. Based on discussions by Treguier et al. (1997); Held and Schneider (1999); Mc-Dougall and McIntosh (2001), Griffies (2004) addressed the kinematic reason for adopting this tapering function: undulating density surfaces can outcrop or incrop, at which point their effects on transport are truncated.

Scheme III: *Griffies' proposals*

Motivated by the studies of Treguier et al. (1997); Held and Schneider (1999); Send and Marshall (1995); Visbeck et al. (1996); Haine and Marshall (1998), Griffies (2004) proposed that it is appropriate to maintain a nontrivial parameterized horizontal advective and diffusive transport near boundaries and/or in steep neutral slope regions. For the diffusive flux, no taper is applied to the diagonal diffusive terms, the tensor elements (1,1) and (2,2) in (2.131), thus maintaining a nontrivial downgradient horizontal component to the flux. In regions where isoneutral slopes are steep, the resulting tracer diffusion is oriented in a horizontal-vertical manner. For the GM flux, a nontrivial GM flux in steep neutral slope regions is maintained through a linear tapering scheme (Treguier et al., 1997; Greatbatch and Li, 2000). That is, if a grid point is within the surface boundary layer, defined as the near surface region where isoneutral slopes are steeper than S_{max}, let $\kappa\mathbf{S}$ linearly move from its saturated value $(\kappa\mathbf{S})_{max}$ at the base of the boundary layer, to zero at the top of the surface grid cell. More practical tests are required for this tapering scheme.

2.9.4   Numerical implementation

Substituting (2.132) and (2.133) into (2.119) and taking the CG method lead to the matrix equation as given by (2.99), with the matrix $\mathbf{K}'$ now defined as

$$
\begin{aligned}
K'_{ij} \;=\; & \int_{\Omega} (\; K_I \nabla N_i \cdot \nabla N_j + (K_I - \kappa)\partial_z N_i \mathbf{S} \cdot \nabla N_j \qquad\qquad (2.136)\\
& + (K_D + K_I S^2)\partial_z N_i \partial_z N_j + (K_I + \kappa)\mathbf{S} \cdot \nabla N_i \partial_z N_j \;)\, \mathrm{d}\Omega,
\end{aligned}
$$

where one of the tapering schemes listed above should be applied at the appropriate place. Because of the intrinsic property of the FE method (variational formulation), the implementation of isoneutral diffusion in a FE model does not require extra efforts to ensure down-gradient diffusive fluxes as required in a FD model (for example, the functional formalism discussed by Griffies et al., 1998). But using the last expression in (2.122) to compute the neutral slope in order to ensure the balance of the active tracer isoneutral diffusive fluxes is generally required (Griffies et al., 1998).

Remark

It is worth mentioning that along-σ diffusivity/viscosity is similarly realized using the rotation tensor (2.121) with the isoneutral slope replaced by the slope

of σ grids. In reality the slope of σ grids can be large, therefore the small-slope approximation should not be applied in this case.

2.10   Calculating pressure gradient forces

2.10.1   An interpolation method

As mentioned previously, the problem of pressure gradient errors is common in FE models employing meshes that deviate from z-levels. One approach to reduce the pressure gradient errors in FE models is to use basis functions with which the hydrostatic relation (2.3) can be exactly approximated. This approach means that the order of basis functions for pressure and velocity should be higher than that used by us, which can lead to a more complicated and less efficient model scheme. Therefore, the method discussed here is based on linear basis functions used in our model.

The equations for $\partial p / \partial x$ and $\partial p / \partial y$ can be obtained by differencing (2.3):

$$\frac{\partial}{\partial z}\left(\frac{\partial p}{\partial x}\right) = -g\frac{\partial \rho}{\partial x}, \quad \frac{\partial}{\partial z}\left(\frac{\partial p}{\partial y}\right) = -g\frac{\partial \rho}{\partial y}. \tag{2.137}$$

The required baroclinic pressure force in the momentum equation is calculated by integrating (2.137) down from $z = 0$:

$$\frac{1}{\rho_0}\frac{\partial p}{\partial x} = \frac{g}{\rho_0}\int_z^0 \frac{\partial \rho}{\partial x}\,\mathrm{d}z', \quad \frac{1}{\rho_0}\frac{\partial p}{\partial y} = \frac{g}{\rho_0}\int_z^0 \frac{\partial \rho}{\partial y}\,\mathrm{d}z', \tag{2.138}$$

where the boundary conditions $\partial p / \partial x = 0$ and $\partial p / \partial y = 0$ at $z = 0$ are employed. Here the sequence of integration and differentiation is exchanged. This method, often referred as density Jacobian, results in more accurate schemes than first solving p and then taking horizontal derivatives (Song, 1998; Song and Wright, 1998), and is now widely used in σ coordinate ocean models. It is easy to see its advantage: the error of pressure gradient vanishes if density ρ is a linear function of z and the first order polynomial is used as the basis function for density. When the density is not the linear function of z, which is usually the case in realistic oceanographic applications, using first order basis function will still cause pressure gradient errors. To overcome this problem, we will use a pressure gradient force scheme based on nonlocal cubic spline interpolation and the FD method.

Although in the horizontal direction there are no definite aligning directions of grid nodes due to unstructured surface meshes, the grid nodes are aligned vertically in our model. Therefore, the one dimensional high order interpolation can easily be taken in the vertical direction, whereas a much more complicated scheme would be required for a fully unstructured grid. Note that interpolation methods can be more flexibly applied in FD models which use structured surface grids. An example is the method proposed by Shchepetkin
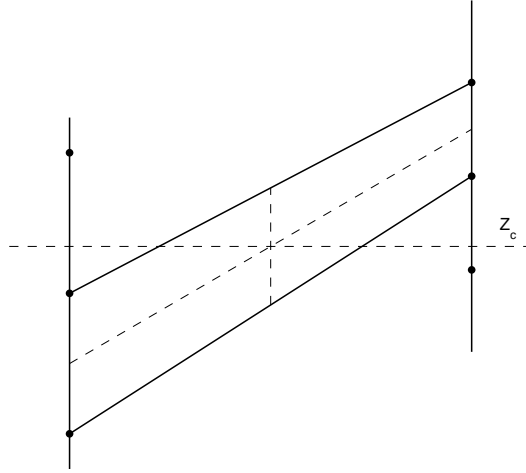
Figure 2.8: Explanation of calculating pressure gradient forces. Only one vertical face of a prism element is shown, indicated with solid lines.

and McWilliams (2003), which employs the cubic spline interpolation method under the framework of the *pseudo flux* form of the density Jacobian.

The nonlocal interpolation method is explained in Fig. 2.8. Along each vertical edge of the prism, the density is interpolated (cubic spline interpolation) to the common level z_c, which is chosen to be at the midlevel of the prism. When the applied horizontal resolution is not very fine and the bottom slope is very steep, one may need to extrapolate the density for the bottom elements, linear extrapolation is used in such cases. Then the three interpolated density values on the three vertical edges of a prism are differenced horizontally. This density gradient is considered as an elementwise constant value. Finally, the pressure gradient forces can be calculated with (2.138) using the FD method.

For each grid node the pressure gradient force is calculated separately in all prisms sharing it as a vertex. Therefore, a set of discontinuous piecewise-linear basis functions $\{Q_k\}$ is required to project the pressure gradient forces. Within elements these functions take the same spatial form as the continuous functions $\{N_i\}$. However, whereas functions $\{N_i\}$ are continuous and non-zero in all prisms that have node i as one of their vertices, the discontinuous basis functions $\{Q_k\}$ are defined such that they are non-zero inside only one prism. For each continuous basis function N_i, the number of associated discontinuous functions is the number of prisms that have node i as one of their vertices. The total number of discontinuous functions is denoted by Q.

Using $\{Q_k\}$, the hydrostatic pressure gradient forces can be approximated as

$$\left(\frac{1}{\rho_0}\frac{\partial p}{\partial x}, \ \frac{1}{\rho_0}\frac{\partial p}{\partial y}\right)^T = \sum_k^{Q} Q_k(\mathbf{Px}_k, \mathbf{Py}_k)^T, \qquad (2.139)$$

where $\mathbf{Px}$ and $\mathbf{Py}$ are the x and y components of pressure gradient forces

computed through equation (2.138), respectively. Each of them has a length of Q. Then the hydrostatic pressure gradient term in the discrete momentum equation (2.42) takes the form $\mathbf{CP}$, where $\mathbf{P} \equiv (\mathbf{Px}, \mathbf{Py})^T$, and

$$\mathbf{C} \equiv \left(\begin{array}{cc} C' & 0 \\ 0 & C' \end{array} \right), \ C'_{ik} = \int_\Omega N_i Q_k \mathrm{d}\Omega, \ \text{for } 1 \le i \le \mathrm{N}, 1 \le k \le \mathrm{Q}. \quad (2.140)$$

A reference method for comparisons

To see the improvement in calculating pressure gradients with respect to accuracy provided by the suggested method, a comparison between it and a reference method is to be taken in the next section. As such the discontinuous Galerkin method used by Ford et al. (2004a) in their hydrostatic pressure solver is selected here. The discontinuous Galerkin representation of (2.137) is

$$\int_E [Q_k \partial_z \mathrm{P} - Q_k \mathrm{D}] \, \mathrm{d}\Omega^E + \int_{\{\Gamma^E : \mathbf{k} \cdot \mathbf{n} > 0\}} Q_k \mathbf{k} \cdot \mathbf{n} (\mathrm{P}_{in} - \mathrm{P}) \, \mathrm{d}\Gamma^E = 0, \quad (2.141)$$

where $\mathrm{P} \equiv 1/\rho_0 (\partial p/\partial x, \partial p/\partial y)^T$, $\mathrm{D} \equiv g/\rho_0 (\partial \rho/\partial x, \partial \rho/\partial y)^T$, $\mathbf{k}$ denotes the vertical unit vector as defined before. The second integration on the lhs represents the weakly imposed inflow boundary conditions (i.e., information from neighboring elements flowing in). The surface integration is restricted to the part on which $\mathbf{k} \cdot \mathbf{n} > \mathbf{0}$, which should be the upper face of each prism element in FEOM. On these boundaries, the value from the neighboring prism, denoted by P_{in}, is imposed. Substituting the discontinuous approximation (2.139) into (2.141) one gets the discretized equation for pressure gradient forces.

2.10.2   Experiments on pressure gradient errors

We take the popular seamount problem setup similar to that used by Beckmann and Haidvogel (1993) to compare the performance of the two pressure gradient force calculation methods described above. The bottom topography of the domain is defined as:

$$h(x,y) = H\{1 - \delta \exp[-(x^2 + y^2)/L^2]\} \quad (2.142)$$

where $H = 4500$ m is the depth away from the seamount, $L = 25$ km represents the horizontal length scale of the seamount, and δ defines the fractional height of the seamount. Two configurations, one with $\delta = 0.9$ and another with $\delta = 0.6$ are used as 'very steep' and 'moderately steep' cases, respectively. The origin of the (x, y) coordinates is at the center of the domain. The model domain is 512×512 km wide bounded with rigid walls. An f-plane approximation is made with Coriolis frequency 10^{-4} s^{-1}. The initial temperature profile is defined by

$$T(z) = 5 + 15 \exp(z/1000 \text{ m}), \quad (2.143)$$

and salinity is set to 35 psu. The initial density depends only on the vertical coordinate z and the flow is initially quiescent, so any motion developed with time should be considered as due to numerical errors. In order to estimate the performance of the pressure gradient force calculation methods, a background density profile is not subtracted here, although the background subtraction method is a practical choice in real applications. The model was run for 5 days with a time step of 10 minutes. It was found that analyzing simulation results over longer time intervals does not change the qualitative conclusions drawn below.
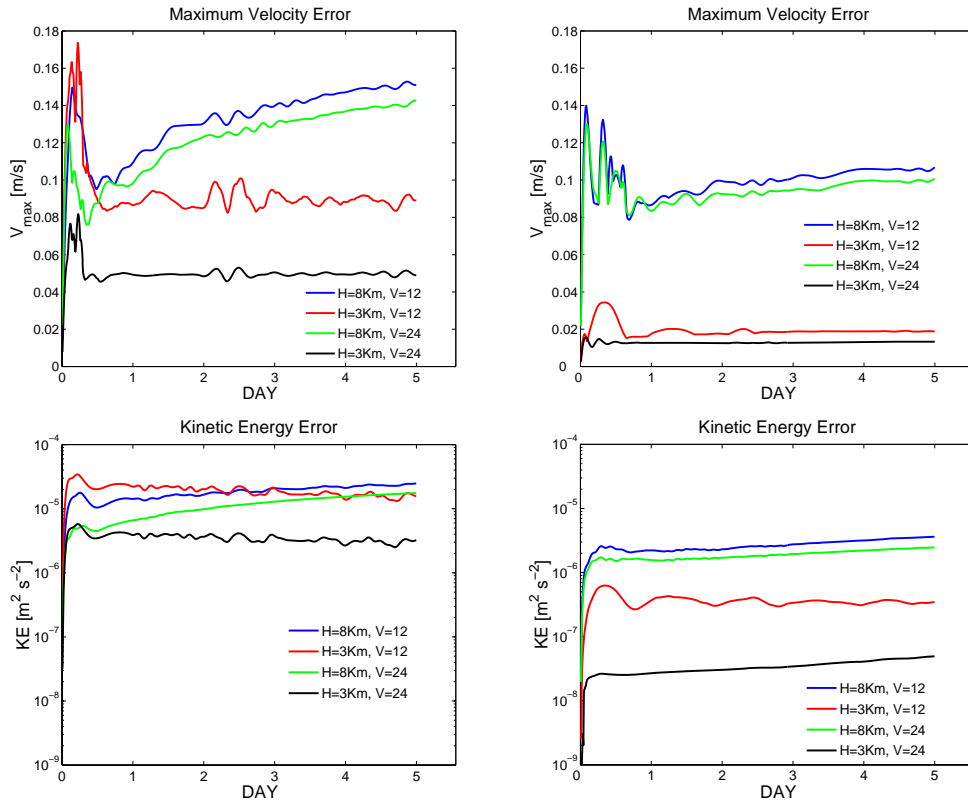
Figure 2.9: Time histories of maximum velocity (top) and kinetic energy (bottom) for the reference method (left) and nonlocal interpolation method (right) in the very steep seamount case ($\delta = 0.9$). Solutions for four different resolution combinations are shown. The kinetic energy is shown with a logarithmic scale.

Comparison between different methods

In the first set of experiments, solutions with different horizontal and vertical resolutions are obtained using the σ grid. Two horizontal resolutions (8 km and 3 km) and two vertical resolutions (12 and 24 equally spaced levels) are
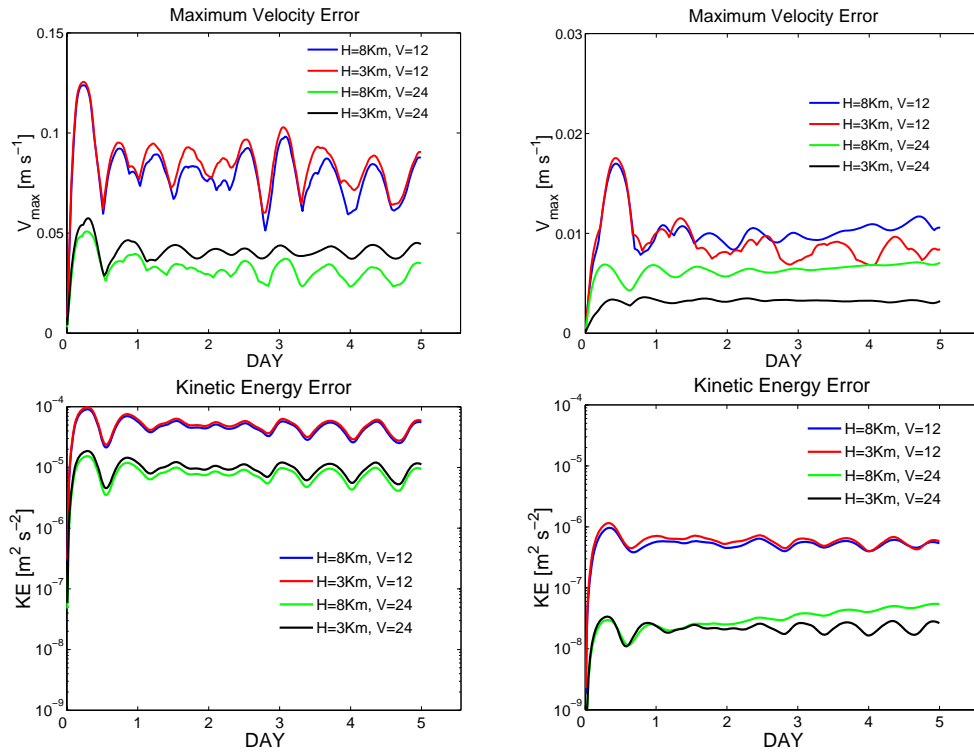
Figure 2.10: Same as Fig. 2.9 but for the moderately steep seamount case ($\delta = 0.6$). The kinetic energy is shown with a logarithmic scale. Notice that the limits of the vertical coordinate in velocity plots are not the same.

used. Both horizontal viscosity and diffusivity are set to 100 m^2 s^{-1}. Vertical viscosity and diffusivity are set to zero.

The time histories of maximum velocity and kinetic energy for the very steep and moderately steep cases are shown in Fig. 2.9 and Fig. 2.10, respectively. In both the very steep and moderately steep cases, the nonlocal interpolation method shows improved accuracy to the reference method at different resolutions with respect to both maximum velocity and kinetic energy. In the very steep case, the maximum velocity from the reference method is about 150% of that from the nonlocal interpolation method at the lowest resolution and more than 200% at the highest resolution. The kinetic energy from the reference method is about one order of magnitude higher than that from the nonlocal interpolation method at different resolutions.

The pressure gradient errors are reduced for both approaches when the seamount is lower. In the moderately steep case the nonlocal interpolation method shows much higher accuracy than the reference method. In this case, the maximum velocity from the reference method is about eight times higher than that from the nonlocal interpolation method at both the highest and lowest resolution, and kinetic energy is about two orders of magnitude higher
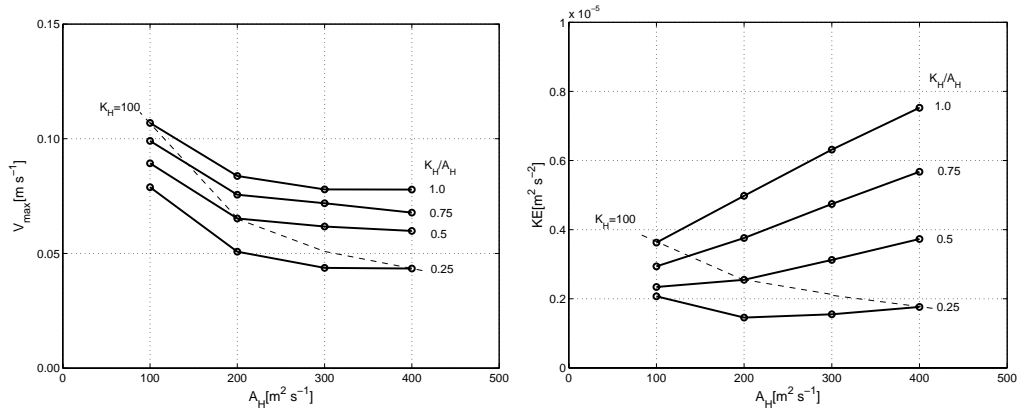
Figure 2.11: Sensitivity of maximum velocity (left) and kinetic energy (right) to horizontal viscosity and diffusivity. The solid lines show the relations at fixed diffusivity to viscosity ratios, and the dash lines show the the relations at fixed diffusivity values.

at different resolutions. By comparison between these two methods, it is clearly seen that the accuracy is dramatically improved when the nonlocal cubic spline interpolation method is employed.

Comparing our results with those of Ezer et al. (2002) shows that using the interpolation method one generally obtains model accuracy at the level of up-to-date approaches used with FD models. Note again that this interpolation method is only possible on grids in which 3D nodes are generated by dropping vertical lines from surface nodes down to the bottom. For a fully 3D unstructured grid more complicated schemes are required. The reference method (Ford et al., 2004a) used here can also be applied on fully unstructured grids, although its accuracy is lower than the nonlocal interpolation method as illustrated above.

Sensitivity to resolution and dissipation

The sensitivity of errors to resolution when using the nonlocal interpolation method can also be seen in Figs. 2.9 and 2.10. Although in both seamount configurations the errors decrease with increased resolution, horizontal and vertical resolutions play different roles in different situations. In the very steep case, the accuracy is more sensitive to horizontal resolution, whereas in the moderately steep case it is more sensitive to vertical resolution. Doubling the vertical resolution only slightly increases the accuracy in the former case, whereas in the latter case it reduces the errors by about 40% and one order of magnitude with respect to maximum velocity and kinetic energy, respectively. Increasing the horizontal resolution from 8 km to 3 km reduces the maximum velocity to about one fifth and the kinetic energy by one order of magnitude in
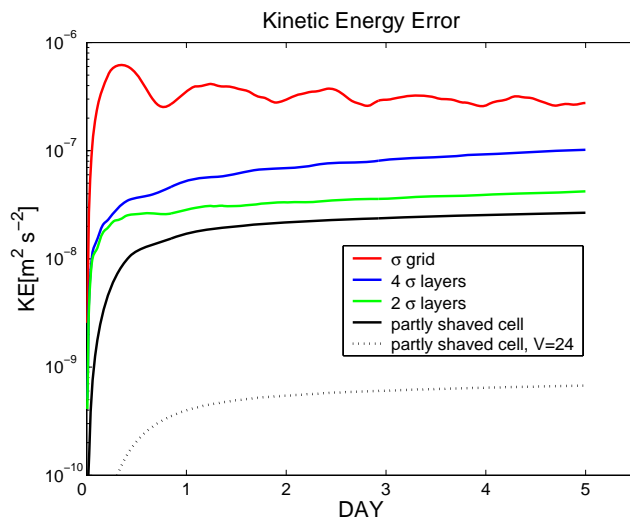
Figure 2.12: Time histories of kinetic energy for different grids in the very steep seamount case. Viscosity is 100 m^2 s^{-1} and diffusivity is 25 m^2 s^{-1}. Horizontal resolution is 3 km. Cases with 12 vertical levels are plotted with solid lines and cases with 24 vertical level with dotted lines.

the former case, whereas it keeps the accuracy almost unchanged in the latter case. In both cases, increasing horizontal and vertical resolution together can most efficiently increase model accuracy.

The sensitivity of spurious velocity and kinetic energy to the value of the horizontal viscosity and diffusivity is displayed in Fig. 2.11. The solutions are taken after five days simulations on a σ-grid with horizontal resolution of 8 km and twelve active levels in the vertical. Only a range of viscosity and diffusivity commonly used at this resolution is studied. For each fixed viscosity an increase in horizontal diffusivity results in an increase in numerical errors with respect to both erroneous velocity and kinetic energy. When the ratio of horizontal diffusivity to viscosity is fixed, maximum spurious velocity decreases when viscosity is increased, whereas kinetic energy increases. However, at fixed diffusivity an increase in horizontal viscosity leads to a decrease in both maximum velocity and kinetic energy. And at lower viscosity a relatively stronger sensitivity is observed. The opposite effects of horizontal viscosity and diffusivity on accuracy in this range of values are consistent with the finding by Mellor et al. (1998).

Errors on different grids

Pressure gradient errors are a long standing problem in σ grid models and cannot be eliminated with the up-to-date techniques as demonstrated above and in previous studies (Ezer et al., 2002; Shchepetkin and McWilliams, 2003). With the recently improved techniques the errors can only be reduced to some

level which can be acceptable in some specific applications.

There are pressure gradient errors in all layers on a σ grid. Compared to the pure σ grid, the $z + \sigma$ grid has only sources of pressure gradient errors in elements where σ levels are used. The (partly) shaved cell grid has pressure gradient errors only within the bottom shaved elements. This is similar to the situation with partial cell grid in GFDL MOM (Pacanowski and Gnanadesikan, 1998). Fig. 2.12 shows time histories of kinetic energy on different grids. The less sigma levels are used, the smaller the spurious kinetic energy. On the partly shaved cell grid the kinetic energy is one order of magnitude smaller than on the σ grid. The partly shaved cell grid shows very strong sensitivity to vertical resolution.

Although the spurious kinetic energy is dramatically reduced with less σ layers used, the erroneous maximum velocity does not necessarily so. This is because errors from the calculation of density gradients are not reduced in the individual elements of employed σ or shaved layers.

The comparison between the performance of different grids with respect to pressure gradient errors provides some basic ideas that we should keep in mind when we choose vertical grids in real applications.

Remark

In the above tests the CG advection scheme is used. As illustrated in section 2.6.2 different schemes can have different accuracy in approximating solution fields. The implicit diffusion and/or the property of monotonicity associated with a specific scheme can influence the quantitative results given above. The CG scheme is less able to constrain maximum/minimum among the schemes available in FEOM and was therefore selected.

2.11   Summary

The main principles of the FEOM code which works with prismatic elements are presented. The implementation of the CBS method in the dynamical part is explained. This method provides stabilization for advection and surface elevation modes, resulting in robust code performance. A key element in this method is the presence of tunable parameter γ. It controls the strength of stabilization of pressure modes and allows to keep the numerical dissipation of the algorithm on a relatively low level.

The space of functions selected for tracer fields defines the possible selection of advection schemes. We described the CG method and its FCT variant. Comparison of the advection schemes shows that the FCT scheme is generally more robust. The implementation of the rotated Redi diffusivity tensor and GM skew flux is also described.

One important feature of the code is its support for different vertical discretization. It is based on two issues. The first one is the nonlocal interpolation

algorithm to compute pressure gradient forces. It is shown that the algorithm leads to relatively small errors comparable to those of FD σ models. The second one is to treat irregular elements especially when there are coalesced nodes.

The essential part of the new version FEOM, including the support for different vertical discretization and the selection and design of numerical algorithms, was implemented and tested by the author.

Chapter 3

Flow over an isolated seamount

A flow past a seamount in a rotating channel represents a standard test bed for studying the performance of models with respect to their skill in representing the topography. Eddy formation and shedding observed under some particular conditions (Chapman and Haidvogel, 1992) is the consequence of topography-induced dynamics. Internal lee waves can be generated by the seamount in some situation (Chapman and Haidvogel, 1993). By simulating these processes the performance of different vertical discretization is studied here.

3.1 Background

When a flow is applied to a rotating channel with a seamount at the center, eddy formation, eddy trapping and eddy shedding can be observed under some particular conditions (Chapman and Haidvogel, 1992). Under some set of physical parameters two eddies form over the seamount when a flow is impulsively started. One of them is swept downstream as a cyclonic vortex, leaving another trapped over the seamount to form a Taylor cap.

Besides the influence of background stratification, seamount height and the inflow strength in terms of the Rossby number, the impact of internal lee waves on Taylor caps was also studied by Chapman and Haidvogel (1992). The conditions influencing the generation of internal lee waves were further investigated in Chapman and Haidvogel (1993). When the speed of background flow is not sufficient to support internal lee waves away from the seamount, large-amplitude lee waves can still form owing to a large local acceleration of the flow by nonlinear advection of momentum in the existence of the seamount. These waves are trapped over the flank of the seamount where the local acceleration occurs, weaken in the downstream direction, and can finally be quickly dissipated by subgrid scale mixing.

The seamount configuration was taken by Adcroft et al. (1997) in studying the performance of their shaved cell algorithm. The eddy formation and shedding processes were better reproduced when topography was represented with shaved cells than with full cells. Ford et al. (2004b) employed this experimental

setup as a validation for their nonhydrostatic FE model (ICOM, Ford et al., 2004a). They carried out model intercomparisons and examined the model sensitivity to resolution. The collection of works based on the seamount geometry provides a reference, upon which a qualitative intercomparison with results from the current work can be made.

It is desirable for ocean models to be capable of faithfully simulating physical processes induced by seamount topography. One of the climate relevant phenomena that could be tightly related with the impact of seamount topography is the formation of Weddell Polynya. Although consensus has not yet been reached concerning the dominant mechanism responsible for observed ice thinning in the vicinity of the Maud Rise, many studies indicate that topography induced effects play an important role. The study of Holland (2001a,b) suggests that the cyclonic eddy shed off the Maud Rise be the dynamical origin of the formation of Weddell Polynya. Beckmann et al. (2001) argued that the tidal amplification owing to the seamount can lead to polynya formation.

Besides the task of studying the performance of several types of vertical discretization available in FEOM, our goal in this and subsequent sections is also to demonstrate the model's overall skill.

3.2 Model setup

A Gaussian seamount was placed at the center of a zonally re-entrant channel of width and length equal to 512 km. The bottom topography of the domain is defined by equation (2.142), with $H = 4500$ m and $L = 25$ km. The (x, y) coordinates are referenced to the center of the domain. Two different seamount fractional height δ are used. It is 0.9 in the simulation of eddy formation and shedding by impulsively applied barotropic flow, and 0.5 in the simulation of internal lee waves. An f-plane approximation is made with the Coriolis parameter equal to 10^{-4} s^{-1}. The applied flow is characterized by two nondimensional numbers, the Rossby number

$$\mathrm{Ro} \equiv \frac{\mathrm{U}}{fL}, \tag{3.1}$$

and the Burger number

$$\mathrm{Bu} \equiv \frac{NH}{fL}, \tag{3.2}$$

where U is the initial barotropic (uniform) flow velocity and N the buoyancy frequency. The initial temperature field is linearly stratified (constant N) and the linear equation of state is used. The periodic boundary condition is augmented by a narrow restoring zone of 50 km with a restoring timescale of 1 h. The sponge zone is far enough from the seamount and does not influence the physics around the seamount. Yet it supplies sufficient force to balance the decelerating form drag exerted by the seamount.

The horizontal resolution of the meshes is 3 km above the seamount, and then increases to about 8 km at the boundary. There are twelve equally spaced vertical layers in the σ grid. In the z-level grids, twelve active levels in the vertical are used, the level thickness of which is 375 m except in the bottommost shaved elements when they are used. Two σ layers are employed when generating the $z + \sigma$ grid, in which the thickness of the σ layers is set close to that in the σ grid with slight adjustment when needed. The surface mesh in the fully shaved cell grid is adjusted to enable a fully piecewise linear smooth bottom representation, but the resolution is maintained as close as possible to that in other grids. The resolution used in this set of simulations was chosen such that the physical process can be properly simulated according to the sensitivity study of Ford et al. (2004b).

Diffusivity and viscosity are 25 m^2 s^{-1} and 100 m^2 s^{-1}, respectively. The current work and the study of Ford et al. (2004b) applied the Laplacian dissipation, whereas in most other references the fourth order operator for horizontal mixing has been used. The advection scheme used here, the Characteristic Galerkin method, is different from that used in other studies too. Due to all the differences in numerics, it is only possible to make qualitative comparison between different models. The purpose of this work is to investigate the effect of vertical grids, so the influence of physical parameters as studied by Chapman and Haidvogel (1992, 1993) is not addressed here.

3.3   Eddy formation and shedding

Burger number Bu = 1.5 and Rossby number Ro = 0.1 are used in the first set of experiments following the studies cited above. When a barotropic flow is impulsively applied to this domain, an anticyclonic and a cyclonic eddies are formed, the latter of which is to be shed off the seamount in the downstream direction as time proceeds. A simulation with the sigma grid is made first as a reference experiment. The density field at the depth of 4000 m and the vertically integrated relative vorticity $\hat{\zeta}/f$ in the σ grid simulation are presented in Fig. 3.1 and Fig. 3.2, respectively.

The process of eddy formation, shedding and advection is well modeled in the σ grid. There is a positive density anomaly around the seamount and a negative density anomaly downstream, the former is associated with the anticyclonic eddy, and the latter is associated with the cyclonic vorticity. The eddy shedding can be seen clearly from the fourth day. As the cyclonic eddy is advected downstream, a tail of cyclonic vorticity between the seamount and the cyclonic eddy is formed. There is a good qualitative agreement to the results by Ford et al. (2004b) with respect to these features. There is quantitative difference in the magnitude of relative vorticity from the results in Adcroft et al. (1997). This can be partly attributed to the difference in numerics (i.e., the dissipation and advection schemes) between FEOM and MITgcm. It thus

emphasizes the necessity of using a model with the same numerics to isolate
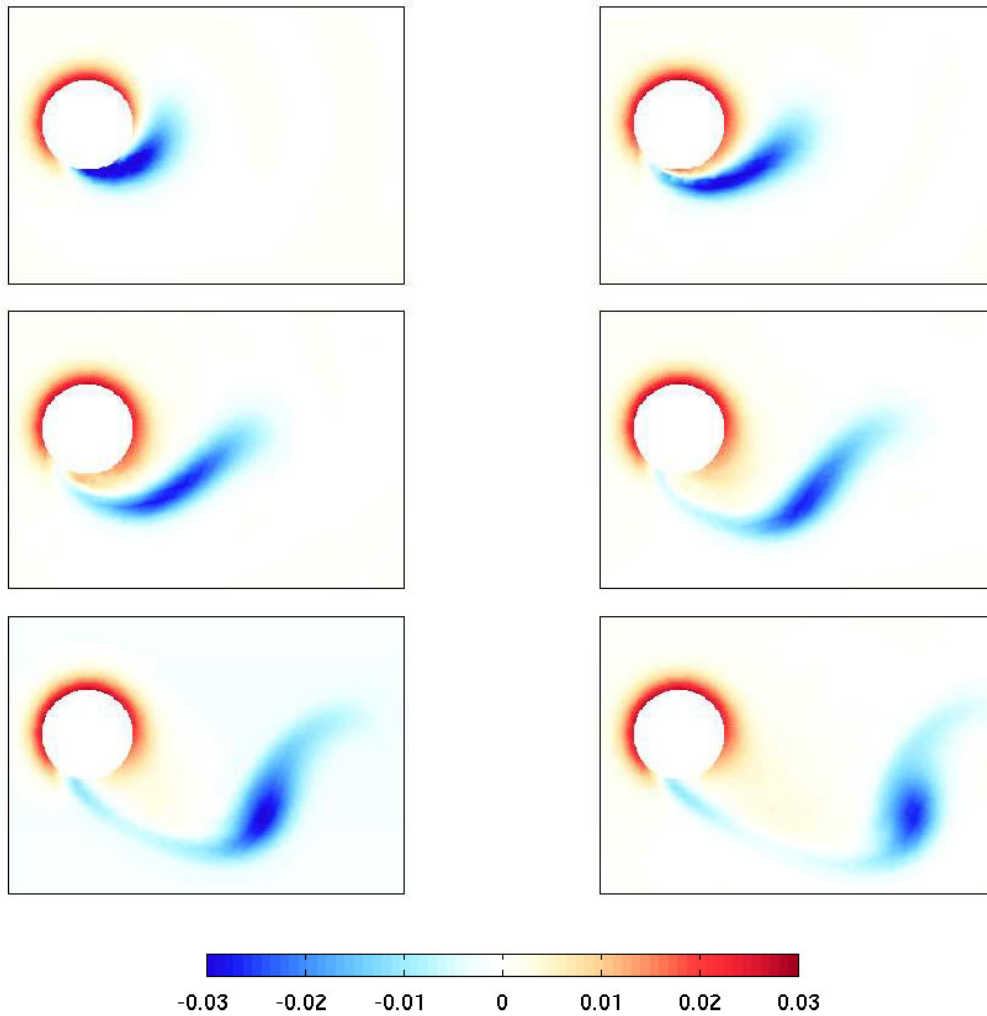the effect of topography representation.

Figure 3.1: Density anomaly at the depth of 4000 m after 2, 4, 6, 8, 10,
and 12 days in the σ grid simulation. The region of model domain shown is
-64 km $\leq x \leq 256$ km, -128 km $\leq y \leq 96$ km.

The density and relative vorticity fields from the $z + \sigma$, full cell, partly
shaved cell, and fully shaved cell grid simulations are shown in Figs. 3.3
and 3.4, respectively. All these approaches manage to model the process of
eddy formation, shedding and advection to some extent. Among these four
approaches, the full cell z-level simulation has the most significant difference
to the sigma simulation, while the others differ from the σ simulation only in
some details.

    The full cell z-level solution features a lot of small scale noise in the vicinity
of the seamount in both the density and relative vorticity fields due to the
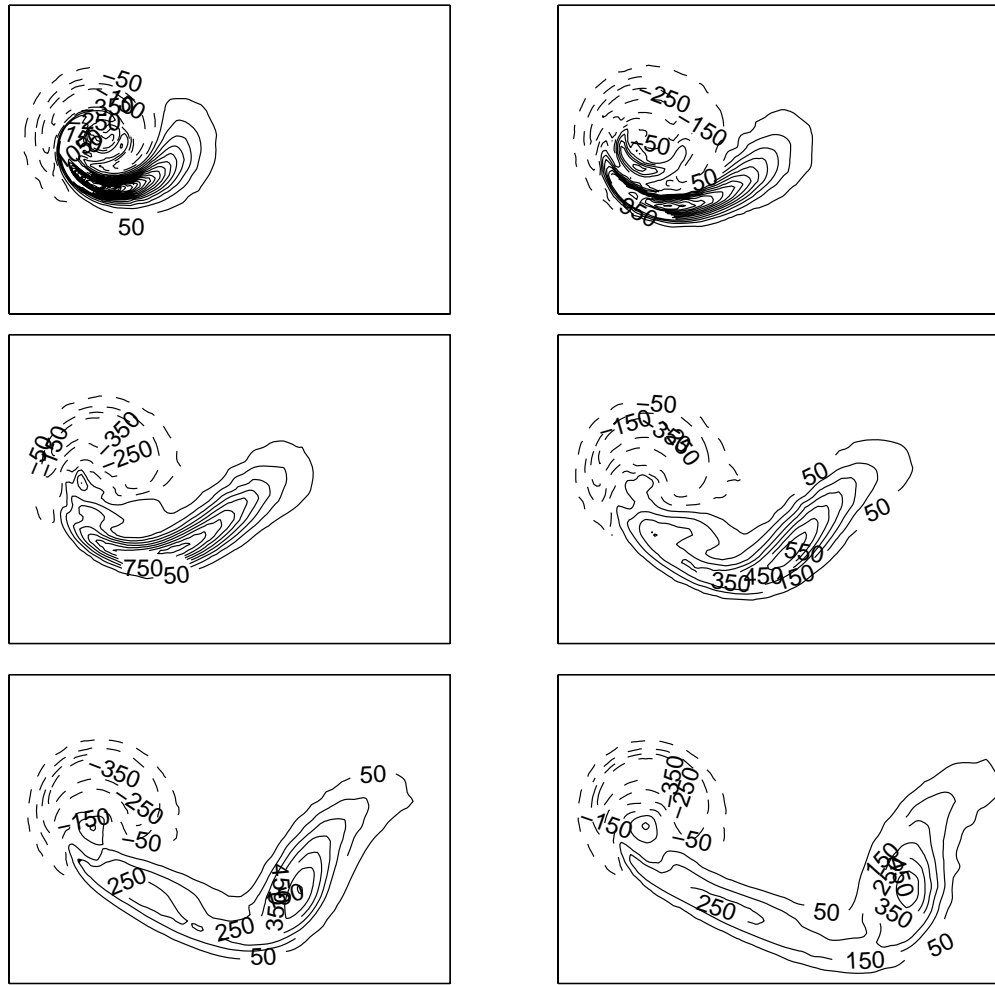
Figure 3.2: Nondimensional vertically integrated relative vorticity $\hat{\zeta}/f$ after 2, 4, 6, 8, 10, and 12 days in the σ grid simulation. Contour interval is 100. The domain shown is the same as in Fig. 3.1.

discontinuities in representing the bathymetry. This can be a more serious issue because unstructured triangular surface meshes are used and hence multiple zig-zag features are created in the three dimensional view. The downstream advection of the cyclonic eddy with time is weaker than on the other grids, and a stronger downstream stretching of the anticyclonic eddy is simulated. The artificial wide cyclonic vorticity positioned off the northeastern flank of the seamount in the full cell z-level simulation in Adcroft et al. (1997) is not observed here. Instead, there are only some small cyclonic eddy spots at the inflow side. Another simulation on the full cell grid with increased horizontal resolution indicates that the model performance is not improved at all (not shown). The explanation for this is that the model topography does not converge to the Gaussian seamount at fixed vertical resolution, see Fig.
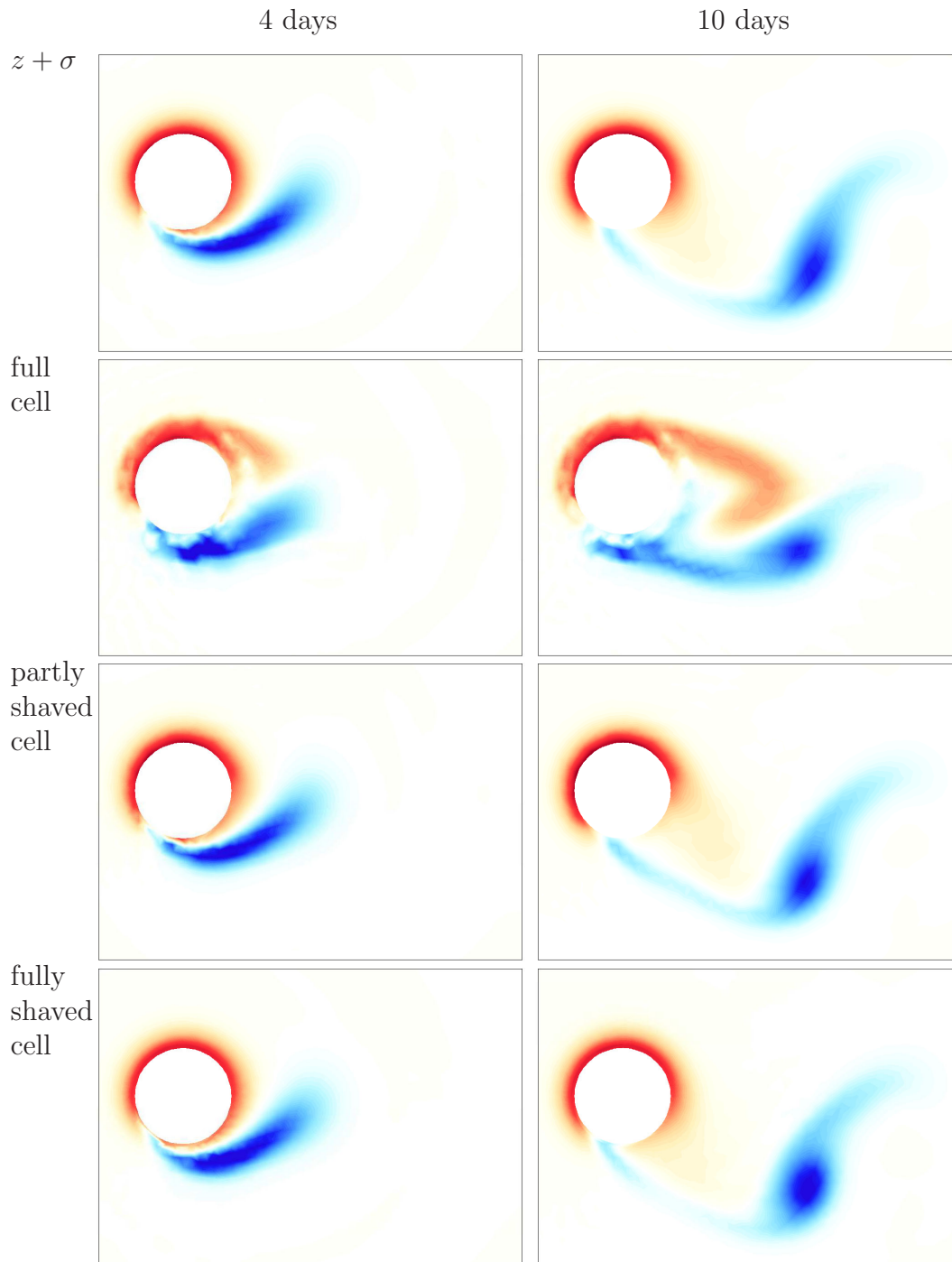
Figure 3.3: Density anomaly at the depth of 4000 m after 4 (left) and 10 (right) days in the (top to bottom) $z + \sigma$, full cell, partly shaved cell, and fully shaved cell grid simulations. The domain and colorbar are the same as in Fig. 3.1. The full cell case shows the strongest deviation from other types of grids. Except for the full cell grid, all other grids represent the process of eddy formation and shedding properly.
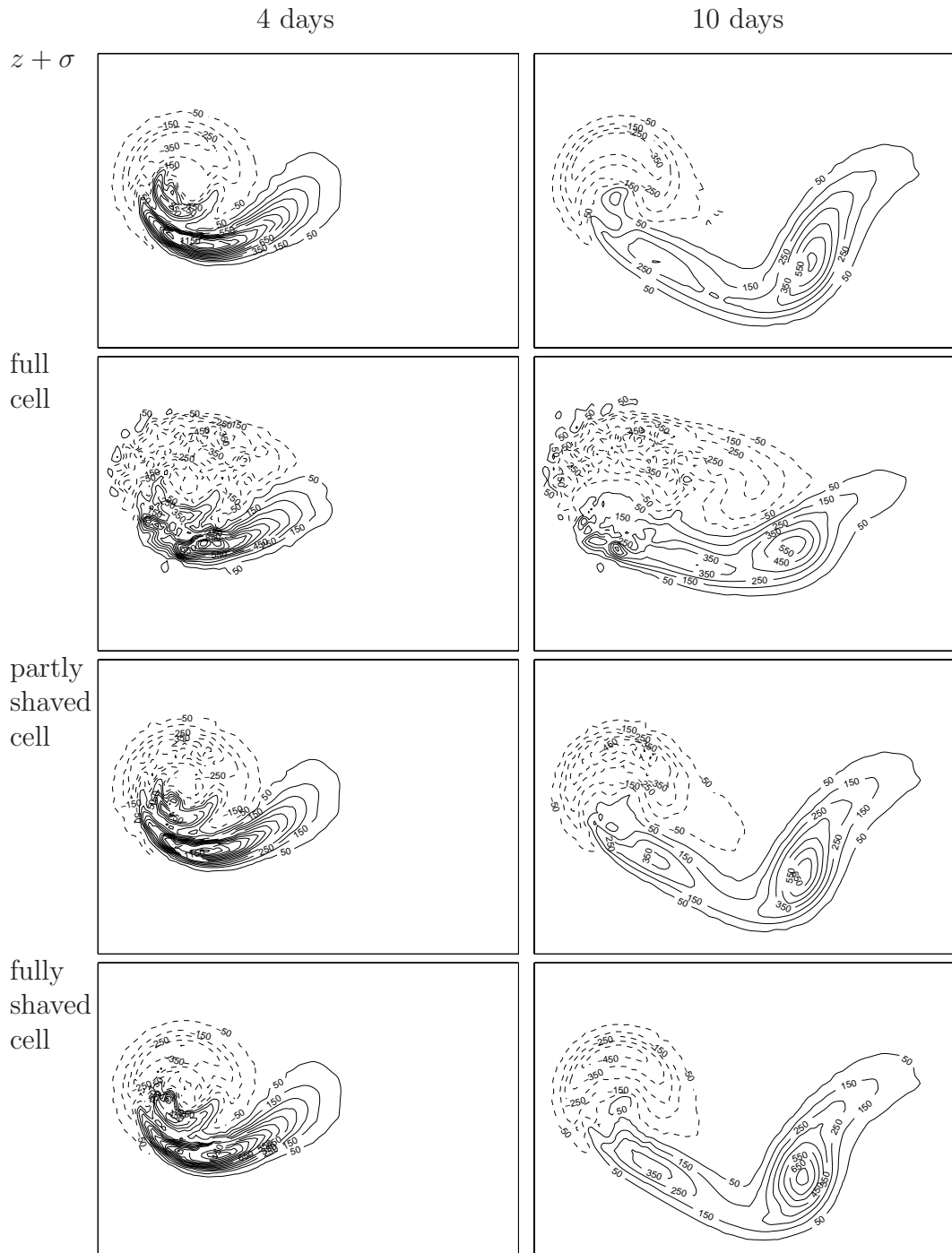
Figure 3.4: Nondimensional vertically integrated relative vorticity $\hat{\zeta}/f$ after 4 (left) and 10 (right) days in the (top to bottom) $z + \sigma$, full cell, partly shaved cell, and fully shaved cell simulations. Contour interval is 100. The domain shown is the same as in Fig. 3.1. The $z + \sigma$ results agree well with the σ results even in a quantitative sense. The full cell grid produces a lot of small-scale perturbations above the seamount, and the shape of both the cyclonic and anticyclonic vortices is clearly different from those on other grids. The (negative and positive) magnitude of the relative vorticity is similar on the partly and fully shaved cell grids, and is larger than on the σ and $z + \sigma$ grids by about 100.

1.4 and the discussion in Adcroft et al. (1997).

The $z + \sigma$ grid solution follows the σ simulations in almost all details quantitatively. The major visible difference is the slightly larger downstream side extension of the anticyclonic eddy. The partly shaved cell grid reproduces a very similar solution. By comparison with the full cell z-level approach, the model performance is considerably improved in this case. However, there are still some slightly unsmooth features in the relative vorticity field above the seamount due to preserved stepwise representation in some regions of very steep topography. There is about a value of one contour interval difference in the magnitude of the anticyclonic and the tail of cyclonic vorticity between the partly shaved cell grid and sigma grid. This can be attributed to the difference in their local vertical resolution in the vicinity of the seamount.

The model performance can further be improved when we adjust surface triangle meshes to fully eliminate stepwise representation of the topography. Small scale noise is absent in this case, yet the magnitude of the anticyclonic vorticity and the tail part of the cyclonic vorticity is quite similar to that of the partly shaved cell solution. This is because they have similar local vertical resolution, which is different from in the σ and $z + \sigma$ cases.

In order to look at the details of the effects of vertical grids, we take the density field at the depth of 400 m. The density anomaly at this depth due to the steering effect of the topography at the initial transient response stage is only in the vicinity of the seamount, therefore, the difference between different vertical discretization can be demonstrated more clearly. The Burger number $Bu = 1.0$ is now used in this set of experiments to match prior studies. Fig. 3.5 shows the density field at the depth of 400 m after 1 and 2 days simulation. The vortex pair on the seamount is well modeled. By comparison with the solution fields of Chapman and Haidvogel (1992) and Ford et al. (2004b), there is a quite good qualitative agreement between different models. Quantitatively, the range of values of density at this depth also agrees with previous studies. The density anomaly ranges between -0.0071 and 0.0305 kg m^{-3} in the current simulation, which is quite close to the range of 0.0350 kg m^{-3} in the study of Ford et al. (2004b). Comparing with the solution fields in Ford et al. (2004b), the difference caused by hydrostatic approximation adopted in our model is not obvious in this experiment configuration. It can be concluded that the current simulation with σ grid agrees with previous studies despite the differences in numerics and dissipation parameters.

Fig. 3.5 also shows the simulation with the $z + \sigma$ grid. It produces most features of the sigma results, because the local resolution in the vicinity of the seamount top is the same in both types of grids. There is only a small shift in the range of density distribution, which is -0.0068 to 0.0324 kg m^{-3} in the $z + \sigma$ simulation. The density fields from other approaches are shown in Fig. 3.6. The full cell z-level grid is the least successful in resembling the sigma simulation, due to its discontinuous representation of the topography. Although it also manages to model the double eddy feature, the range of the
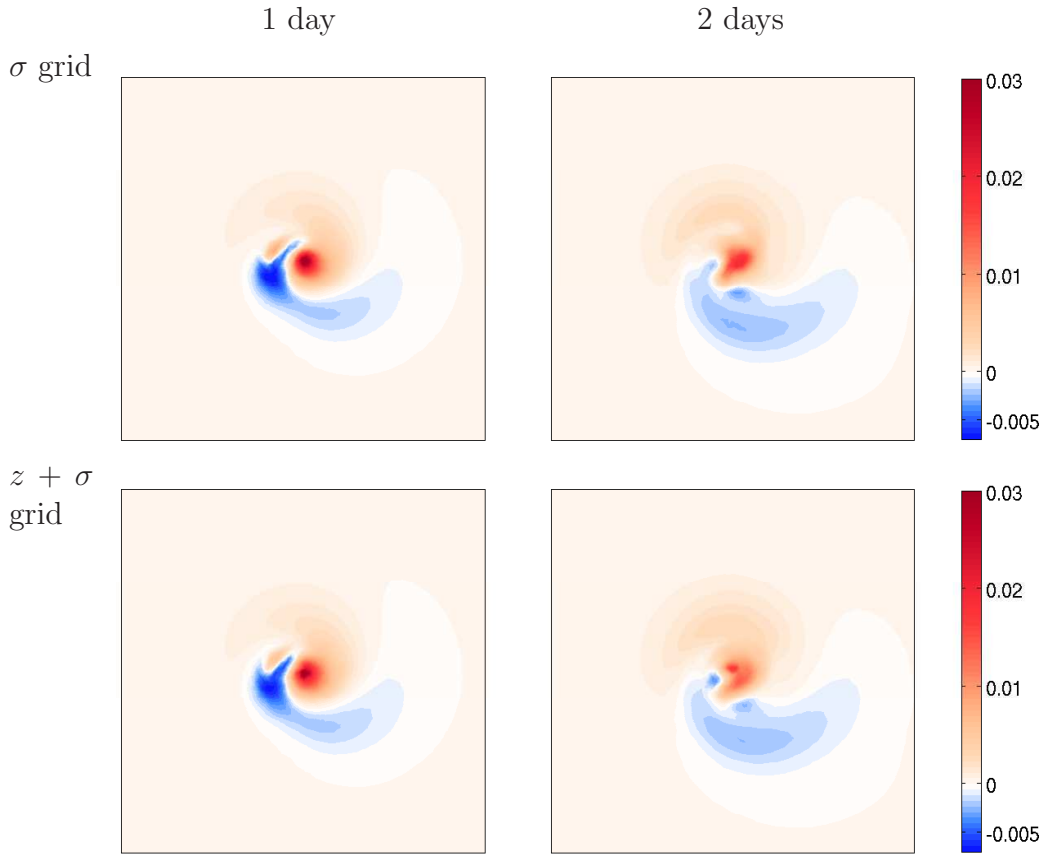
Figure 3.5: Density anomaly at the depth of 400 m after 1 (left) and 2 (right) days in the σ grid (top) and $z + \sigma$ (bottom) simulation. The region of the model domain shown here is -96 km $\leq x \leq 96$ km, -96 km $\leq y \leq 96$ km. The solutions on the pure σ grid and on the $z + \sigma$ grid are very similar to each other.

density anomaly, from -0.0072 to 0.0127 kg m^{-3}, is much smaller than that in the σ simulation. The results from partly and fully shaved cell grids are quite similar to each other in a quantitative sense. Their density anomalies range from -0.0078 to 0.0245 kg m^{-3} and from -0.0072 to 0.0247 kg m^{-3}, respectively. Both approaches lead to more reasonable values than the full cell approach.

When looking at the details of eddy patterns, the improvement to the partly shaved cell grid by employing fully shaved cell grid is clear: the small scale noise presented in the partly shaved cell solution disappears because there is no more discontinuities in the presentation of bathymetry. The remaining quantitative difference between the σ approach and the shaved cell approach is mainly due to the difference in the local vertical resolution.
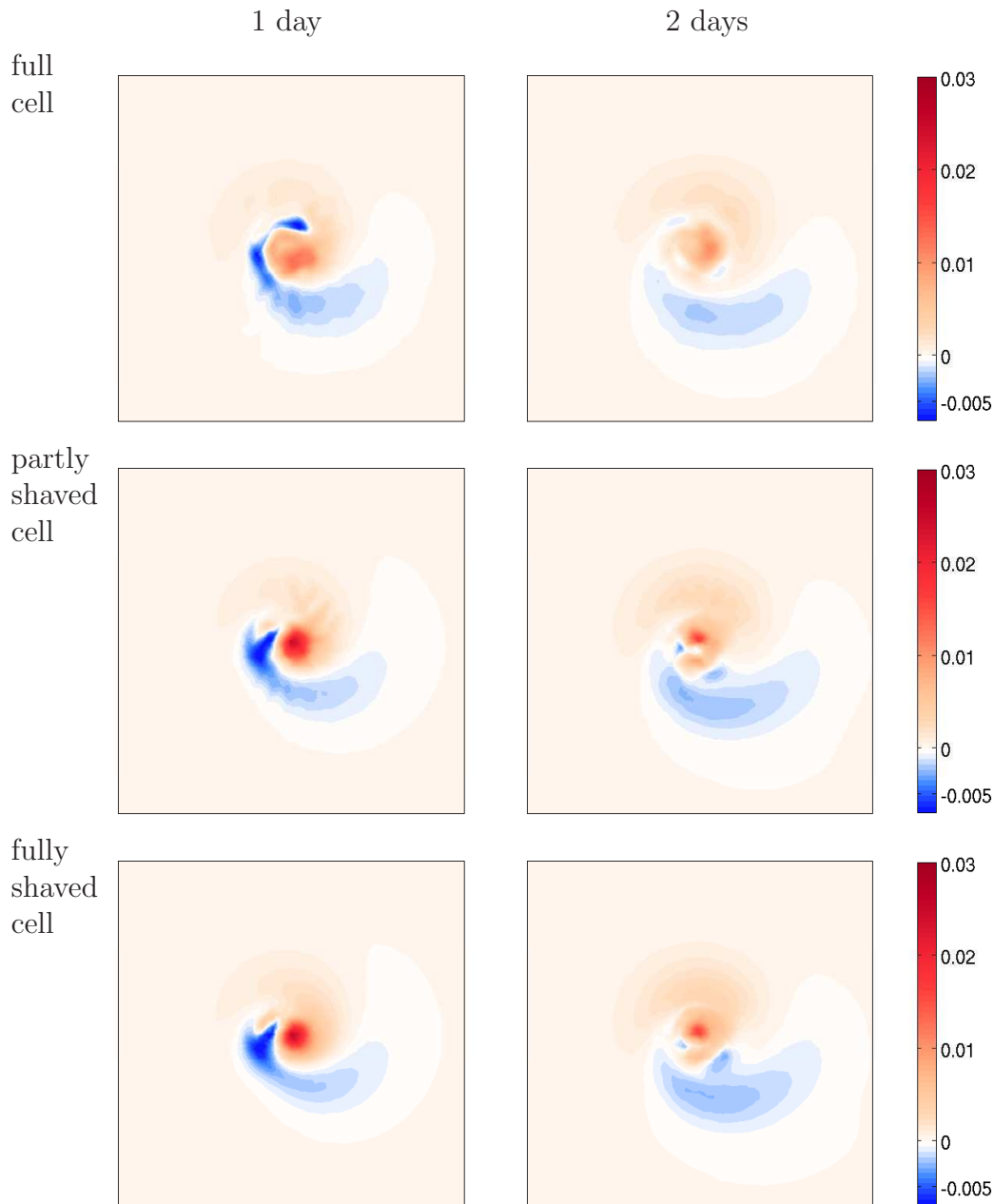
Figure 3.6: Density anomaly at the depth of 400 m after 1 (left) and 2 (right) days in the (top to bottom) full cell, partly shaved cell, and fully shaved cell simulations. The domain shown is the same as in Fig. 3.5. The full cell grid produces a much smaller positive density anomaly. Results on the full cell grid deviate from the σ solution more than on other grids. The solutions on the partly and fully shaved cell grids resemble those on the σ grid, but magnitudes are slightly smaller. Small-scale noise on the partly shaved cell grid is still present.

3.4 Internal lee waves

To further demonstrate the effects of vertical grids, the internal lee waves are simulated with the Gaussian seamount configuration. We investigate to what an extent the lee waves can be influenced by the choice of vertical grids. For sufficiently small seamount and sufficiently large Fround numbers,

$$\text{Fr} \equiv \frac{\text{Ro}}{\text{Bu}}, \tag{3.3}$$

a significant field of stationary internal lee waves can be found downstream the seamount when the flow is in a steady state (Chapman and Haidvogel, 1993). In the current work we take the fractional seamount height $\delta = 0.5$, the Rossby number Ro $= 0.2$, and the Burger number Bu $= 1.0$. Hydrostatic approximation is adequate in this configuration bearing in mind that the vertical length scale is less than one tenth of the horizontal scale.

Fig. 3.7 shows the density field after 24 days in the zonal section across the seamount center. Fig. 3.8 shows the zonal and horizontal sections of the density anomaly and vertical velocity. Well defined patterns of trapped stationary internal waves in the region downstream of the seamount can be observed in these sections. The solution agrees qualitatively with results of previous studies by Chapman and Haidvogel (1993) and Ford et al. (2004b). The internal waves trapped to the seamount are enhanced in the region where local acceleration of current takes place. These well modeled features on the σ grid provide the benchmark for comparison with other grid solutions.

Figs. 3.9 and 3.10 show the solution fields after 24 days from runs on other grids. Except for the full cell grid, all other approaches manage to simulate the internal lee waves. The full cell simulation gives completely different solutions without internal lee wave structures, which are dominated instead by small scale noise caused by artificial ridges in the topographic representation. The smaller vertical velocity and density anomaly is mainly due to dissipation, which works more efficiently on small scales induced by artificial ridges. The $z + \sigma$ solution resembles most of the σ solution, only possessing small quantitative difference in magnitude. Both the modified z-level approaches (partly and fully shaved cell grids) represent internal lee waves in a qualitative agreement with sigma solutions, but show about 30% of difference in the magnitude of vertical velocity to the σ and $z + \sigma$ solutions. This is caused by the difference in local resolution where the strongest wave energy locates. Compared with the fully shaved cell approach, the partly shaved cell grid solution has some small scale noise at the upstream side of the seamount, which can be observed in both the zonal and horizontal sections of the vertical velocity fields.
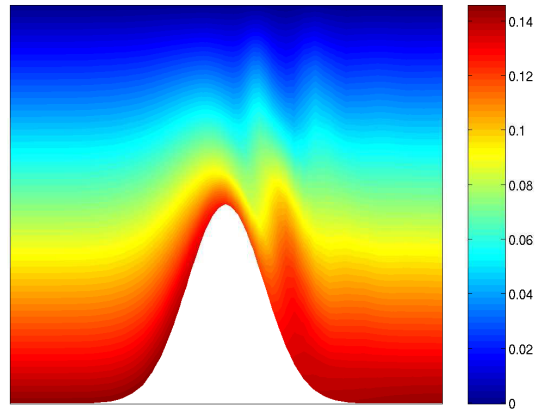
Figure 3.7: Density field in the along-stream section passing through the seamount center in the σ run. The zonal range of -100 km $\leq x \leq 100$ km is shown.
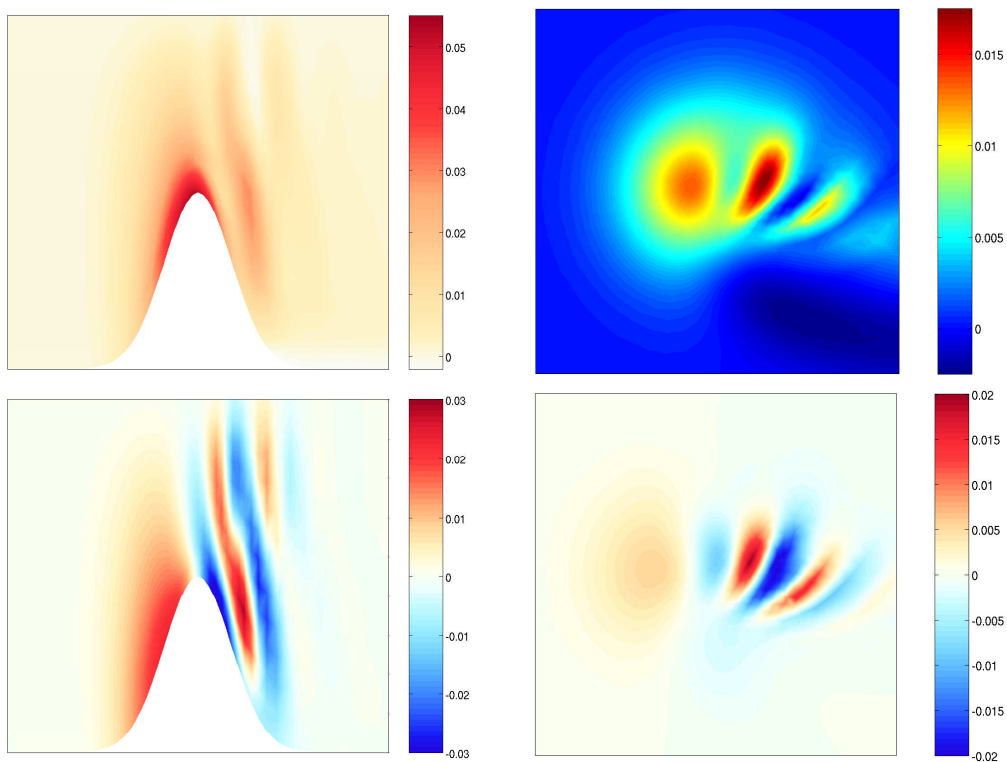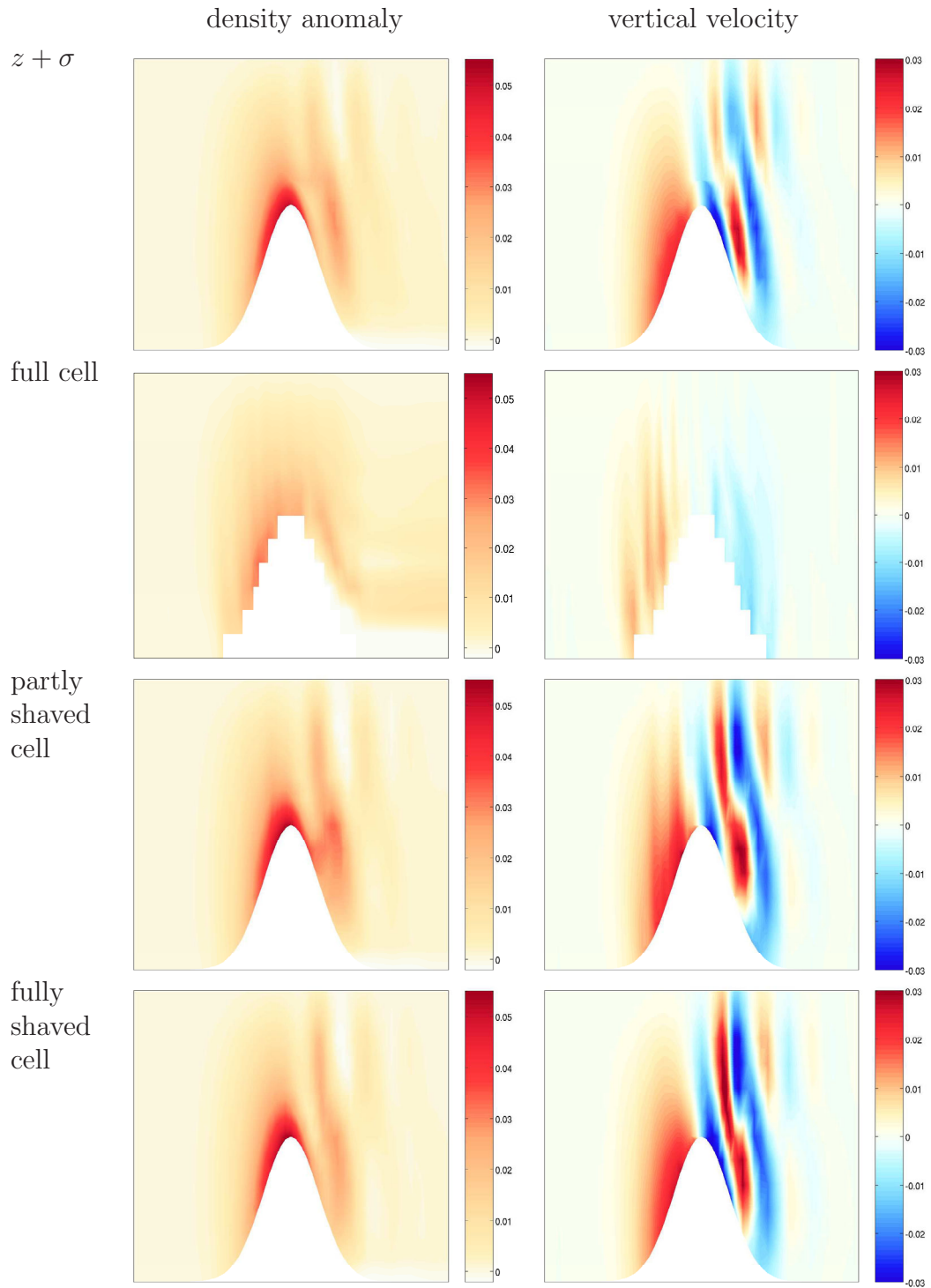

Figure 3.8: Density anomaly (top) and vertical velocity (bottom) fields in the along-stream section passing through the seamount center (left) and in a horizontal section at the depth of 1125 m (right) in the σ run. In the left panel the same zonal range as in Fig. 3.7 is shown, and in the right panel the domain is -64 km $\leq x \leq 64$ km, -64 km $\leq y \leq 64$ km.

density anomaly   vertical velocity

Figure 3.9: Density anomaly (left) and vertical velocity (right) fields in the along-stream section passing through the seamount center in the (top to bottom) $z + \sigma$, full cell, partly shaved cell, and fully shaved cell simulations. Domain shown is the same as in Fig. 3.7. The full cell grid can not represent the internal lee waves, instead it produces spurious fields associated with the discontinuous topography representation. Other grids reproduce lee waves properly. Note that noise due to partly discontinuous bottom representation on the partly shaved cell grid can be observed in the vertical velocity field at the upstream side of the seamount.
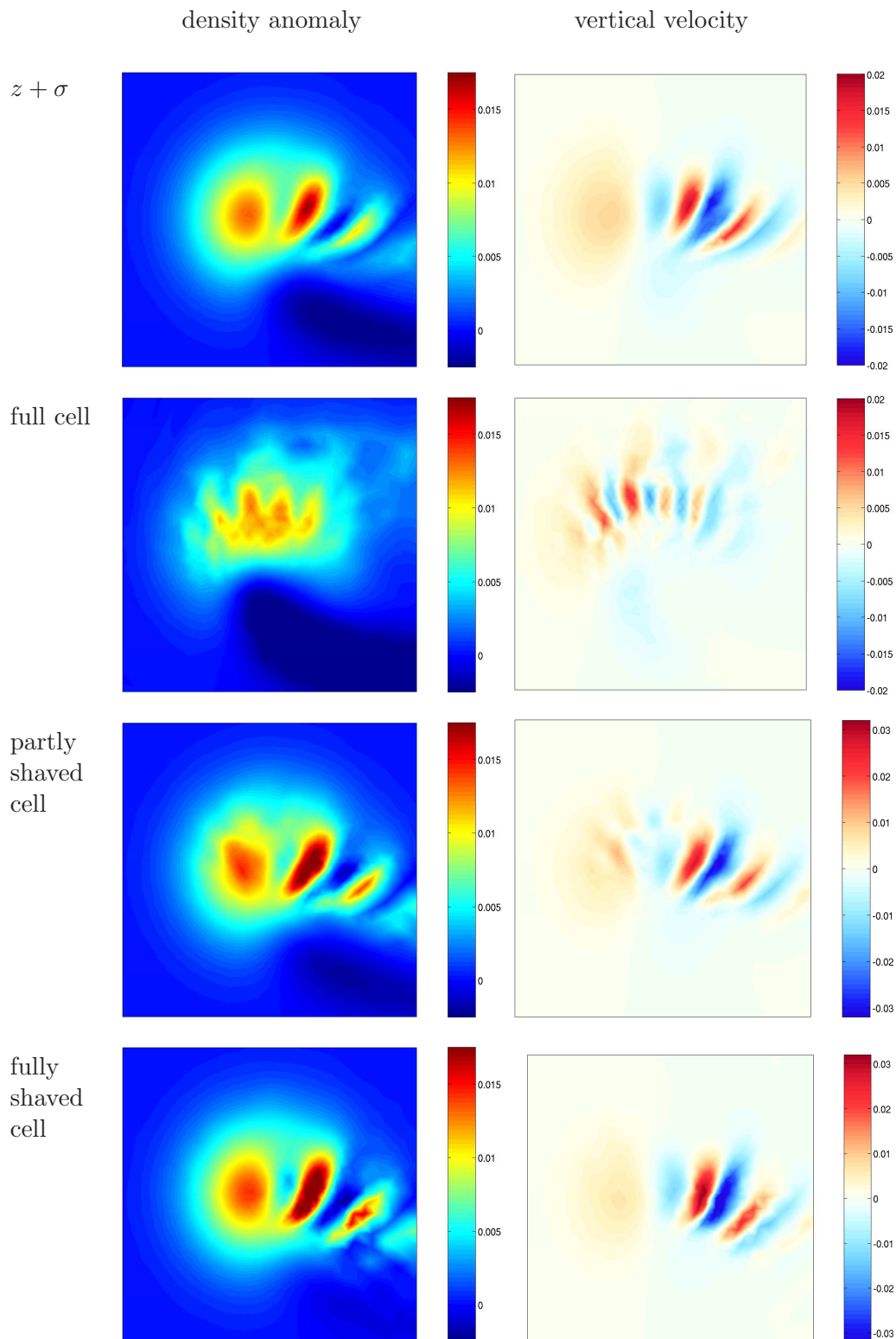
Figure 3.10: Density anomaly (left) and vertical velocity (right) fields at the depth of 1125 m in the (top to bottom) $z + \sigma$, full cell, partly shaved cell, and fully shaved cell simulations. Domain shown is the same as in Fig. 3.8. The solution on the full cell grid is dominated by grid noise. Vertical velocities on the partly and fully shaved cell grids are similar, yet they are slightly larger than those on the σ and $z + \sigma$ grids.

3.5   Summary

In this chapter the performance of different vertical grids has been studied via simulations of steadily forced flow past an isolated seamount. The process of eddy formation and shedding, and the characteristics of trapped internal lee waves as well, are faithfully simulated on the σ and $z + \sigma$ grids. Their results agree well with those obtained in cited studies. The (partly) shaved cell grids can also represent these physical processes well. Their difference to the σ grid simulation is mainly due to the local difference in resolution. The solutions on full cell grids are characterized by grid noise caused by artificial ridges in full cell discretization. Note that employing biharmonic dissipation may help smooth grid noise induced by discontinuous bottom representation with relatively less dissipation effect. But the results in Adcroft et al. (1997) imply that the major part of impact of the nonrobust topography representation could not be eliminated by simply using higher order dissipation.

The partly shaved cell grids are shown to resolve topography related processes much better than full cell grids. But their solutions still contain some small scale noise above artificial ridges, which could exist in regions where the aspect ratio of the grid cell ($\Delta z / \Delta x$) is smaller than the local slope of the topography. FE models can flexibly employ unstructured meshes with varying resolution in the horizontal and/or vertical, so fully shaved cell grids can also be realized for steep slopes. Then the model performance can be further improved. However, realizing such grids in regions of very steep slopes can introduce too small horizontal scales which could lead to numerical difficulties, so this approach usually is only applied when these steep slopes are research interest relevant.

Chapter 4

Stratified topographic waves in a channel

Although reproducing the particular small-slope topographic waves studied by Rhines (1970) requires only solving linearized equations, it is a tough problem for traditional z-level ocean models, as it is sensitive to the way the bottom topography is taken into account. Simulating topographic waves was taken by Pacanowski and Gnanadesikan (1998) to test their partial cell algorithm. Here we use the same setup to demonstrate that the shaved cell algorithm in FEOM performs well in reproducing the dispersion relation of topographic waves propagating in the presence of a gentle slope.

4.1 Background

The linearized hydrostatic Boussinesq equations are given by

$$\frac{\partial u}{\partial t} - fv = -\frac{1}{\rho_0}\frac{\partial p^f}{\partial x} \tag{4.1}$$

$$\frac{\partial v}{\partial t} + fu = -\frac{1}{\rho_0}\frac{\partial p^f}{\partial y} \tag{4.2}$$

$$\frac{\partial p^f}{\partial z} = -\rho g \tag{4.3}$$

$$\frac{\partial \rho}{\partial t} = \frac{\rho_0}{g} w N^2 \tag{4.4}$$

$$\frac{\partial u}{\partial x} + \frac{\partial v}{\partial y} + \frac{\partial w}{\partial z} = 0. \tag{4.5}$$

Here p^f is the total pressure including the surface pressure part, N is the buoyancy frequency. Based on these equations topographic waves in a rotating
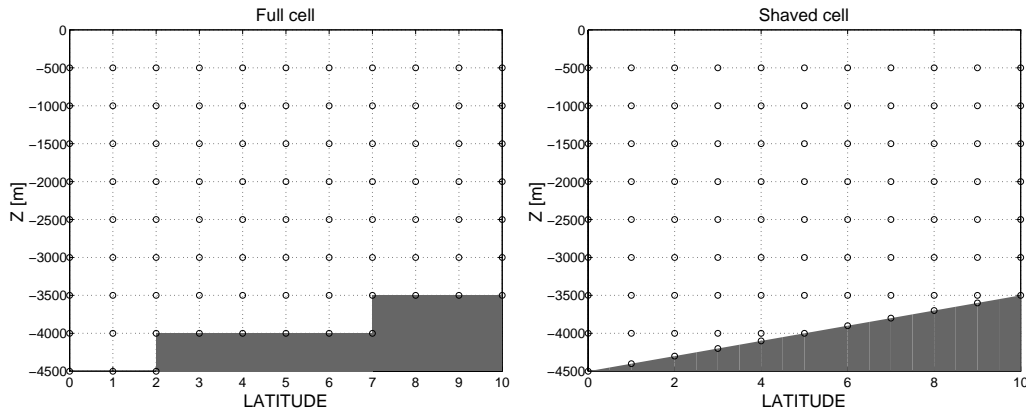
Figure 4.1: A north-south section showing the bottom representation and grid points in the topographic wave simulation. 2D nodes could be unstructured, so the grid shown here is idealized to indicate the difference in bottom representation between these two grids.

stratified fluid in a channel were studied by Rhines (1970). The solution in terms of propagating waves in the limit of low frequency is given by

$$\rho = A \sin(k_x x - \omega t) \sin(k_y y) \sinh(\lambda z) \tag{4.6}$$

where k_x and k_y are zonal and meridional wavenumbers, respectively, x, y, and z are zonal, meridional and depth coordinates, and

$$\lambda = (k_x^2 + k_y^2)^{1/2} \cdot \frac{N}{f}, \tag{4.7}$$

$$\omega = \frac{k_x N^2 \tan \alpha}{f \lambda \tanh(\lambda H)}, \tag{4.8}$$

where f is the Coriolis parameter, $\tan \alpha$ is the topographic slope, and H is the depth of the slope. The phase speed in x-direction is then given by $c = \omega/k_x$. The analytical dispersion relation given above provides the benchmark against which numerical simulations can be easily compared.

4.2   Model setup

The model configuration similar to that used by Pacanowski and Gnanadesikan (1998) is employed in the current work. The zonally reentrant channel of $10°$ lon × $10°$ lat on an f-plane at $45°$N is selected. The channel is 4500 m deep at the south and 3500 m deep at the north with a constant gentle slope of 100 m deg^{-1}. The initial background stratification is linear with depth, with the buoyancy frequency $N = 0.003$ s^{-1}. The linear equation of state is used, and

temperature is the only active tracer. The horizontal viscosity and diffusivity is 10^3 m^2 s^{-1}, the vertical diffusivity is 10^{-4} m^2 s^{-1}, and the vertical viscosity is 2×10^{-3} m^2 s^{-1}. No-slip boundary conditions at rigid walls and free-slip for the bottom are used. The vertical resolution is 500 m equally spaced except in shaved cells, and the horizontal resolution is 1°.

With this resolution there are two artificial topographic ridges in the full cell stepwise discretization (Fig. 4.1). However, this slope can be truly represented using the shaved cell approach. A north-south section showing grid points and model topography is given in Fig. 4.1. In this configuration, the aspect ratio of the grid cell is about five times the slope of the topography, so the fully shaved cell representation can be naturally realized.

In the next section we compare simulations on the full cell and shaved cell grids and confront our results with those of Pacanowski and Gnanadesikan (1998). A noticeable difference between the shaved cell and σ approaches in this experiment is not anticipated, because the local vertical resolution above the topography on the shaved cell grid is sufficient for the current problem.

4.3 Model results

An initial temperature perturbation of the form

$$T = 0.25 \sin(k_x x) \sin(k_y y) \sinh(\lambda z) \tag{4.9}$$

was employed to initialize topographic waves at a wavelength equal to the zonal domain length. So the wavenumbers are set as $k_x = 2\pi/L_x$, and $k_y = \pi/L_x$, where L_x and L_y are zonal and meridional domain length, respectively. The model was integrated for 100 days.
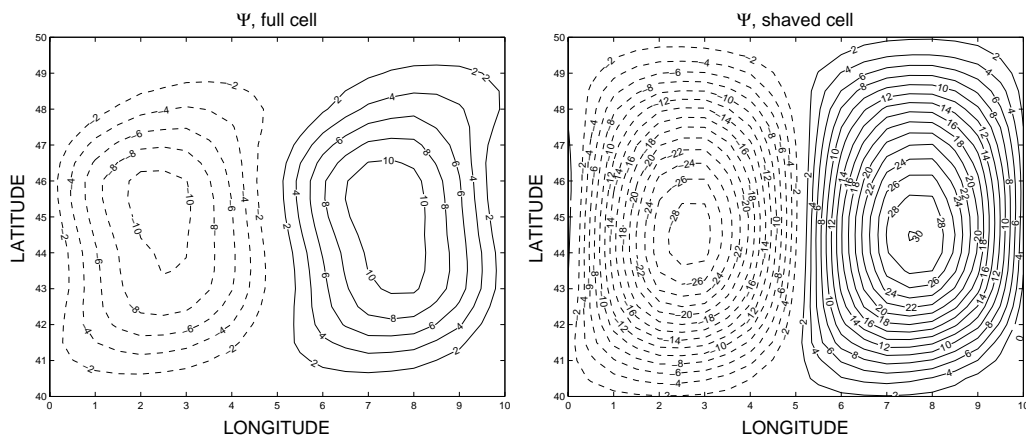

Figure 4.2: Streamfunction [Sv] after 100 days of integration for full cell (left) and shaved cell (right) runs.
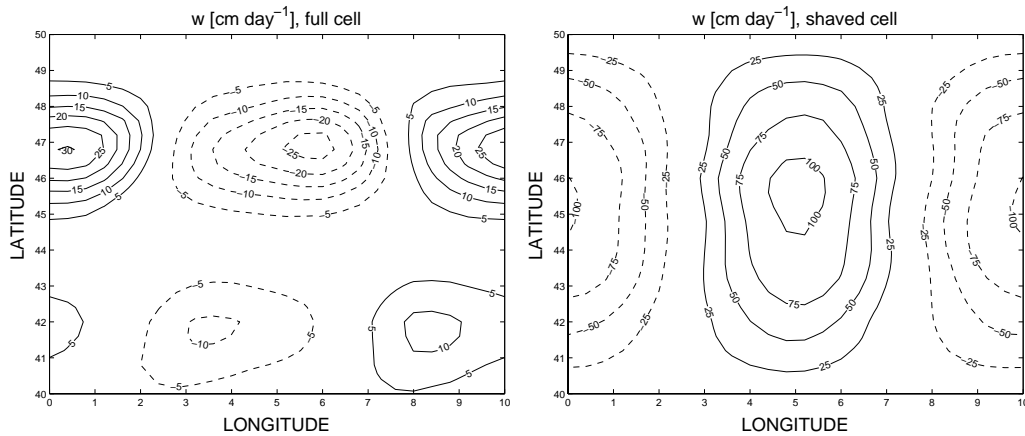
Figure 4.3: Vertical velocity [cm day^{-1}] at the depth of 3500 m after 100 days of integration for full cell (left) and shaved cell (right) runs.

Fig. 4.2 shows the streamfunctions after 100 days integration for the two cases: one with the full cell z-level grid and the other with the shaved cell grid. The shaved cell case produces a wavelike pattern like the initial perturbation. By contrast, the structure of the streamfunction in the full cell case deviates from it and the streamfunction has a reduced amplitude. Vertical velocity fields at the depth of 3500 m are displayed in Fig. 4.3. The full cell solution shows a clear double maximum structure corresponding to the Kelvin waves propagating along the two artificial ridges, similar to the finding of Pacanowski and Gnanadesikan (1998). They argued that it is those small scale features above the artificial ridges in the full cell run that lead to more efficient dissipation and thus smaller streamfunction magnitude.

The vertical structure of the zonal velocity anomaly (time mean from last 50 days removed) shown in Fig. 4.4 indicates the significant baroclinic differences between two cases which is similar to the results by Pacanowski and Gnanadesikan (1998). The vertical topographic trapping is much stronger in the full cell simulation than in the shaved cell case. The shaved cell solution shows a wider meridional scale, whereas the full cell z-level solution shows smaller scales with maximum at the bottom.

The wave propagation indicated by streamfunction anomaly (time mean from last 50 days removed) is shown in Fig. 4.5 in the Hovmöller diagram. The phase speed of the wave in the full cell z-level case is 106 cm s^{-1}, which corresponds to a basin crossing time of about 9 days. The phase speed of the waves in the shaved cell case is about 41 cms^{-1}, and the basin crossing time is 22 days. The theoretical phase speed is 42 cms^{-1} based on the linearized analytical solution. This demonstrates that the simulation with the shaved cell grid can resolve the dispersion relation quite well, while the full cell z-level approach gives results dominated by numerical effects.
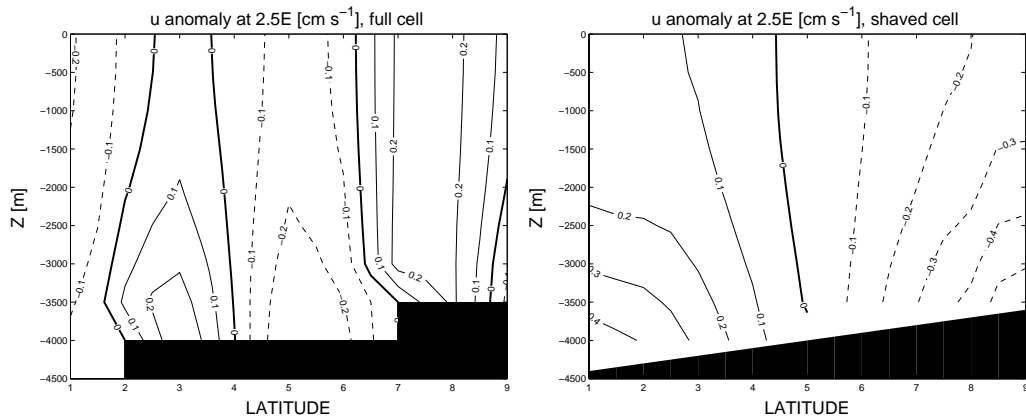
Figure 4.4: Zonal velocity anomaly [cm s^{-1}] in a meridional section after 100 days of integration for full cell (left) and shaved cell (right) runs.
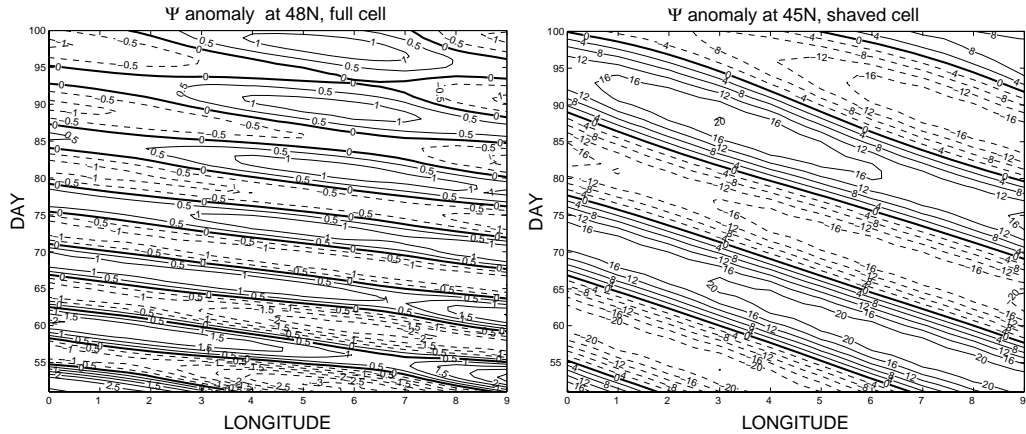

Figure 4.5: Streamfunction anomaly [Sv] as the function of longitude and time for full cell (left) and shaved cell (right) runs. Phase speed of the topographic wave can be estimated from this relationship.

The full dispersion relation of this topographic wave can be constructed from solutions with more wavelengths employed. In the next set of experiments, an initial temperature perturbation with a spectrum containing 15 zonal wavelengths was applied and evolved for 100 days in a zonally reentrant channel of 100° long. The wave frequencies were extracted through Fourier transformation and plotted versus wavenumbers in Fig. 4.6. The shaved cell approach accurately approximates the analytic dispersion relation in regions of both low and high wavenumbers, whereas the result from the full cell z-level simulation deviates far from the analytical solution and the group velocity from the dispersion relation at high wavenumber is opposite to the theoretical value. Another experiment conducted on a σ grid (Fig. 4.6) shows that σ grid simulation can also accurately resolve the topographic wave dispersion relation
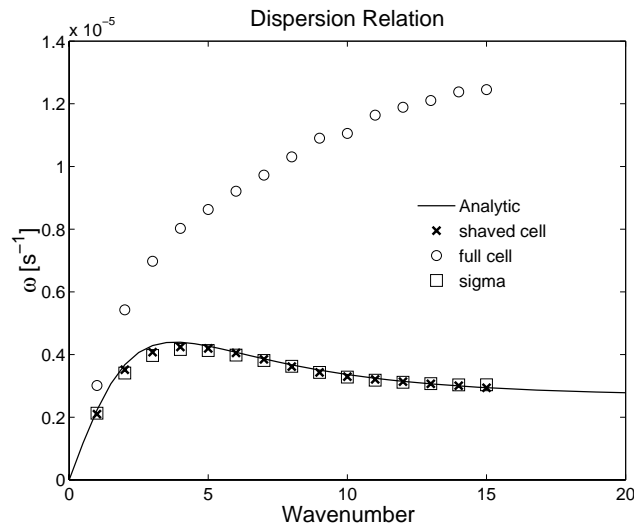
Figure 4.6: Dispersion relation for topographic waves for analytic (solid line), shaved cell (crosses), full cell (open circles), and σ grid (squares).

as expected.

4.4 Summary

Comparison between the performance of shaved cell and full cell grids was undertaken through simulating a topographic wave propagating over a gentle slope. The full cell grid misses the gentle slope of the bottom topography and results in unphysical dispersion relation. The vertical velocity field in this case is characterized with artificial wave modes related to the stepwise topography representation. Simulations with full cell grids are not robust, also because the topography representation does not improve even with increased horizontal resolution, as shown in Fig. 1.4. Both the horizontal and vertical resolution should be increased for full cell grids to perform better. The shaved cell grid accurately represents the topography and well reproduces the analytical dispersion relation.

Chapter 5

Simulating overflows

Overflows play an important role in the world ocean, as they determine the formation of deep waters, such as Mediterranean Overflow Water, North Atlantic Deep Water and Antarctic Bottom Water (Price and Baringer, 1994). Properly representing overflows in ocean general circulation models still faces challenges (Griffies et al., 2000a). The model's vertical discretization and bottom representation is one of the most important issues (Willebrand et al., 2001). Different vertical grids are employed to simulate overflows in an idealized configuration. Their performance is explored.

5.1   Background

Overflows are density driven currents flowing down topography. The overflow dynamics is an important part in the thermohaline circulation of the world ocean because it is the primary source of the deep water in the world ocean's basins. An accurate representation of overflows is of vital importance for OGCM, but it still faces challenges (Griffies et al., 2000a). The model's vertical discretization and bottom representation is one of the most important issues (Willebrand et al., 2001).

There exists increasing evidence that ocean models using z-level grids have difficulties in simulating overflows at relatively coarse resolution mainly because of the step-like representation of the bottom topography (Gerdes, 1993b; Beckmann and Döscher, 1997; Winton et al., 1998). When dense water flows down passing discrete "stairs", excessive vertical mixing generally causes artificial dilution and entrainment (Winton et al., 1998). In order to overcome this difficulty, modifying z-level models by adding a BBL model has been tried to better resolve overflows (Beckmann and Döscher, 1997; Campin and Goosse, 1999; Killworth and Edwards, 1999; Song and Chao, 2000).

Both σ and isopycnal coordinate models can represent flows over topography more accurately, and are able to concentrate vertical resolution in regions of overflow dynamics. For this reason they were extensively used for numerical studies of overflows. The Denmark Strait Overflow (DSO) has been simulated

using σ grid models (Jungclaus et al., 2001; Käse et al., 2003); the Mediterranean outflow has been simulated using both σ grid models (Jungclaus and Mellor, 2000) and isopycnal models (Papadakis et al., 2003). The study of Penduff et al. (2002) suggests that simply smoothing the topography in a z-level model leads to results qualitatively resembling those from a σ grid model. But as to be shown in this work z-level grids have difficulty in representing overflows even on a uniform slope. On the other hand, smoothing topography is indeed a useful practical strategy (also in σ models), but care is generally required, otherwise it can severely deteriorate accuracy.

The DOME project (Dynamics of Overflow Mixing and Entrainment, see `www.rsmas.miami.edu/personal/tamay/DOME/dome.html`) established an idealized model configuration to study the dynamics of overflows. This model configuration is mainly patterned after the overflow in the Denmark Strait. Overflow plume features and accompanying diapycnal mixing, entrainment and BBL dynamics have been studied with this configuration by Ezer and Mellor (2004); Legg et al. (2006); Tseng and Dietrich (2006) using different models and different vertical grids. Although the DOME setup is quite idealized, basic overflow properties derived from model simulations in these studies have been found similar to some observed features of the DSO.

Once more we exploit the ability of FEOM to work with different vertical grids using the same numerical kernel, and explore the influence of vertical discretization, resolution and also partly subgrid approximations on overflow characteristics in the DOME setup. The vertical grid types considered by us are σ, the combination of z and σ which includes several bottom following layers and z-levels above them, the z-level grid and two modification of it, the partly shaved cell and fully shaved cell grids. The latter two allow an accurate bottom representation while using z-levels except the very last layer, and is in effect similar to the shaved and partial cell approaches of structured models. Studying the influence of grid types on overflow simulations with hybrid grid models has the advantage of isolating (as far as possible) the effect of grid types from the model physics and numerics. The work by Ezer and Mellor (2004) using the FD model POM was also intended in this direction.

Our result is that σ and $z+\sigma$ setups provide the smallest plume dilution and plume thickness and largest downslope plume penetration provided horizontal diffusivity is replaced by along-σ diffusivity. Their plume properties start to converge at coarser horizontal resolution than on other grids. Using horizontal diffusivity adds diapycnal mixing and can degrade the σ grid results. Partly shaved cell grids approach the σ grid results at finer horizontal resolution and with larger number of vertical levels.

5.2 Experimental setup

5.2.1 the DOME setup

The model domain includes a basin of 1100 - 1600 km (longitude) by 600 km (latitude) and an attached embayment of 100 km by 200 km (Fig. 5.1a). The depth at the northern boundary of the basin is 600 m, sloping down to the maximum depth of 3600 m to the south with a uniform slope of 1%. The embayment is 600 m deep. The eastern and southern boundaries are closed, and the western boundary is open using the outflow condition with damping applied within a narrow sponge zone. Free-slip and no-flux boundary conditions are applied at closed walls.
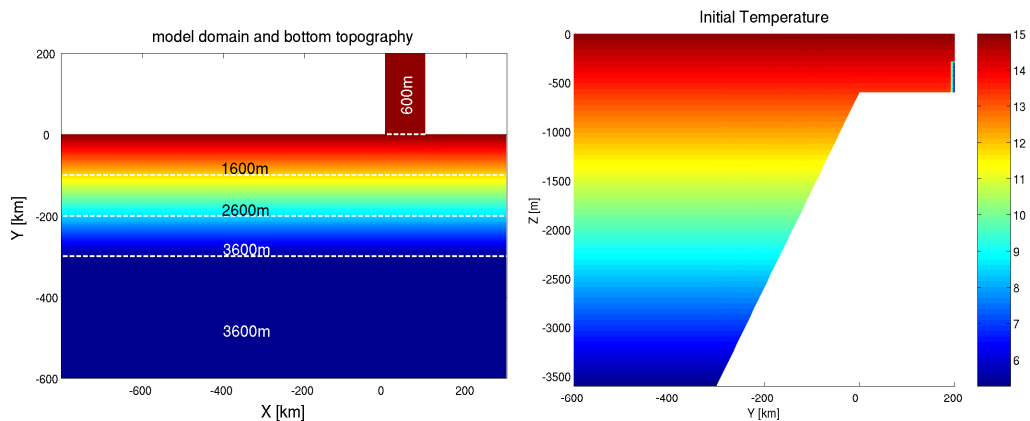

Figure 5.1: (left) Top view of the model domain and bottom topography in the DOME experiments. (right) Side view of a cross-section at $x = 0$ and the initial stratification.

The inflow from the northern open boundary of the embayment is prescribed following Legg et al. (2006) to have 5 Sv of geostrophically balanced dense water, the thickness of which is 300 m at the western wall of the embayment and exponentially decays to zero near the eastern wall. The linear equation of state (only with potential temperature) is used. The initial ambient stratification (Fig. 5.1b) is linear with $N = 2.3 \times 10^{-3}$ s^{-1}, corresponding to a density difference of 2 kg m^{-3} between domain surface and bottom, which is also the density anomaly of the dense inflow. To facilitate the analysis of the overflow, a passive tracer with concentration $c = 1$ was injected into the inflow water. The initial value of c is zero everywhere in the domain.

5.2.2 Numerical experiments

Laplacian dissipation and quadratic bottom drag with $C_d = 0.002$ are employed. An f-plane approximation with the Coriolis parameter $f = 10^{-4}$ s^{-1}

is used. The physical parameters, including the bottom drag coefficient, background stratification, the topographic slope, the Coriolis parameter, and the inflow velocity and width, can influence the results of overflow simulations significantly (Jiang and Garwood, 1996; Legg et al., 2006). Our objective in the current work is to examine the performance of different vertical grids, so we have only chosen a combination of parameters commonly used in the studies of other authors.

Four different resolutions are used for each vertical grid (Table 5.1). On the σ grid, 36 evenly distributed vertical layers are used. On the full cell and partly shaved cell grids, vertical resolutions of 100 m, 50 m, and 25 m are used for different horizontal resolution cases. The fully shaved cell grids are realized by generating surface grid nodes following isobaths and using proper (lower) vertical resolutions. So in fully shaved cell grids the vertical resolutions are 100 m and 50 m for the 10 km and 5 km horizontal resolution cases, respectively, which is coarser than in their full cell and partly shaved cell counterparts. To save CPU time, the resolution varies in space and the resolution referred to above is that in regions where plume dynamics happens.

Experiments using a $z + \sigma$ grid, combining 6 σ layers and z levels above them, show results almost identical to the σ grid simulations. It is simply because the σ layers at the bottom in the $z + \sigma$ grid are able to resolve the overflow plume equally well as a pure σ grid. So the $z + \sigma$ experiments are not separately discussed here, and the properties found in the σ grid runs can be generalized to the $z + \sigma$ simulations. Note, however, that the $z + \sigma$ grid has more advantages in basin scale and climate scale applications because of reduced pressure gradient errors.

In the reference runs (gray parts in Table 5.1), lateral diffusivity of $K_H = 10$ m^2 s^{-1} is used. Lateral viscosity is set to $A_H = 5\,K_H$ in all simulations. To study the sensitivity to lateral diffusivity/viscosity, simulations with $K_H = 100$ m^2 s^{-1} using resolution of 10 km are taken for each grid. The lateral dissipation is oriented in the along-σ direction on the σ grids. Two runs (Si2hor and Si2Hhor) with geopotentially oriented lateral diffusivity/viscosity are done to illustrate the effects of the orientation of sub-grid operators on σ grids.

With currently affordable resolution for climate scale simulations, the processes responsible for entrainment accompanying overflows are not resolved, and hence must be parameterized. In simulations under the framework of DOME setup, Tseng and Dietrich (2006) employed the Richardson-number-dependent scheme (Pacanowski and Philander, 1981) using the z coordinate model DieCAST, whereas Ezer and Mellor (2004) and Ezer (2005) used the turbulence closure scheme of Mellor and Yamada (1982) in the generalized model POM. The isopycnal coordinate models currently tend to employ the empirical gravity current entrainment parameterization (Legg et al., 2006) as described by Hallberg (2000). The simulation employing non-hydrostatic physics (MITgcm) without mixing parameterizations by Legg et al. (2006) shows that the

Table 5.1: Parameters in different runs with the DOME configuration.

Experiments	Horizontal resolution Δx (km)	Vertical resolution Δz (m)	Lateral diffusivity K_H (m^2 s^{-1})	Maximum vertical mixing coefficient A_{v0} (m^2 s^{-1})
Si1	20	36 layers	10	0.05
Si2	10	36 layers	10	0.05
Si3	5	36 layers	10	0.05
Si4	2.5	36 layers	10	0.05
Si2H	10	36 layers	100	0.05
Si2V	10	36 layers	10	0.2
Si2hor	10	36 layers	10 (hor)	0.05
Si2Hhor	10	36 layers	100(hor)	0.05
FC1	20	100	10	0.05
FC2	10	50	10	0.05
FC3	5	25	10	0.05
FC4	2.5	25	10	0.05
FC2H	10	50	100	0.05
FC2V	10	50	10	0.2
PSC1	20	100	10	0.05
PSC2	10	50	10	0.05
PSC3	5	25	10	0.05
PSC4	2.5	25	10	0.05
PSC2H	10	50	100	0.05
PSC2V	10	50	10	0.2
FSC2	10	100	10	0.05
FSC3	5	50	10	0.05
FSC2H	10	50	100	0.05
FSC2V	10	50	10	0.2

Si, σ grid; FC, full cell grid;
PSC, partly shaved cell grid; FSC, fully shaved cell grid;
hor, cases with horizontally (geopotentially) oriented lateral dissipation.

processes responsible for mixing are captured at horizontal resolution of 500 m, but this resolution is still insufficient to fully resolve mixing processes.

In the current work, the modified Richardson-number-dependent scheme (Pacanowski and Philander, 1981) is used. The parameterized vertical viscosity A_v and diffusivity K_v are computed as

$$A_v = \frac{A_{v0}}{(1 + \alpha \mathrm{Ri})^n} + A_{vb}, \qquad (5.1)$$

$$K_v = \frac{A_v}{1 + \alpha \mathrm{Ri}} + K_{vb} \qquad (5.2)$$

where the local gradient Richardson number is

$$\mathrm{Ri} = \frac{N^2}{u_{,z}^2 + v_{,z}^2}. \tag{5.3}$$

The same formulas but with Ri set to zero are applied if stratification becomes unstable. The background values A_{vb} and K_{vb} are set to 2×10^{-5} m^2 s^{-1} throughout the work. Constants $n = 2$ and $\alpha = 10$ are used. A_{v0}, which is the limiting value of A_v and K_v under the neutral and unstable conditions Ri ≤ 0, is the prescribed maximum value of vertical mixing coefficients. In different applications different controlling physical processes might require different values of A_{v0}. Besides the standard value $A_{v0} = 0.05$ m^2 s^{-1} used in reference runs, experiments using $A_{v0} = 0.2$ m^2 s^{-1} at the 10 km resolution are carried out to demonstrate the influence of this parameter. The mixing scheme also works to remove the static instability, so convective adjustment is not employed in this work. Note that convective adjustment could still be required in general applications.

The FCT advection scheme (Löhner et al., 1987) described above in Chapter 2 is employed in the current work, which both prevents the appearance of overshoots and introduces numerical diffusion where needed for stability. Clearly, different implicit diffusion effects are associated with different advection schemes. Studying these effects is beyond the scope of the current work. But it is worth mentioning that the reference runs with small lateral diffusivity provide solutions that do not show significant difference to those with zero explicit lateral diffusion (not shown). These solutions are thus in the regime where numerical diffusion exceeds explicit lateral diffusion.

5.3   Model results

5.3.1   General description

Fig. 5.2 shows snapshots of the tracer concentration c just above the bottom on four different days in σ grid run Si3 at the 5 km resolution. The westward and downslope propagation of the dense bottom plume with large scale eddies can clearly be observed, as expected from previous studies (Jiang and Garwood, 1996; Cenedese et al., 2004; Ezer and Mellor, 2004; Legg et al., 2006). The propagation of the dense plume is accompanied by bottom Ekman flows and development of eddies. The large amplitude eddies have spatial scales of 50 to 100 km, and the Rossby radius of deformation at their locations is about 20 to 50 km, so these eddy structures can be resolved with a 5 km horizontal scale. Most of the tracer dilution occurs to the east of $x = -200$ km. The overflow water reaches the neutral buoyancy level when it penetrates downslope to about $y = -200$ km. The spatial scale of eddies and the distance of the downslope penetration of the dense plume are quite close to those shown in snapshots in figure 5 of Ezer and Mellor (2004).
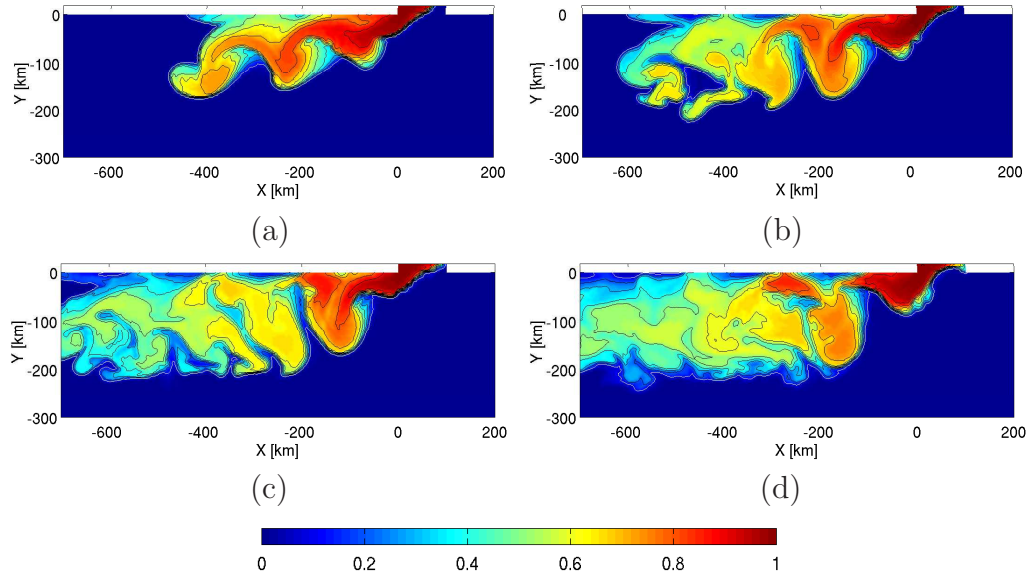
Figure 5.2: Instantaneous bottom tracer concentration in the Si3 run after (a) 10, (b) 15, (c) 20 and (d) 30 days. Contour interval is 0.1.

In the DOME configuration, $0.4 < Fr < 0.6$ and $Ek < 0.1$ almost everywhere in the main part of the overflow (Ezer, 2005), where Fr is the Froude number and Ek is the Ekman number, therefore, the simulated flow is in an eddy regime (Cenedese et al., 2004). Strong cyclonic eddies can be found in all runs. The vertically integrated relative vorticity after 15 days for 5 km resolution runs is shown in Fig. 5.3. A train of cyclonic eddies connected by weaker anticyclones along the path of the dense plume is present, consistent to numerical and laboratory studies (e.g., Jiang and Garwood, 1996; Lane-Serff and Baines, 2000; Käse et al., 2003). One possible mechanism for cyclonic eddy generation is the conservation of potential vorticity (Spall and Price, 1998; Lane-Serff and Baines, 1998, 2000; Etling et al., 2000; Cenedese et al., 2004). When the dense fluid which is coupled with the lighter water colume above it moves downslope, the vortex is stretched. To conserve the potential vorticity, the water colume acquired cyclonic vorticity. Dramatic cyclonic eddies over the path of the DSO along the coast of Greenland have been clearly observed (Bruce, 1995) through satellite measurements.

5.3.2 Comparison between grids

a) Tracer concentration over the bottom

The snapshots of bottom tracer concentration from simulations on different grids are shown in Figs. 5.4 – 5.7. Results on different grids even at the same resolution appear to be very different. In the full cell case, the dense
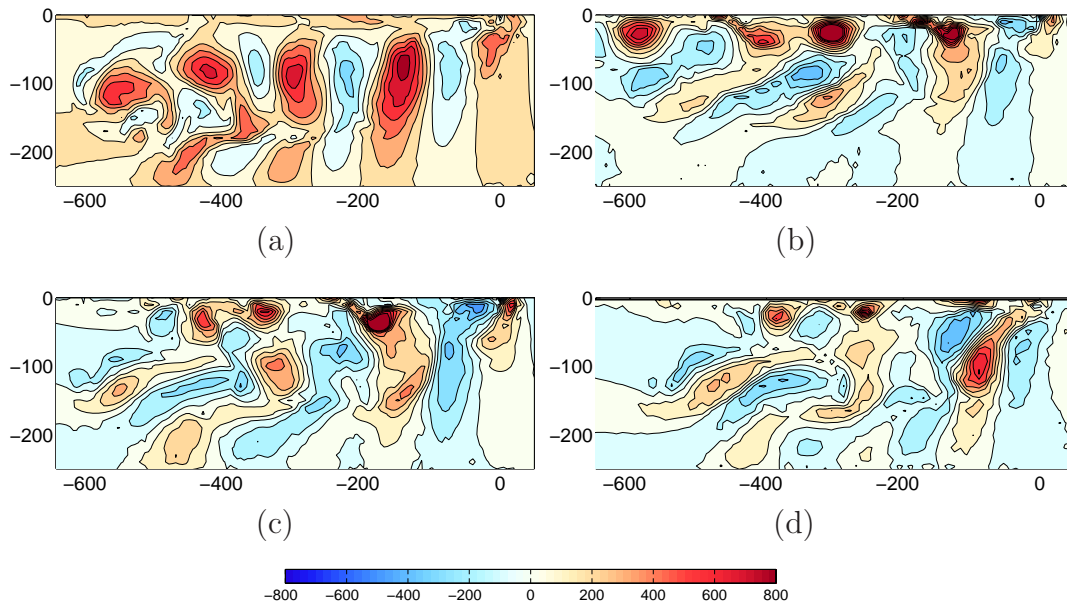
Figure 5.3: Vertically integrated relative vorticity after 15 days for (a) σ, (b) full cell, (c) partly shaved cell, and (d) fully shaved cell grid runs at resolution of 5 km. Notice the difference in the position of cyclonic eddies between the σ and other types of grids.

plume remains closer to the coast than in the σ cases, and the descent of the downslope side front is about 50 to 100 km less than that in the σ runs. The development of large scale eddies on the full cell grids is also confined near to the northern coast compared with the σ grid simulations. These findings are consistent with those of Ezer and Mellor (2004), who have also reported the difficulty of full cell grids in properly simulating overflow processes.

The z-level model (DieCAST, full cell grid) used in the study of Tseng and Dietrich (2006) utilizes a high-order conservative advection scheme, which suppresses numerical instability and allows using very small viscosity/diffusivity. Such numerical ability has advantages in oceanographic applications (e.g., Dietrich et al., 2004), but the behavior of overflow in the DOME setup is not significantly changed in terms of downslope penetration and resolution sensitivity by this numerical property. The simulations of Tseng and Dietrich (2006) show that the downslope penetration distance of the dense plume is limited to about 100 km offshore, similar to the full cell simulations in Ezer and Mellor (2004) and in the current work. However, there are indeed smaller scale structures in simulations by Tseng and Dietrich (2006) than in ours, simply because of the very small diffusivity and viscosity (4 $\mathrm{m^2 s^{-1}}$) they have used.

The downslope propagation process as simulated by models on full cell z-level grids has been explained by Winton et al. (1998) and Ezer and Mellor
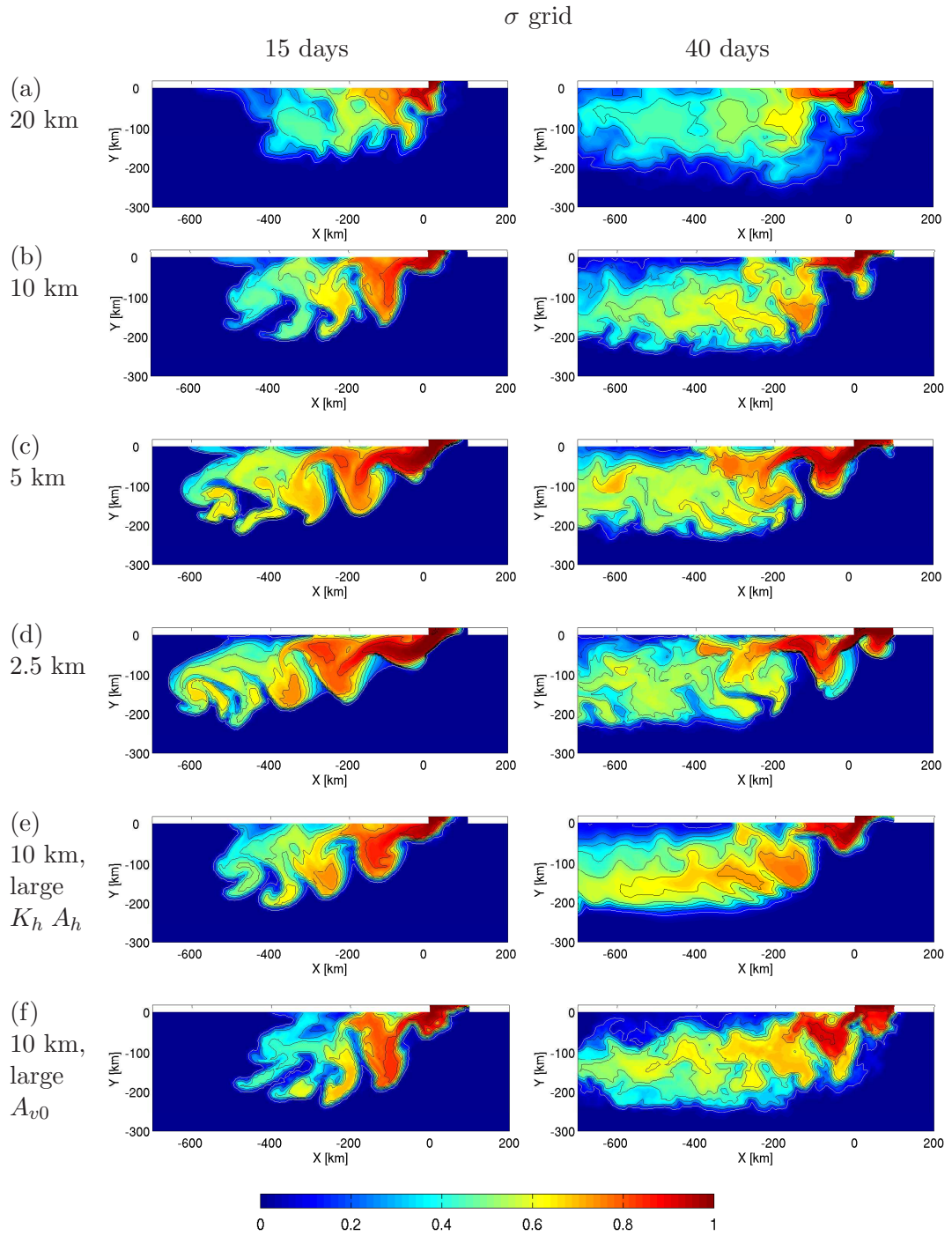
σ grid

15 days   40 days

(a)
20 km

(b)
10 km

(c)
5 km

(d)
2.5 km

(e)
10 km,
large
K_h A_h

(f)
10 km,
large
A_{v0}

Figure 5.4: Instantaneous bottom tracer concentration in the σ grid simulations for runs (a) Si1, (b) Si2, (c) Si3, (d) Si4, (e) Si2H and (f) Si2V. Results after (left) 15 days and (right) 40 days are shown for each run. There is no strong sensitivity to resolution beginning from 5 km resolution (c) , and even the difference between the 10 km (b) and 5 km (c) results with respect to large scale eddies and plume downslope penetration is not very significant.
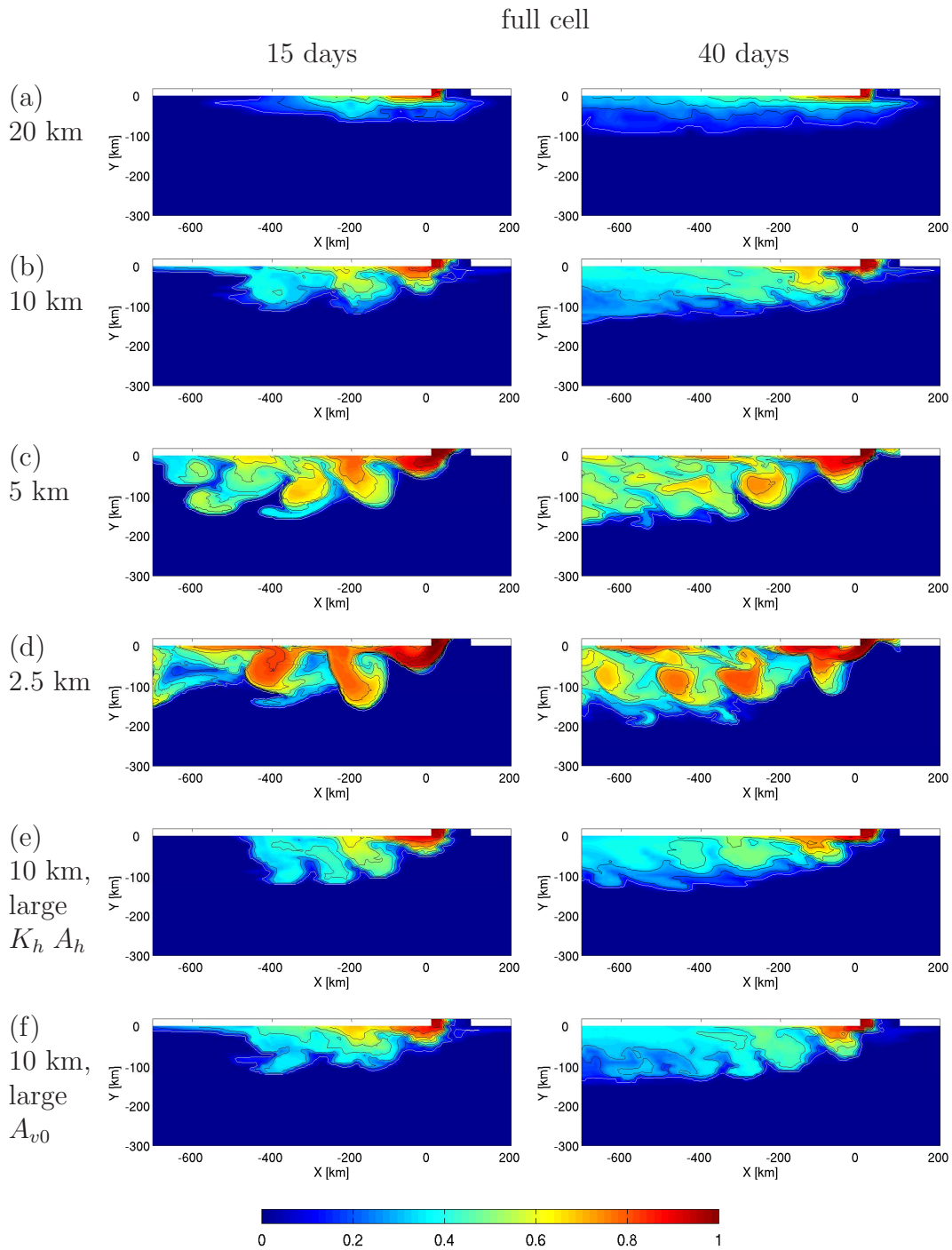
Figure 5.5: As in Fig. 5.4 but for the full cell grid simulations: (a) FC1, (b) FC2, (c) FC3, (d) FC4, (e) FC2H and (f) FC2V. Note the strong sensitivity to the horizontal resolution in these full cell cases. The downslope propagation is limited.
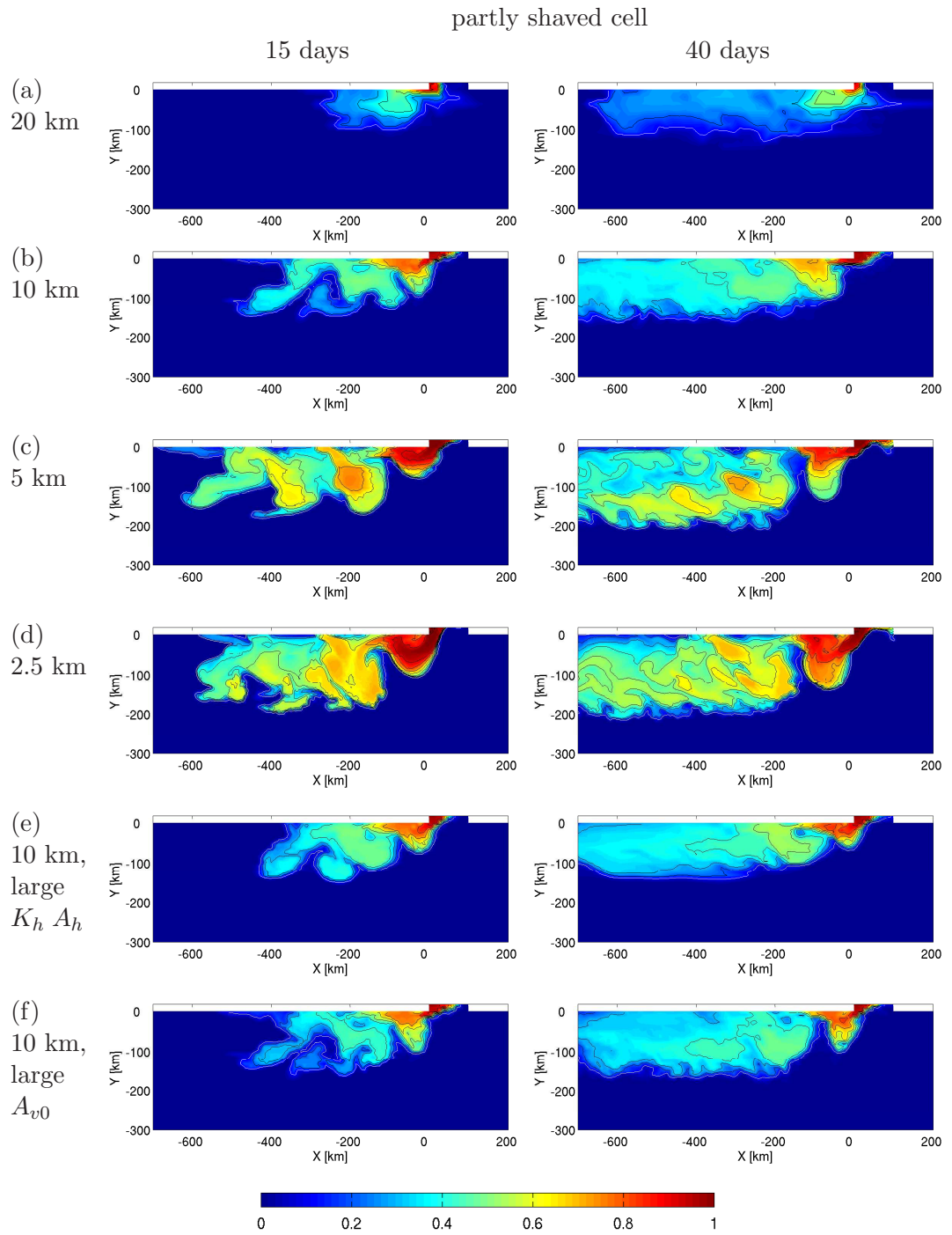
partly shaved cell

Figure 5.6: As in Fig. 5.4 but for the partly shaved cell grid simulations: (a) PSC1, (b) PSC2, (c) PSC3, (d) PSC4, (e) PSC2H and (f) PSC2V. With the increase in resolution, the skill of partly shaved grids is improving and the characteristics of the simulated plume start to approach those on σ grids.
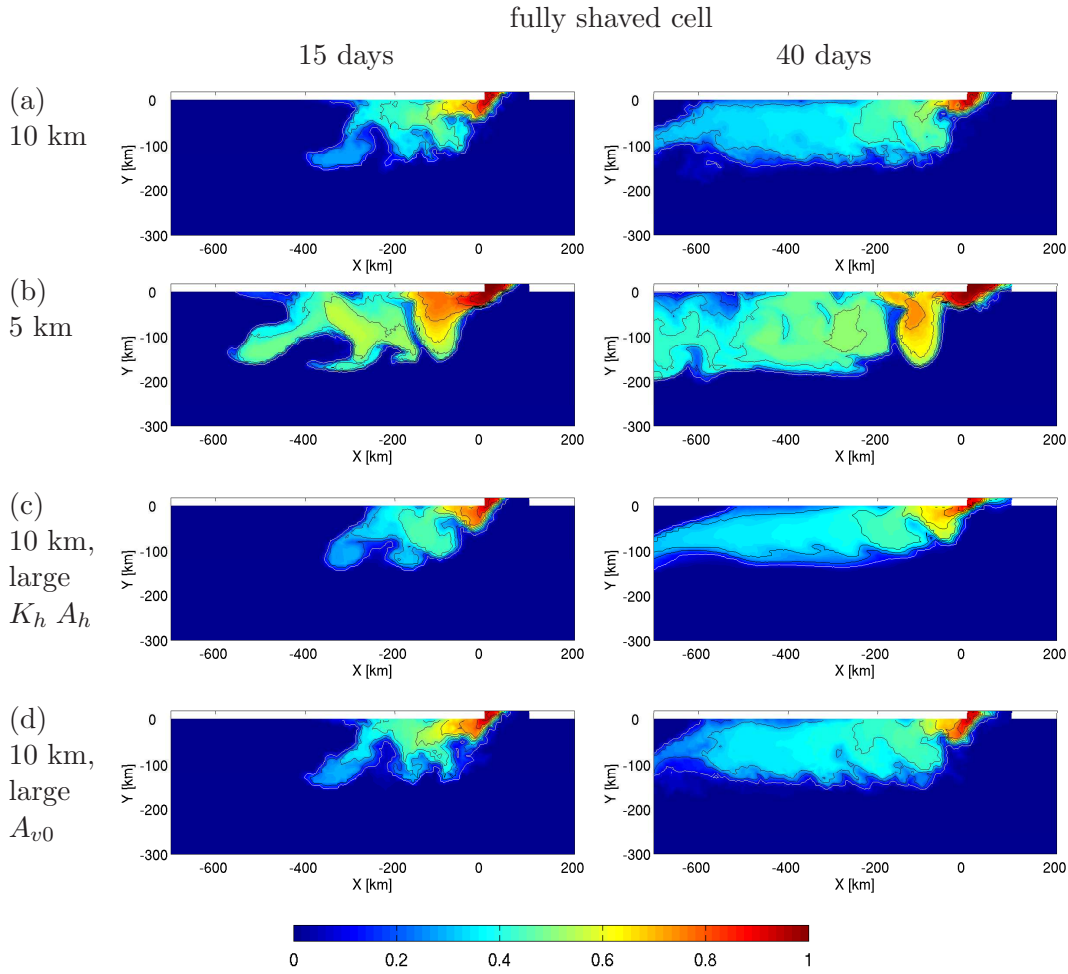
fully shaved cell

Figure 5.7: As in Fig. 5.4 but for the fully shaved cell grid simulations: (a) FSC2, (b) FSC3, (c) FSC2H and (d) FSC2V. Although the fully shaved cells provide better bottom approximation than partly shaved cells they are lacking vertical resolution for the prescribed horizontal resolution. Hence, they lead to stronger dilution of the plume. This comparison emphasizes that both bottom representation and vertical resolution in the bottom vicinity are important.

(2004). Passing the plume over the step-like topography in the full cell grid involves two steps. First, advection and diffusion mix the plume with the adjacent water mass in the horizontal direction; then the vertical mixing scheme (Richardson-number-dependent scheme in the current work) creates large vertical mixing due to an unstable stratification (Fig. 5.8b). This situation is different from the σ grid case (Fig. 5.8a), in which along sigma/slope advection plays the dominant role. Winton et al. (1998) indicated that unless both vertical and horizontal resolution satisfy the criteria

$$\Delta z < h \text{ and } \Delta x < h/\tan\alpha, \tag{5.4}$$

where h is the thickness of the overflow and α is the topographic slope angle, full cell z-level models are unable to transport dense overflows down the slope without excessive entrainment. Although the requirements on both the horizontal and vertical resolutions are satisfied in our full cell simulations, they still have difficulty in reproducing downslope propagation. At coarse resolution the dense plumes are clearly more diluted on the full cell grids than on the σ grids. With the increase in resolution, eddies associated with high tracer concentration can be seen in the bottom tracer snapshots on full cell grids. However, the spatial and temporal mean of the final plume density shows that the dense plumes as a whole are still more diluted on the full cell grids than on the σ grids (see details in section 5.3.5).

The simulations using the partly shaved cell grid (Fig. 5.6) show a better resolved plume than on the full cell grid in terms of the downslope penetration. With the shaved elements introduced, the bottom topography is better approximated and the stairs, over which the dense fluid passes, are not so steep as in their full cell counterparts. A larger downslope descent of the plumes can be observed on the partly shaved cell grid than on the full cell grid. At the 2.5 km resolution the bottom tracer concentration on the partly shaved cell grid is quite close to the σ result at the quasisteady stage (after 40 days). The tendency of approaching the σ results with the increase in resolution can be observed on the partly shaved cell grids, but is not clearly observable on the full cell grids. The grid scale errors due to artificial ridges are also expected to be smaller in the partly shaved cell simulations (see Chapter 3). But the remaining artificial stairs can still cause spurious mixing.

The fully shaved cell simulations at horizonal resolutions of 10 km and 5 km (Fig. 5.7) show plume structures similar to their partly shaved cell counterparts in terms of eddy characteristics and plume propagation, but the plume is more diluted in these cases. This is simply due to a coarser vertical resolution adopted on such grids in order to match the horizontal resolution. Because of lower vertical resolution, the fully shaved cell grid do not further improve overflow representation compared with the partly shaved cell grids despite the fact that they do not contain artificial ridges and allow downslope advection (Fig. 5.8d). The series of experiments with fully shaved cell grids clearly demonstrate the role of vertical resolution. The sensitivity to resolution is addressed in a later section.

b) Plume thickness

Fig. 5.9 to Fig. 5.12 show the cross section of the passive tracer at $x = -100$ km after 40 days. The full cell grid simulations have the dense plume remaining the closest to the coast. On the σ grid, the plume thickness is the thinnest, the front can penetrate downslope 150 to 200 km in this cross section. For each resolution the partly and fully shaved cell grid simulations show thicker plumes than the σ grid results. But their results agree better with
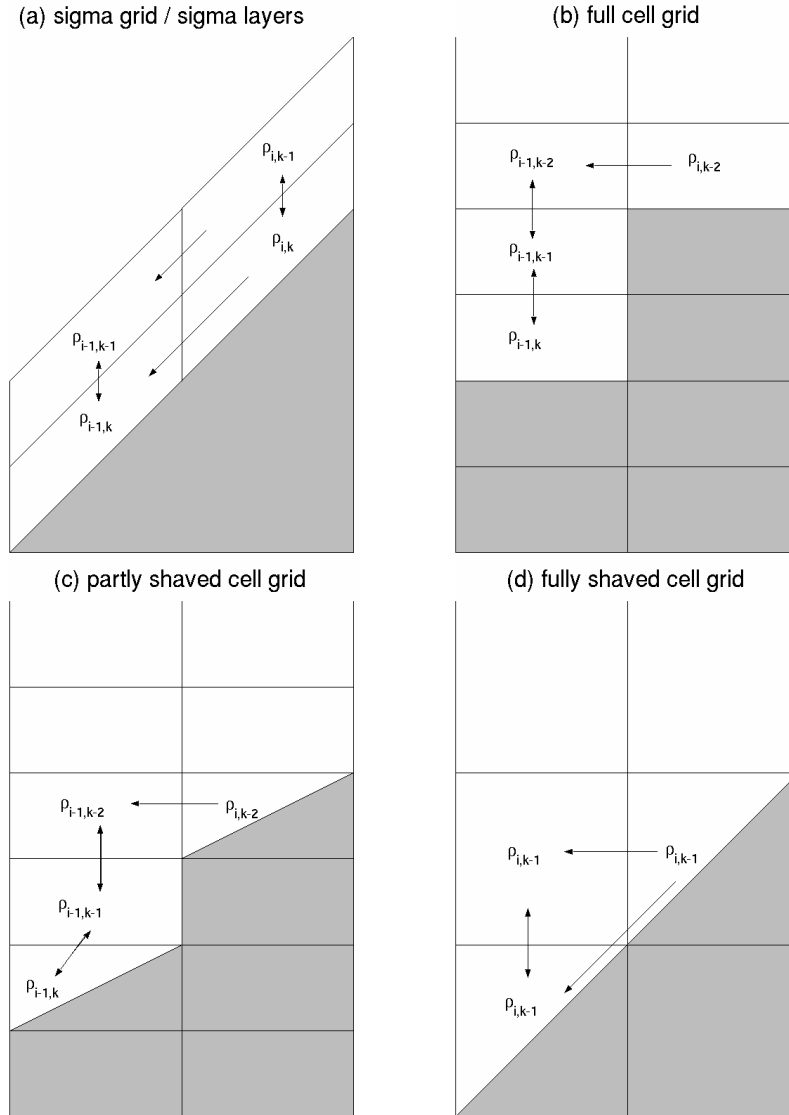
Figure 5.8: Schematic diagram of the near bottom mixing processes of a dense plume for (a) σ or $z + \sigma$ grid, (b) full cell grid, (c) partly shaved cell grid, and (d) fully shaved cell grid. As explained by Ezer and Mellor (2004), the along slop advection in the σ grid is large so that the density $\rho_{i,k} \approx \rho_{i-1,k} > \rho_{i-1,k-1}$, while vertical mixing in the full cell grid is large so that $\rho_{i,k-2} > \rho_{i-1,k-2} \approx \rho_{i-1,k-1} \approx \rho_{i-1,k}$. The processes in the partly shaved cell grid are similar to those in the full cell grid, whereas the topography in the partly shaved cell grid is better approximated than in the full cell grid. The fully shaved cell grid, in which $\rho_{i,k-1} \approx \rho_{i-1,k} \approx \rho_{i-1,k-1}$, can accurately represent the slope, and the along slope advection is large. But its vertical resolution is coarser than in the partly shaved cell grid when the same horizontal resolution is used.

Figure 5.9: Cross section of tracer concentration at 100 km downstream of the embayment after 40 days for the σ runs: (a) Si1, (b) Si2, (c) Si3, (d) Si4, (e) Si2H and (f) Si2V. Contour interval is 0.1.

Figure 5.10: As in Fig. 5.9 but for the full cell runs: (a) FC1, (b) FC2, (c) FC3, (d) FC4, (e) FC2H and (f) FC2V.

Figure 5.11: As in Fig. 5.9 but for the partly shaved cell grid runs: (a) PSC1, (b) PSC2, (c) PSC3, (d) PSC4, (e) PSC2H and (f) PSC2V.

Figure 5.12: As in Fig. 5.9 but for the fully shaved cell grid runs: (a) FSC2, (b) FSC3, (c) FSC2H and (d) FSC2V.

the σ results with respect to the downslope propagation distance compared with the full cell simulations.

The thickness of the dense plume (defined by tracer concentration $c > 0.1$) averaged over the domain after 40 days is shown in Fig. 5.13. At each resolution the σ grid simulation always has the smallest plume thickness. The average plume thickness on the σ grid at the 10 km resolution is about 220 m, close to the model result in Ezer and Mellor (2004). At fine resolution (2.5 km) the average plume thickness on the full cell and partly shaved cell grids is similar, but at coarse resolution the average plume thickness on the partly shaved cell grid is even thicker than that on the full cell grid. The explanation is due here. The plume is more confined to the coast (Fig. 5.14) and propagates faster along the slope (cf. 5.4-5.7) on the full cell grid. Very large diapycnal mixing takes place mainly within a relatively narrow range from the coast, resulting in large plume thickness there. But only very limited tracers are able to penetrate further downslope, associated with relatively thin plumes in this region. Because of this part of contribution, spatially averaged plume thickness on the full cell grid is smaller than that on the partly shaved cell grid. This observation can be understood as one of the manifestations of the full cell grid's difficulty in producing sufficient downslope propagation.

c) Meridional tracer distribution

Quantifying the average water mass distribution is a useful perspective to compare the performance of different grids. The water mass distribution can be characterized by the zonally averaged vertically integrated tracer concentration (Ezer and Mellor, 2004),

$$C(y,t) = \sum_x \sum_z c(x,y,z,t)\Delta x \Delta z \bigg/ \sum_x \Delta x \;, \qquad (5.5)$$

which has units of meter and is proportional to the average thickness of the plume at each downslope distance. This quantity from results averaged over one week after 40 days for different runs is shown in Fig. 5.14.

In the σ-grid simulations, the maximum is always found large distance from the coast for all resolutions used, with the maximum thickness located between 170 km to 200 km offshore. This location is close to that of the isopycnal model (HIM) result (see Legg et al., 2006), but about 100 km farther away from the coast than the σ simulation with POM (Ezer, 2005). Difference in model numerics details, including mixing parameterization, could contribute to such a variance. Finding appropriate parameterizations for diapycnal mixing is still an area of ongoing research (Hallberg, 2000; Papadakis et al., 2003; Ezer, 2005; Legg et al., 2006), and the difference mentioned above emphasizes the need for further studies.

In the full cell simulations the maximum thickness of the dense plume is about 25 km offshore independent on resolution (Fig. 5.14), although an
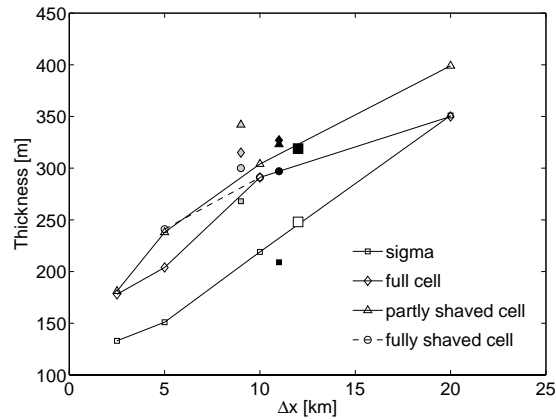
Figure 5.13: Plume thickness averaged over the domain as the function of horizontal resolution for the reference runs listed in Table (5.1). The results from runs with lateral diffusivity of 100 $m^2\,s^{-1}$ (black) and vertical mixing coefficient limiter value of 0.2 $m^2\,s^{-1}$ (gray) at horizontal resolution of 10 km are shown with separated small markers; the σ runs with geopotentially oriented dissipation are shown with big squares (white for case Si2hor and black for case Si2Hhor). To avoid overlap they are plotted at slightly shifted Δx locations. The plume thickness decreases with an increase in resolution. The simulated dense plume on σ grids is thinner than on other grids. The plume on shaved cell grids is thicker than on the full cell grids, see explanation in the text (section 5.3.2). Increasing the along-σ mixing on the sigma grid leads to a thinner plume, whereas an increase in along-geopotential diffusivity results in an increase in plume thickness.

increase in resolution can indeed lead to increased downslope distribution as also indicated in Fig. 5.10. This location is very similar to that found in the z-level grid simulation with POM (Ezer, 2005). The maximum location in the partly and fully shaved cell grid runs is between the maximum locations of σ and full cell grids at all different resolutions. The sensitivity to resolution is addressed in the next section.

5.3.3   Sensitivity to resolution

With an increase in resolution, the plume structure is better resolved on all different grids in terms of resolved large amplitude eddies, plume dilution (Fig. 5.4 to Fig. 5.7), and average plume thickness (Fig. 5.13). But the σ grid shows less resolution dependence than others.
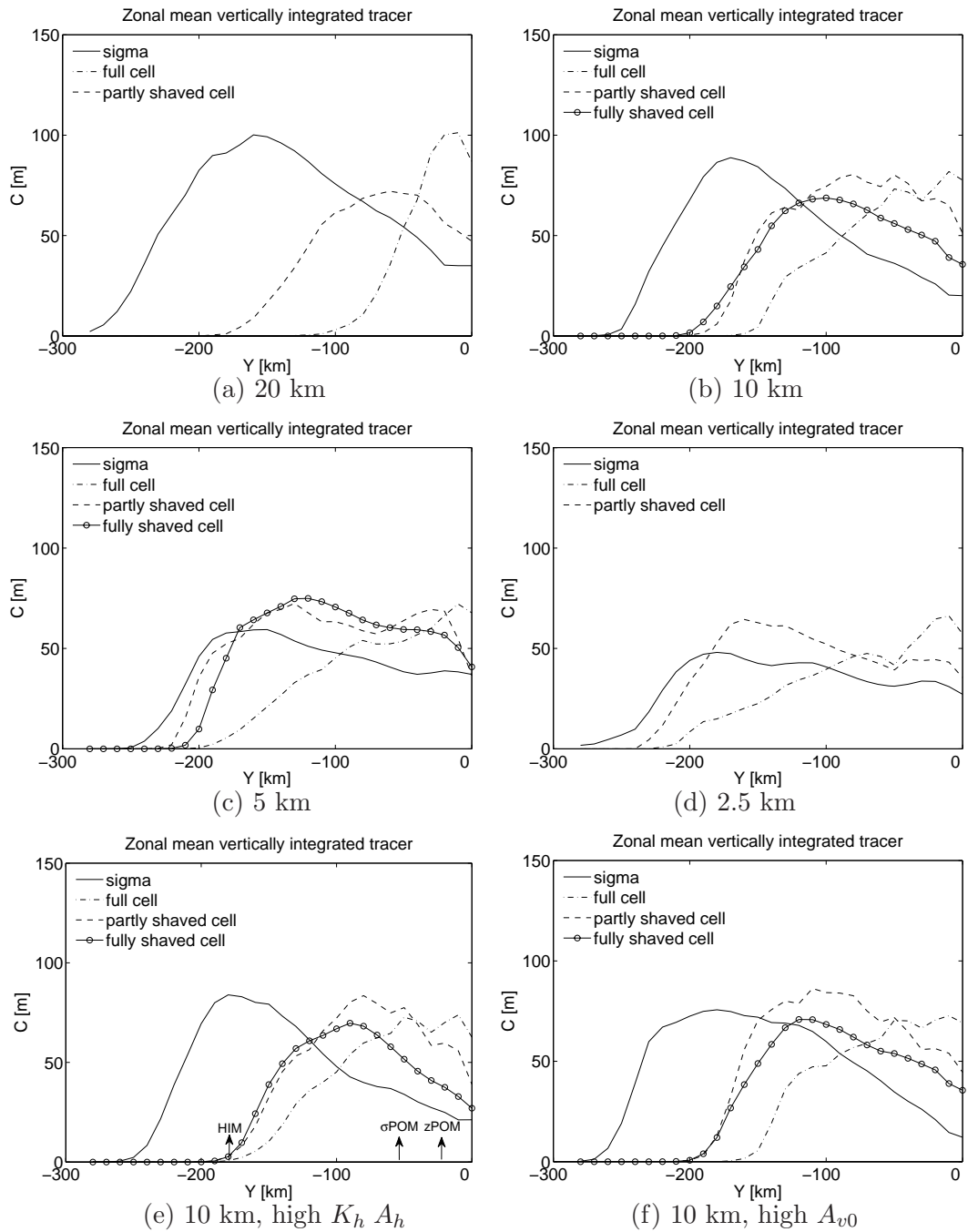
Figure 5.14: Zonal mean and vertically integrated tracer as the function of downslope distance, for reference runs with horizontal resolution (a) 20 km, (b) 10 km, (c) 5 km, (d) 2.5 km, and for (e) runs with lateral diffusivity of 100 m^2 s^{-1} and (f) runs with vertical mixing coefficient limiter value of 0.2 m^2 s^{-1}. Also indicated by arrows in (e) are the locations of the maxima for the POM σ case (σ-POM), POM z-level case (z-POM), and HIM case (HIM) taken from Ezer (2005). Note the convergence of results on partly shaved cell grids to those on σ grids with the increase in resolution. The plume is more confined to the coast on the full cell grid than on other grids in all cases.

a) Sigma grids

In the σ run with horizontal resolution of 20 km, the dense plume is poorly resolved, but it still resembles a coarse-grained version of the plume structure from the run with resolution of 10 km. The maximum location of the zonal mean vertically integrated tracer at resolution of 20 km (Fig. 5.14a) is also quite close to the maximum location in other higher resolution runs.

The simulation on the σ grid with 10 km resolution can marginally resolve the plume in terms of eddies and subplumes. Resolution of 5 and 2.5 km should be sufficient to fully resolve the large scale eddies and Rossby deformation radius. It can be seen that the plume structures in the σ grid runs with resolution of 5 km and 2.5 km are quite close to each other (Fig. 5.4c,d). The average plume thickness (Fig. 5.13) also shows that the trend of the decrease in plume thickness with the increase in horizontal resolution is reduced at resolution finer than $\Delta x = 5$ km. The zonal mean and vertically integrated tracer (Fig. 5.14) demonstrates the similar trend for the σ grid simulations. Indeed, the reduction in the magnitude of the integrated tracer occurs mostly between 10 km and 5 km, and is not so significant between 5 km and 2.5 km resolution.

The difference between σ grids and z-level grids can be attributed to not only the different downslope propagation processes on different grids as indicated in Fig. 5.8, but also to the difference in local vertical resolution. On the σ grid, 36 active layers are used, which correspond to a vertical resolution of 100 m at the southern domain bottom but only 17 m near to the northern coast. The ability to have locally refined vertical resolution is also one of the advantages of the σ grid. With this vertical resolution the BBL dynamics can be marginally resolved as shown later in this section.

b) Full cell grids

The plume structures in the full cell grids (Fig. 5.5) show that full cell grids have more demanding resolution requirement. At both the 10 and 20 km horizontal scales, the plume is very poorly resolved and remains near to the coast, and eddies are almost absent. With the resolution increased to 5 km and 2.5 km, large scale eddies start to appea. Although with an increase in resolution the downslope expansion is increased and plume thickness is reduced (Fig. 5.10 and Fig. 5.13), the location of maximum tracer distribution (Fig. 5.14) is always maintained near to the coast and much less tracer is distributed at the downslope side of the plume than on the σ grids. Comparison between σ grid and full cell z-level grid in Ezer (2005) also indicated that the plume in the full cell run stays closer to the coast and is more diluted than on σ grids even at the resolution of 2.5 km.

Higher requirement for resolution and much more sensitivity to resolution in the full cell grid is a general finding in existing relevant studies (Ezer and Mellor, 2004; Ezer, 2005). Bearing in mind the limited computational resources

currently affordable, high-resolution full cell grid is not adequate for simulating dense water overflows in oceanographic applications, even in basin scale modeling.

c) Partly shaved cell grids

The partly shaved cell grid shows clearly improved performance compared with the full cell grid, since its results converge to the σ results much faster than those on the full cell grid (Fig. 5.14). At 10 km resolution the maximum location of zonal mean vertically integrated tracer on the partly shaved cell grid is less than 100 km offshore with a large amount of dense water remaining near to the coast. With an increase in resolution, the maximum location moves downslope, to about 170 km offshore at horizontal resolution of 2.5 km, and the total shape of distribution tend to resemble the σ grid result. In the partly shaved cell simulations with horizontal resolution of 2.5 km, the bottom tracer concentration at the quasisteady phase after 40 days (Fig. 5.6d) is similar to the σ-grid result, and the downslope penetration distance in the cross section at $x = -100$ km (Fig. 5.11d) is also quite close to that in the σ grid simulation.

d) Fully shaved cell grids

The tracer distribution on the fully shaved cell grids (Fig. 5.14) resembles mostly the partly shaved cell results. But the passive tracer in the fully shaved cell grid with horizontal resolution 5 km and vertical resolution 50 m (Fig. 5.7b) is more diluted than the partly shaved cell result with the same horizontal resolution but with vertical resolution of 25 m (Fig. 5.6c), which implies that vertical resolution finer than 50 m is required to well resolve the BBL dynamics in this model setup.

e) Vertical profiles of tracer concentration

The vertical profiles of tracer concentration taken at locations close to (x, y)=(-100, -40 km) after 40 days are shown in Fig. 5.15 for different runs. In all reference runs, the σ grids resolve the BBL the best. The mixing layer thickness is between 50-100 m in previous model studies (Ezer and Mellor, 2004), close to the σ grid results in the current work. The BBL can be marginally resolved by reference runs with the σ grid, owing to both its fine vertical resolution above the topography and accurate bottom flow representation. The only partly shaved cell run in which the mixing layer thickness almost approaches that of the σ grid simulation is the PSC4 case (Fig. 5.15d), in which the vertical resolution of 25 m and horizontal resolution of 2.5 km are used. Due to unstructured surface meshes used, the locations where these profiles are taken do not exactly coincide at different resolution. But the trend for the mixing layer thickness simulated on z-level grids to converge to the σ grid results with the increase in resolution can still be observed. Especially, comparing
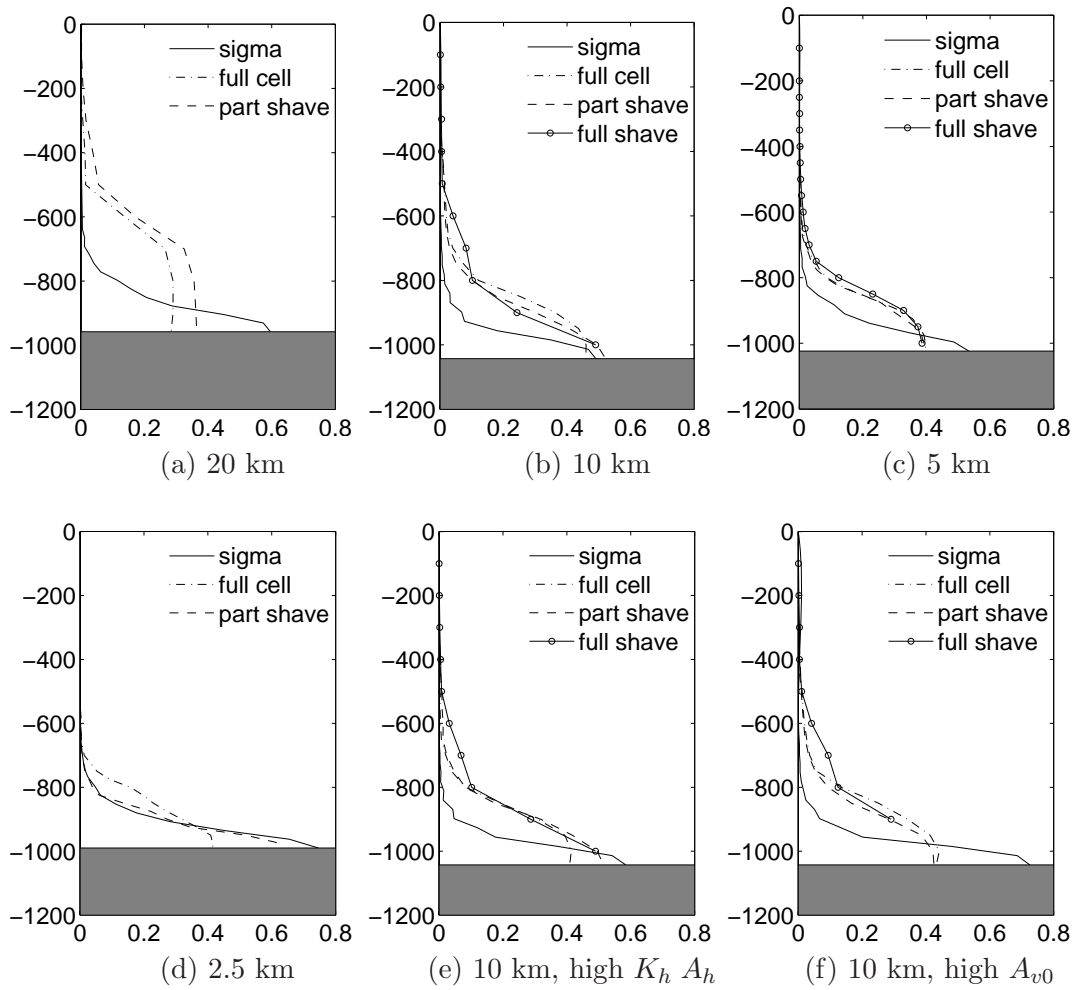
Figure 5.15: Example of vertical profiles of tracer concentration after 40 days: for reference runs with horizontal resolution (a) 20 km, (b) 10 km, (c) 5 km, (d) 2.5 km, and for (e) runs with lateral diffusivity of 100 $m^2\,s^{-1}$ and (f) runs with vertical mixing coefficient limiter value of 0.2 $m^2\,s^{-1}$. The x and y coordinates refer to tracer concentration and depth [m], respectively. The profiles are taken at surface grid nodes which are the closest to the location $(x, y) = (-100\ \text{km}, -40\ \text{km})$. Due to irregular surface nodes used, the locations are not exactly identical at different resolution.

the resolved bottom mixing layer between the cases PSC3 and PSC4, in which the same vertical resolution is employed, clearly demonstrates that the z-level grids need higher horizontal resolution to be able to resolve BBL dynamics than required by the σ grids.

5.3.4   Sensitivity to subgrid scale mixing

a) Sensitivity to the lateral mixing

The sensitivity to lateral dissipation is studied through a series of experiments with higher diffusivity (100 m^2 s^{-1}) using different grids at horizontal resolution of 10 km. The influence of lateral dissipation is clearly illustrated in the snapshots of bottom tracer concentration. With an increase in lateral dissipation, the plume fronts are more diffuse and show less fine-scale features at all grids, simply due to increased damping effects. The tracer concentration in the cross sections at $x = -100$ km indicates reduced downslope penetration, consistent to suppressed frontal instability with increased dissipation.

Except for these common features observed with all grids, there exist also more subtle differences. On the σ grid (Fig. 5.4), the bottom tracer concentration in the high dissipation run (Si2H) is higher than in the low dissipation run (Si2). Fig. 5.13 shows that the plume thickness is decreased in the high dissipation σ run, consistent to the findings by Ezer and Mellor (2004). These features indicate that the dense water is less diluted with an increase in lateral mixing coefficients. This can be attributed to the decrease in parameterized vertical mixing when eddy activity is suppressed by the larger lateral viscosity. On the contrary, the high dissipation runs on other grids show an increase in plume thickness (Fig. 5.13).

b) Sensitivity to the orientation of lateral dissipation

The increase in plume thickness with an increase in horizontal dissipation in the full cell and partly shaved cell grids could be partly attributed to the fact that the larger horizontal diffusion can lead to more excessive vertical mixing over artificial stairs (Ezer and Mellor, 2004). But the increase in mean plume thickness in the fully shaved cell grid suggests another reason for increasing plume thickness. The lateral dissipation is applied in the horizontal direction in all runs except in the σ runs presented so far. A horizontal diffusion can be decomposed to a component along the slope and a component perpendicular to the slope, the latter of which contributes to diapycnal mixing. This can be another reason for the increased plume thickness with an increase in horizontal dissipation on the z-level grids.

To illustrate this point another two σ grid runs (Si2hor and Si2Hhor) were taken, in which geopotentially oriented diffusivity are used. The snapshots for bottom tracer concentration for these two cases are shown in Fig. 5.16. In the case of low horizontal diffusivity (Si2hor), the plume features are similar to the reference run (Si2), in which the dissipation is along-σ (Fig. 5.4b). When the horizontal dissipation is increased (Si2Hhor), not only are the large scale eddies clearly smoothed and suppressed, but also the plume is more diluted than in the low dissipation case (Si2hor). Also opposite to the along-σ diffusion case, the mean plume thickness using horizontally oriented diffusion is

increased with an increase in diffusivity (Fig. 5.17). The zonal mean vertically integrated tracer distribution (Fig. 5.17c) indicated that the value of lateral dissipation has much stronger influence on the overflow simulations when it is oriented in the horizontal direction, which could create dominant diapycnal mixing overwhelming other applied diapycnal mixing parameterizations in the model.
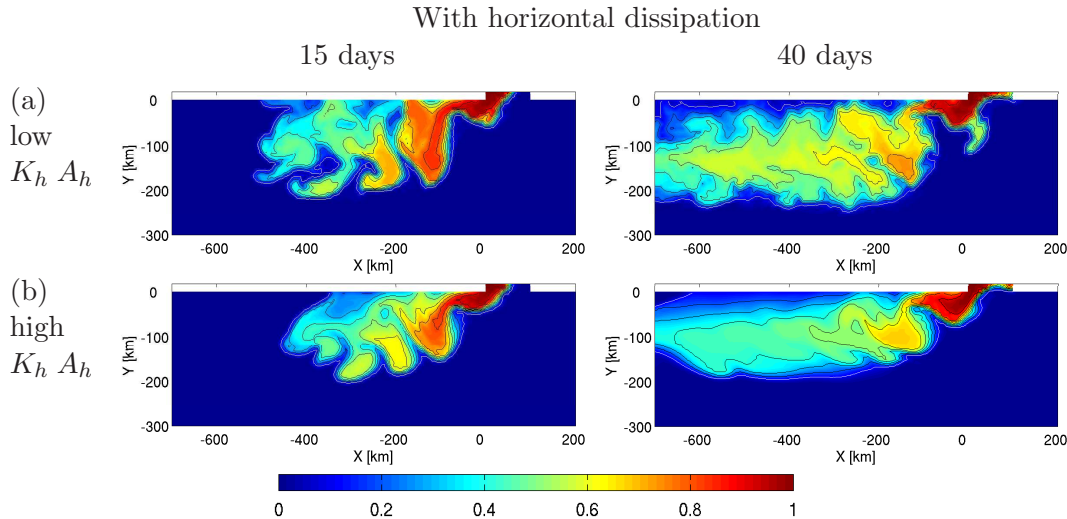

Figure 5.16: Instantaneous bottom tracer concentration on the σ grid for runs with lateral dissipation oriented in the horizontal: (a) Si2hor, (b) Si2Hhor. Results after 15 days (left) and 40 days (right) are shown for each run. Increasing along-geopotential diffusivity not only supresses eddies, but also leads to more dilution.

The influence of the orientation of the lateral diffusion in σ coordinate models has been discussed since a long time (e.g., Beckmann and Haidvogel, 1997). In traditional σ coordinate models the natural orientation of the lateral diffusive/viscous operators is along σ surfaces. An along-σ subgrid mixing can be decomposed to horizontal and vertical components. Beckmann and Haidvogel (1997) suggested to use geopotentially oriented mixing to avoid the smoothing effect in the vertical direction when the vertically propagating internal waves are important. However, along-σ diffusion is commonly used in the simulation of density driven overflows in FD σ coordinate models (e.g., Ezer and Mellor, 2004). The intrinsic properties of density driven overflows (bearing in mind that the isopycnal direction is mostly along the bottom topography slope) support, also can benefit from, the usage of along-σ diffusion.

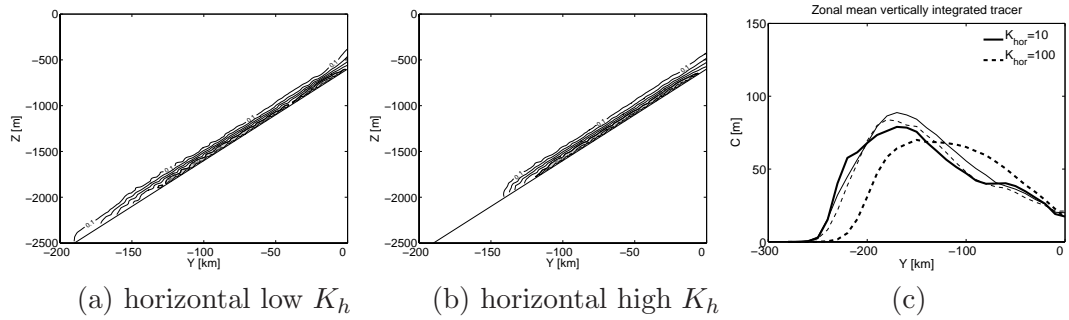(a) horizontal low K_h (b) horizontal high K_h (c)

Figure 5.17: Cross section of tracer concentration at 100 km downstream of the embayment after 40 days for runs with lateral dissipation oriented in the horizontal: (a) Si2hor and (b) Si2Hhor. Contour interval is 0.1. (c) shows the zonal mean vertically integrated tracer for these two cases (thick curves), where their counterparts with along-σ dissipation are also shown (thin curves) for an easy comparison. An increase in horizontal diffusivity leads to a thicker plume. Changing horizontal diffusivity has stronger influence on the tracer distribution than changing the along-σ diffusivity.

c) Sensitivity to the vertical mixing parameter

With the limiting value of vertical mixing coefficients increased to $A_{v0} = 0.2 \text{ m}^2 \text{ s}^{-1}$, both the allowed maximum vertical diffusivity and vertical viscosity are increased. Enhanced diapycnal mixing and Ekman transport play the role together. When the diapycnal mixing for tracers is increased, the dense plume is expected to be thicker. As shown in Fig. 5.13, the mean plume thickness increases with an increase in the limiting value A_{v0} on all the grids. The same trend can also be observed in the tracer cross sections (Figs. 5.9 to 5.12). The zonal mean vertically integrated tracer (Fig. 5.14f) shows that the location of maximum tracer thickness moves further offshore at higher limiting value A_{v0} on all different grids, although the sensitivity is dependent on the grids. At higher A_{v0} there is a much broader region of high tracer thickness at the downslope side of the plume in the σ grid simulation. On the partly shaved cell grid, the location of maximum tracer thickness is about 30 km further downslope than in the reference run. The increase in downslope penetration on the fully shaved cell grid is not so large, mainly due to its coarse vertical resolution. Although the location of maximum tracer thickness on the full cell grid is not significantly changed, there is also more tracer located at the downslope side of the plume when the limiting value A_{v0} is increased.

5.3.5   Entrainment and transport

As the overflow descends it entrains the ambient fluid, which modifies the tracer properties and increases the volume of the dense water mass (Price and Baringer, 1994; Girton and Sanford, 2003). Therefore, the ability to properly represent entrainment in overflows is of importance for a numerical model. In this section the properties of entrainment obtained with different vertical grids are to be examined.

a) Volume transport

By defining the dense plume by tracer concentration values greater than 0.01, the along slope transport can be calculated as (Legg et al., 2006)

$$\mathrm{T}(x) = \int_A u(x,y,z)\, \mathrm{d}y\mathrm{d}z, \ A \text{ is such that } c > 0.01, \tag{5.6}$$

where $u(x,y,z)$ is the zonal velocity. The spatial variation of the along slope transport is useful to quantify the entrainment. Strong variation in transport associated with meandering and eddies has been found in all runs, consistent to observations (Girton and Sanford, 2003) and model studies (Käse et al., 2003). The variation in transport can be attributed to the covariation of velocity and cross section area of the plume.

For an easy comparison, the zonal transport averaged over one week after 40 days for different runs is taken and shown in Fig. 5.18. The significant increase in zonal transport occurs mostly within the first 200 km downstream the inlet except for the coarsest z-level grid runs. The σ grid runs show much less variability in zonal transport than other grids when resolution is changed. On the σ grid, further increase in the zonal transport after $x = -200$ km only occurs at the coarsest resolution (20 km), and a trend of decrease in zonal transport after $x = -200$ km is found in both the 5 km and 2.5 km resolution σ runs.

On the full cell and partly shaved cell grids with resolution 20 km, the increase in transport within the first 200 km is quite small, and the transport continues increasing at a similar rate further downstream. On the z-level grids (full cell, partly and fully shaved cell grids) a decrease in transport (implying detrainment) after $x = -200$ km is only found at the highest resolution (2.5 km). At this resolution, the transport derived from the σ-grid and partly shaved cell grid runs are quite similar to each other showing similar maximal transport (amount and location) and the mean rate of (relatively small) detrainment after $x = -200$ km.

In the high lateral diffusivity runs using full cell and partly shaved cell grids (Fig. 5.18e), the zonal transport is larger than in the low diffusivity runs, consistent to the larger plume thickness observed in higher horizontal diffusion runs (Fig. 5.13). On the contrary, a decrease in the zonal transport is observed on σ grids with an increase in along-σ mixing, as implied by the reduced
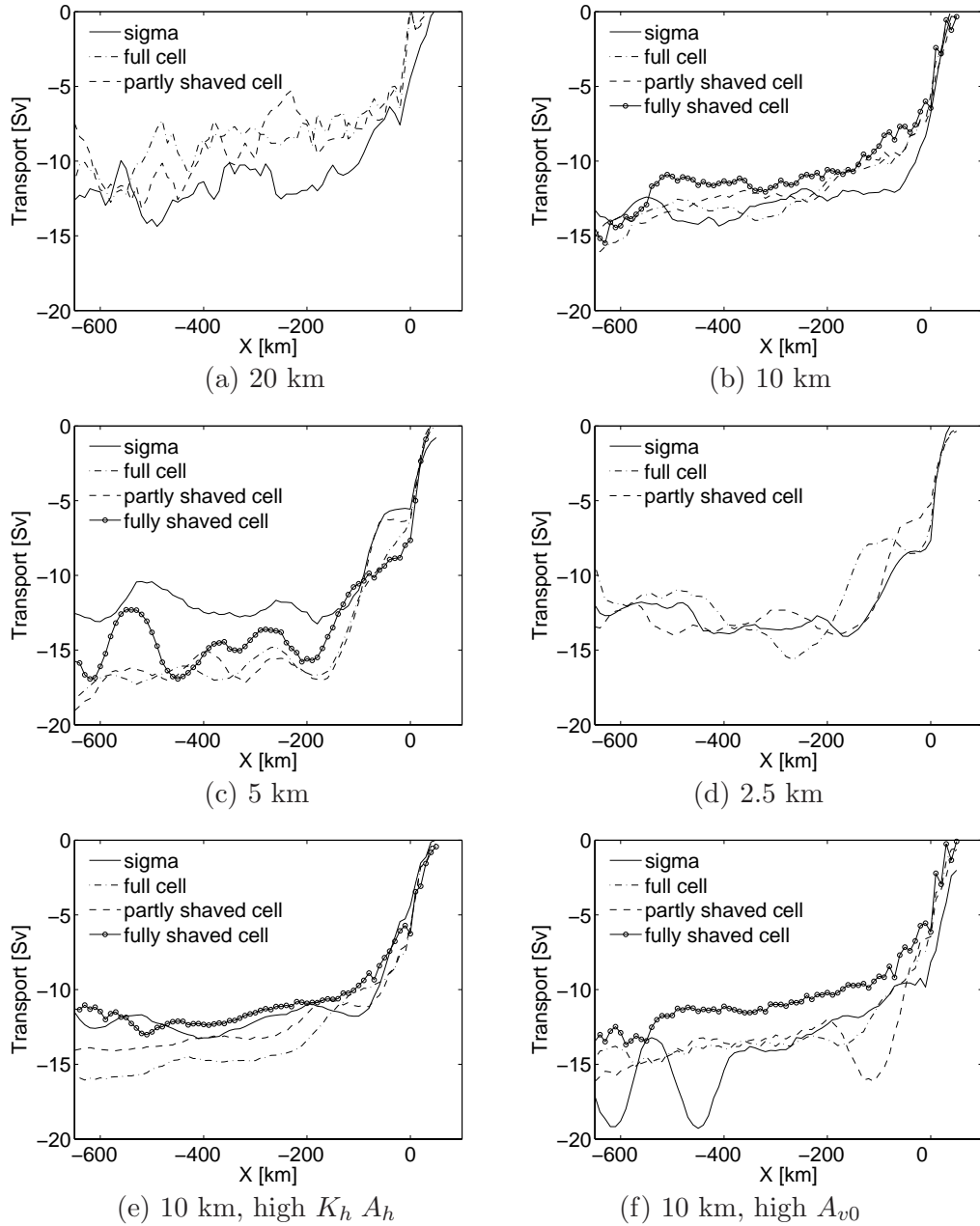
Figure 5.18: The along-slope transport averaged over one week after 40 days: for reference runs with horizontal resolution (a) 20 km, (b) 10 km, (c) 5 km, (d) 2.5 km; for (e) runs with lateral diffusivity of $100 \, \mathrm{m^2 \, s^{-1}}$; and for (f) runs with vertical mixing coefficient limiter value of $0.2 \, \mathrm{m^2 \, s^{-1}}$ with resolution of 10 km. The zonal transport on σ grids has less sensitivity to resolution than on other grids. A trend of weak detrainment beyond 200 km from the inlet can be observed on σ grids at both 5 and 2.5 km horizontal resolution. The transport on the full cell and shaved cell grids starts to converge to that on the σ grid at 2.5 km horizontal resolution. Note that the same vertical resolution (25 m) is used for both the 5 and 2.5 km z-level grids, and the difference in results implies that z-level grids need higher horizontal resolution to properly resolve the overflow.

dilution and plume thickness in the high dissipation run. The transport in the fully shaved cell grid is not changed significantly, mostly due to its coarse vertical resolution which, in this situation, could be a more important factor influencing the entrainment. Although a one week averaging is taken for the computation of transport, oscillations in transport can still be observed in reference runs, whereas oscillations are almost suppressed in high dissipation runs.

The influence of vertical mixing parameterizations on zonal plume transport is shown in Fig. 5.18f. Clear influence can be observed on all grids except the fully shaved cell grid. Increase in plume transport is enhanced in the partly shaved cell and full cell grids within the first 200 km from the source. The σ grid transport shows quite large oscillations at the downstream side. This can be explained by the fact that the along-slope propagation is slowed down when the plume is more diluted and farther transported downslope, and the head of the dense plume has just passed by the location of strong oscillations. It appears that the σ run with $A_{v0} = 0.2 \text{ m}^2 \text{ s}^{-1}$ at 10 km resolution does not reach a quasisteady state in the whole domain after 40 days.

b) Tracer distribution in the density space

The total tracer distribution as a function of along slope distance and density anomaly $\Delta \sigma_T$ (referenced to surface in kg m^{-3}) has been proposed by Legg et al. (2006) to illustrate the property of dense plume water formation. Figures 5.19 and 5.20 show this diagram for simulations at 10 km and 5 km resolution, respectively. The source water is located at the lower right corner of the diagram, with density anomaly of 2 kg m^{-3} as prescribed for inflow conditions. In both resolution σ runs, the maximum in tracer moves rapidly to lighter density classes as the overflow moves westward and downslope. The diapycnal mixing occurs mainly within $100-200$ km from the inlet, after which the tracer maximum is not changed significantly, remaining between $1.4 < \Delta \sigma_T < 1.6$ at both resolutions. The region of strong diapycnal mixing coincides with the region of significant entrainment (increase in transport), so the entrainment is largely diapycnal, as expected from the previous study employing the non-hydrostatic physics (Legg et al., 2006). The plume is clearly less diluted on the σ grid than on others, indicated by a smaller region of density classes not reached by overflows (the blue region at the bottom of the diagram).

In the full cell simulations diapycnal mixing and entrainment appears to occur over a longer distance. The maximum tracer is located at about $\Delta \sigma_T = 1.1$ in the 10 km run, associated with a lighter neutral buoyancy level than in the σ simulation. When the resolution is increased to 5 km, entrainment is reduced on the z-level grids, indicated by denser plume water. Both the partly and fully shaved cell simulations show a distance of strong diapycnal mixing similar to that in the σ runs. Although the maximum tracer is located in lighter density classes on the partly and fully shaved cell grids than on the

σ grids, the partly and fully shaved cell grids have less diluted plume water than the full cell grid.

The final plume density (anomaly to the surface) averaged over -600 km $< x < -200$ km for different reference runs is shown in Fig. 5.22. This plot clearly shows that the mean density increases with an increase in resolution on different grids except for the finest σ grid run. The σ grid simulations have the least resolution sensitivity. At each resolution, the mean plume density is the highest on the σ grid, then the second highest on the partly shaved cell grid.

$$\Delta x = 10 \text{ km}$$

(a) σ grid

(b) full cell

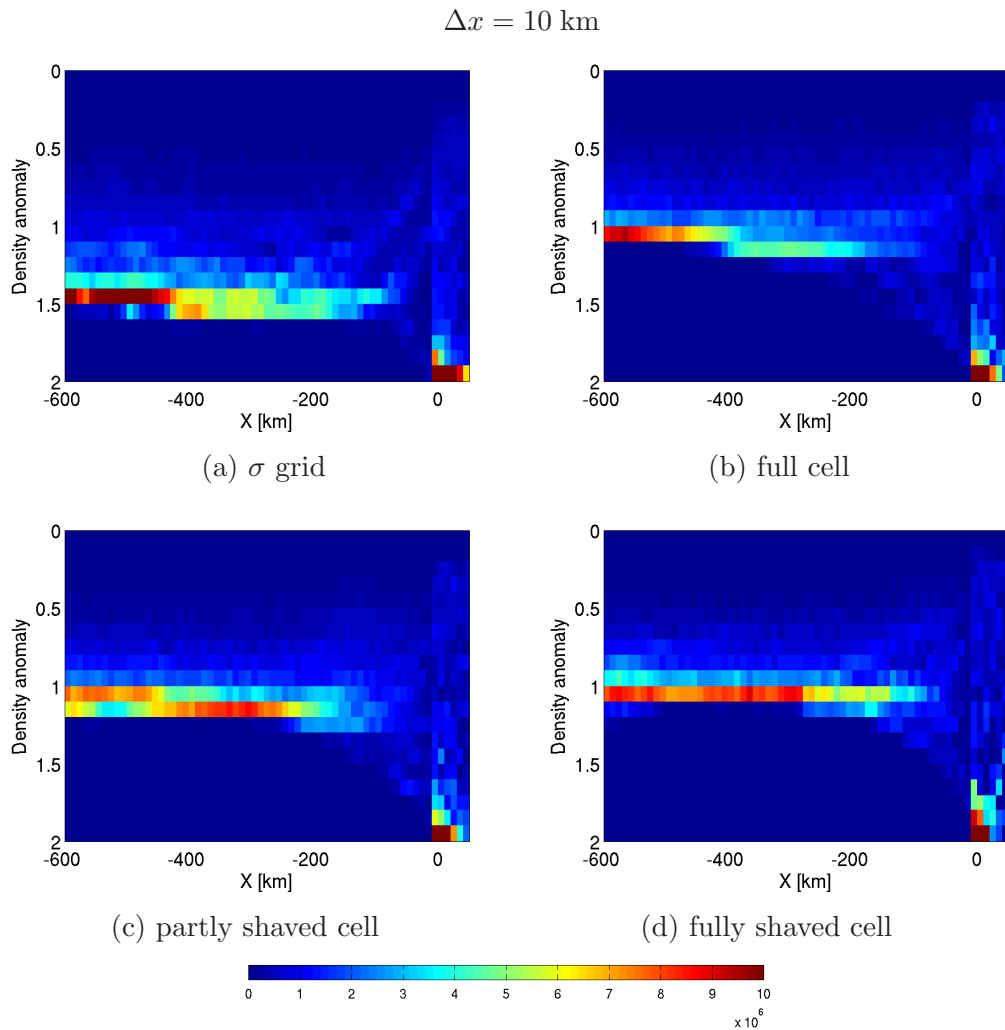(c) partly shaved cell

(d) fully shaved cell

Figure 5.19: Total tracer averaged over one week after 40 days as the function of downstream distance (x) and density anomaly class (y) for runs at 10 km resolution: (a) Si2, (b) FC2, (c) PSC2, (d) FSC2. The overflow is less entrained on the σ grid than on others. Entrainment takes place mainly within the region 100-200 km from the inlet on the σ and shaved cell grids, but over a longer distance on the full cell grid.

$\Delta x = 5$ km

(a) σ grid

(b) full cell

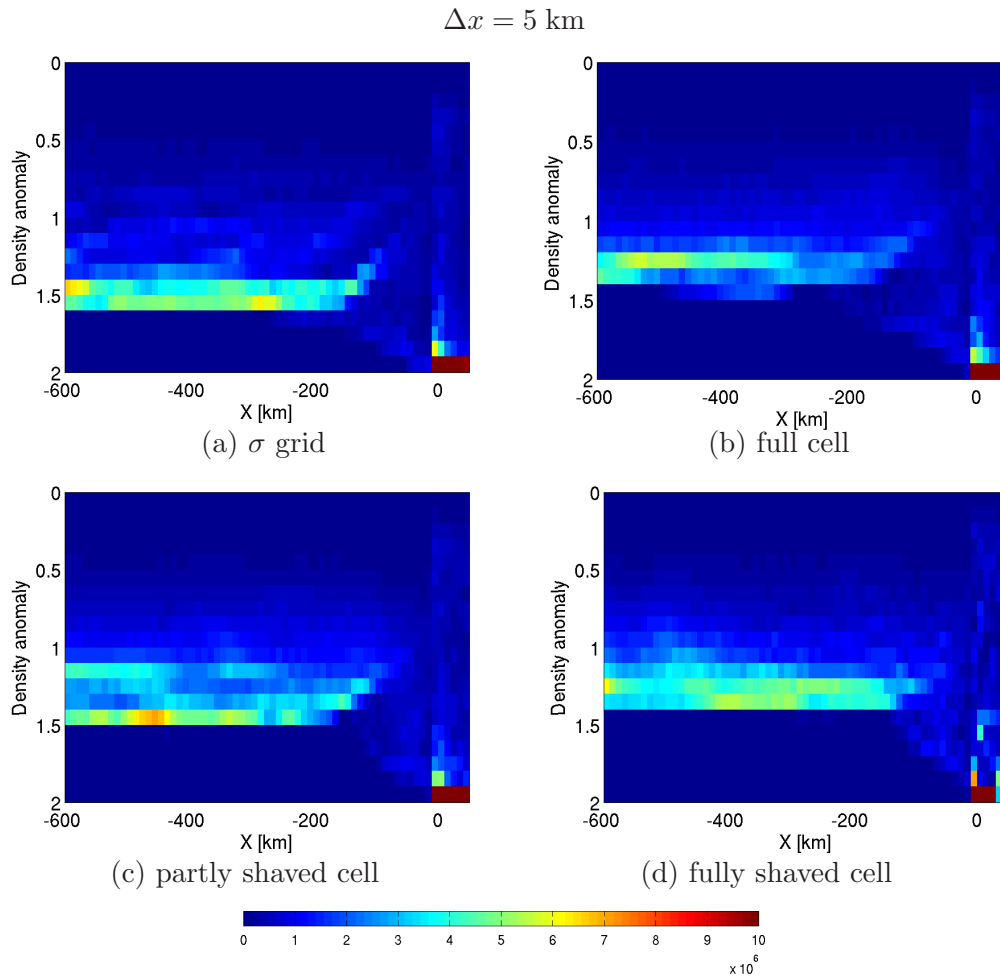(c) partly shaved cell

(d) fully shaved cell

Figure 5.20: As Fig. 5.19 but for runs at 5 km resolution: (a) Si3, (b) FC3, (c) PSC3, (d) FSC3. Entrainment is reduced on all the z-level grids with the increase in resolution.
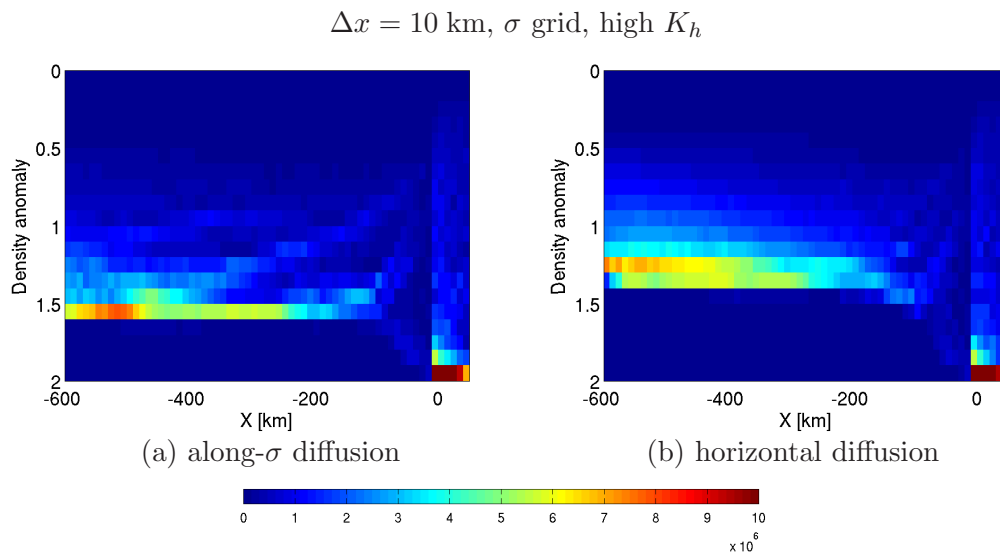
$\Delta x = 10$ km, σ grid, high K_h

(a) along-σ diffusion

(b) horizontal diffusion

Figure 5.21: As Fig. 5.19 but for σ runs with high diffusivity of 100 m^2 s^{-1}: (a) along-σ Si2H, and (b) along geopotential direction Si2Hhor. This comparison clearly shows the diapycnal mixing effect of the horizontally oriented diffusivity.

The partly shaved cell grid results converge to the σ grid results faster than the full cell runs, especially at the finest resolution. The fully shaved cell grid has plume density similar to that in the full cell grid, and lower than in the partly shaved cell grid. Once again this is due to the coarser vertical resolution used in the fully shaved cell grid, which appears coarser than required for solving the dense plume.
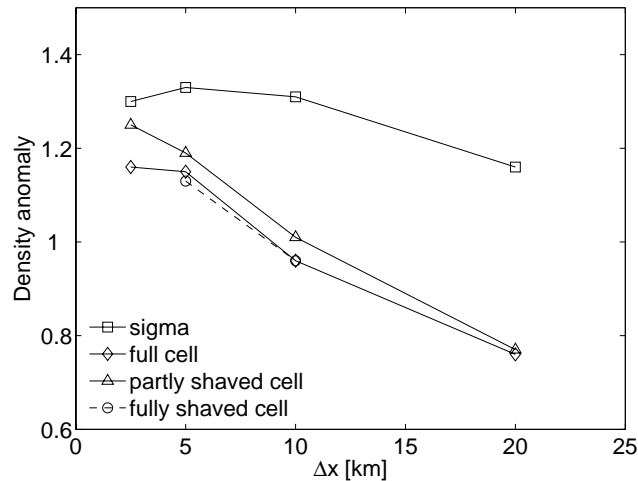

Figure 5.22: Overflow plume density (anomaly to surface) averaged over -600 km $< x < -200$ km as the function of resolution. The σ grid produces a denser overflow plume, and it is not very sensitive to the horizontal resolution. With increased resolution (both horizontal and vertical), the plume density on z-level grids starts to converge to that on the σ grid. Plume density increases further on the partly shaved cell grid when horizontal resolution is increased from 5 km to 2.5 km (at the same vertical resolution), which demonstrates the higher requirement for horizontal resolution by z-level grids. The results on the fully shaved cell grids, which have lower vertical resolution than other grids, emphasize the importance of vertical resolution.

Consistent to the findings from the plots of plume transport, both an increase in lateral diffusivity and an increase in vertical mixing coefficients can cause more tracer to be distributed in lighter buoyancy classes on the full cell and partly shaved cell grids (diagram not shown). However, an increase in lateral diffusivity causes more tracer to be in heavier water classes on the σ grid (Fig. 5.21a). On the contrary, in the σ run with geopotentially oriented diffusivity of 100 m^2 s^{-1} (Fig. 5.21b), most tracer is located in much lighter buoyancy classes, indicating stronger entrainment, as can be expected from the increased plume thickness (Fig. 5.13) and reduced bottom tracer concentration (Fig. 5.16). As stated previously, it is the increased diapycnal mixing contributed from the geopotentially oriented diffusion that directly enhanced the simulated entrainment.

c) Vertical mixing coefficients

The vertical viscosity (5.1) in the cross section at $x = -50$ km after 40 days for each run is shown in Figs. 5.23 and 5.24. Parameterized vertical diffusivity is not shown here, from which the same general conclusions can be drawn as below. Larger vertical viscosity (corresponding to smaller local gradient Richardson number) is mostly found at the upslope side of the plume, which is consistent to previous simulations (Ezer, 2005; Tseng and Dietrich, 2006). In the reference runs, the σ grid has smaller regions of viscosity above 0.03 m^{2}s^{-1} (blue patches) than the full cell and partly shaved cell grids in coarse resolution runs. Larger viscosity (also diffusivity) found in full cell and partly shaved cell grids indicates excessive vertical mixing due to the effects of artificial stairs. So more diluted plume is generally found in these grids (Fig. 5.22). With an increase in resolution the area of large vertical viscosity is reduced, as expected from the better resolved bottom mixing layer in the fine resolution full cell and partly shaved cell runs (Fig. 5.15). On the fully shaved cell grid, there is no so excessive vertical mixing as in the full cell and partly shaved cell grids because of its accurate bottom representation. In fact, the vertical mixing coefficient in the fully shaved cell grid is even smaller than that on the σ grid. This should be attributed to larger gradient Richardson numbers caused by the poorly resolved (smaller) velocity shear with coarser vertical resolution in the fully shaved cell grid.

On all grids, increasing permitted maximum vertical mixing coefficients leads to much larger regions of strong vertical mixing, which is responsible for enhanced entrainment and thicker plume (Fig. 5.13). With an increase in lateral diffusivity/viscosity, regions with large parameterized vertical mixing coefficients are more confined to the bottom, shown by thinner areas of contour lines in all high diffusivity/viscosity runs. Reduction in areas of large vertical mixing coefficients is not necessary related with a thinner plume. As previously stated, decrease in plume thickness with an increase in lateral dissipation is only found in the σ grid experiments when along-slope diffusivity/viscosity is applied. It appears that diapycnal mixing due to horizontally oriented diffusivity plays an important role in having larger entrainment and plume thickness on z-level grids. This point becomes clearer by comparing the Si2H and Si2Hhor cases. In the Si2Hhor case, the parameterized vertical mixing coefficients are smaller, while the plume is much more diluted (Fig. 5.16b).

5.4 Summary

In this section FEOM has been used to simulate overflows in the idealized DOME configuration. Our major attention was to the influence of different types of vertical discretization supported by FEOM on the properties of the simulated plume. However, issues such as resolution and subgrid scale mixing
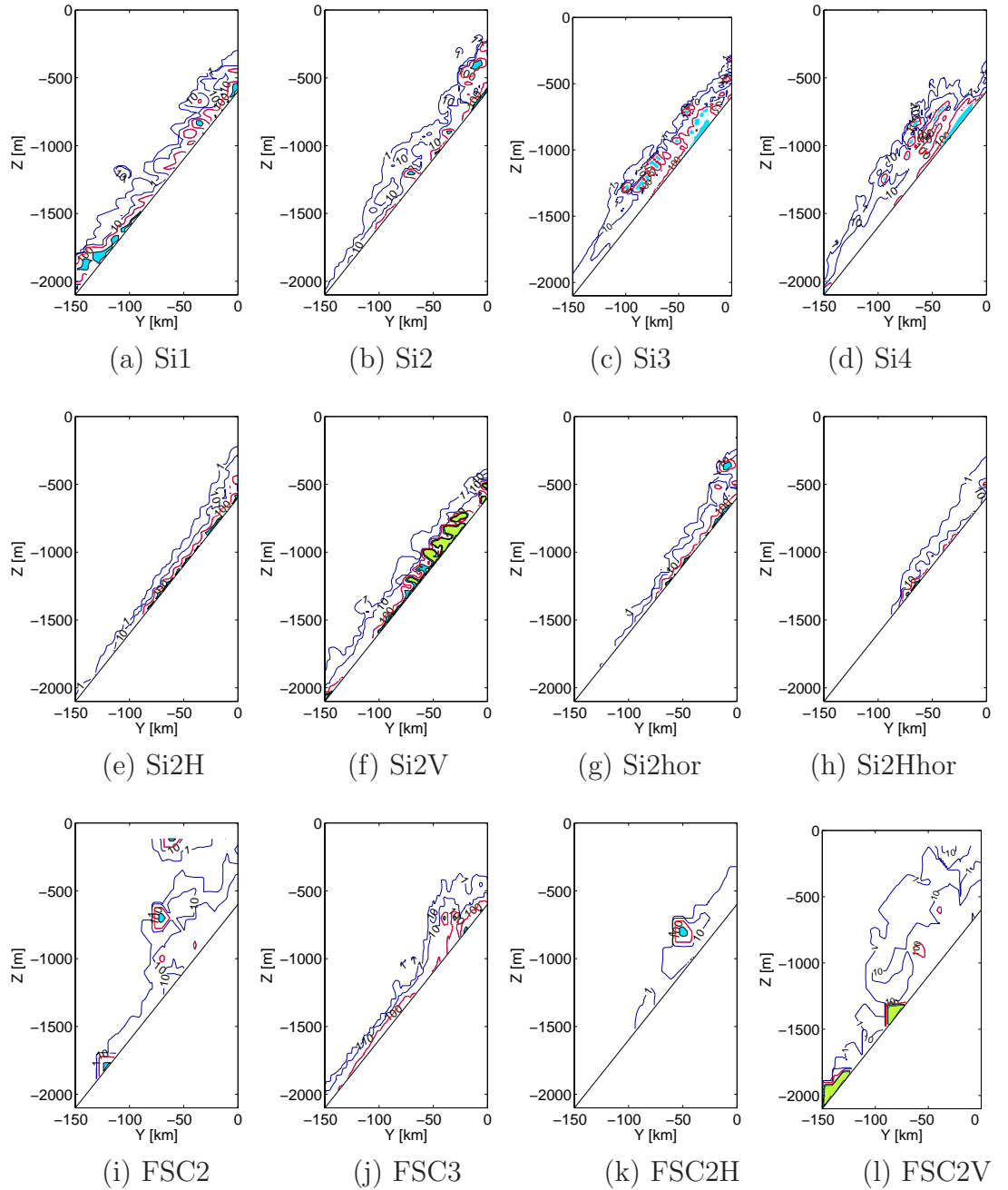
Figure 5.23: Vertical viscosity (A_V in unit of 10^{-4} m^2 s^{-1}) in the cross slope section 100 km downstream the inlet after 40 days for σ and fully shaved cell grids. The contour lines for [1, 10, l00] are shown; the contour line for 100 is in red. Blue patches represent areas with values between 300 and 500, and the green patches for areas with values above 500. Note that the parameterized vertical mixing is small in (h), where large horizontal diffusivity is used. So strong dilution observed in this case is attributed to the diapycnal mixing due to the horizontal diffusion.
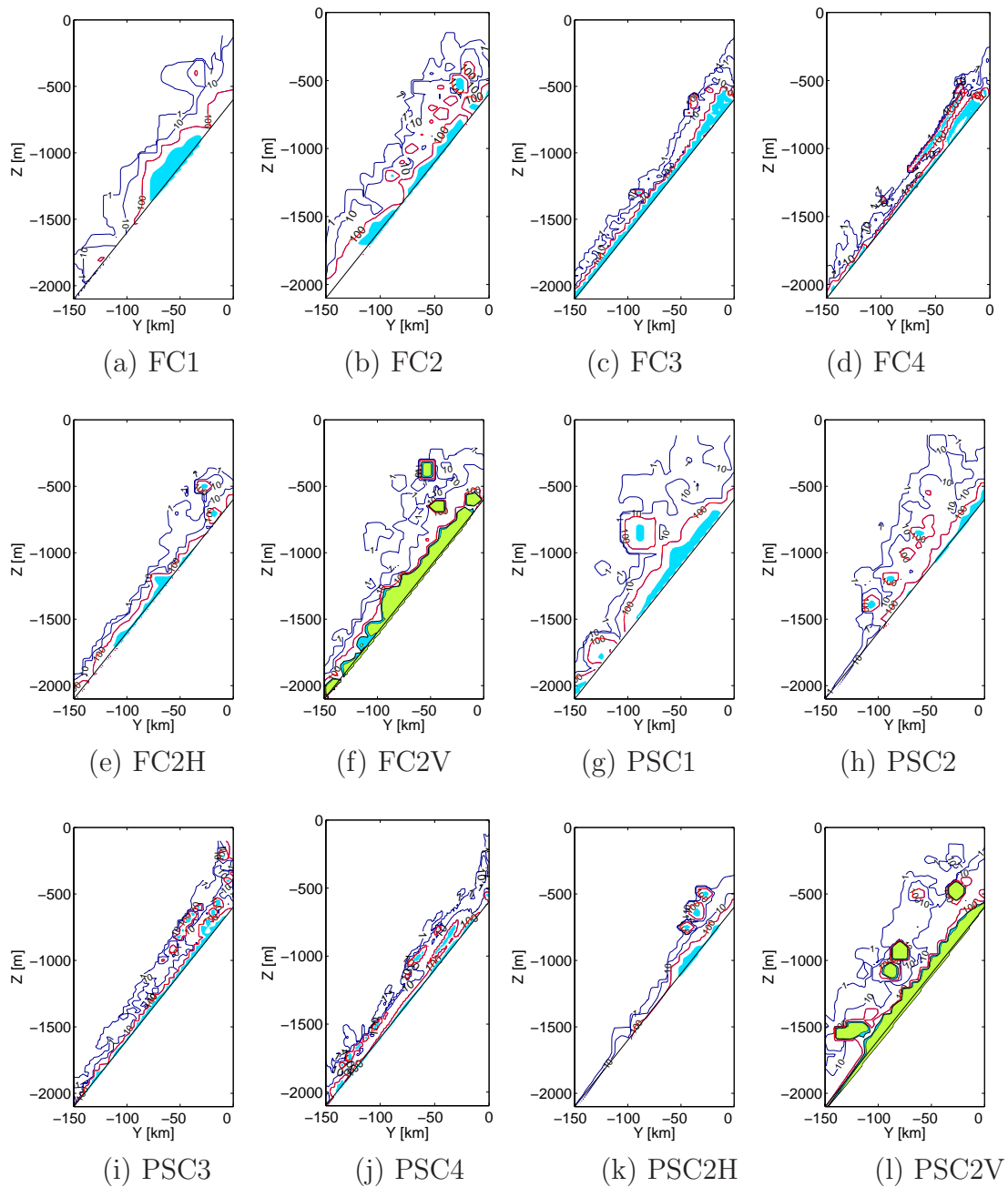
Figure 5.24: As Fig. 5.23 but for full cell and partly shaved cell grid runs. Note that the vertical mixing coefficient is larger on the full cell and partly shaved cell grids than their counterpart of σ grids in Fig. 5.23. But the full cell grids have larger vertical mixing than the partly shaved cell grids.

are also important factors determining the properties of overflows. The study here touched these aspects, too.

In the σ (also $z + \sigma$) grid simulations the DOME overflow plume converges to a low-diluted solution very fast with the increase in resolution. The 5 km resolution run appears to be able to fully resolve large scale structures. The σ grid shows less sensitivity to resolution than other grids. Even the coarsest σ run still reproduces the pattern obtained at finer resolution. The dense plume features, including plume thickness, downslope penetration distance, large scale eddies, and the accompanying diapycnal mixing and entrainment on the σ grid agree well with previous studies (e.g., Ezer and Mellor, 2004; Ezer, 2005; Legg et al., 2006).

The volume transport on σ grids is increased by a factor of 2-3 within the first 100 to 200 km from the entrance, accompanied by strong entrainment and dilution in this region. A slight but clear detrainment beyond 200 km from the source was observed in σ runs at resolution of 5 and 2.5 km. The occurrence of detrainment has also been reported by Ezer (2005). Although more observations are required to justify the location of detrainment in the real ocean, the finding in the current work is consistent to the study of Killworth (2001). Through a simple dynamical analysis under the assumption of local turbulent equilibrium, Killworth (2001) argued that entrainment is confined to small regions where topography varies rapidly, whereas detrainment can be expected when the slope angle is uniform (or decreasing) and the stratification of the surrounding water is stable.

The dense plume simulated on full cell grids is confined to the northern boundary and is excessively diluted when the resolution is not very fine. The difficulty of z-level grids in simulating overflows is mainly due to its step-like bottom representation. Static instability over these artificial "stairs" can result in intensive spurious vertical mixing, leading to overestimated dilution. By introducing shaved cells at the bottom, the z-level grid can better resolve the overflow dynamics and mixing. At 2.5 km resolution the partly shaved cell simulation results appear to approach the σ grid results in terms of downslope propagation, bottom mixing layer thickness and final plume density, but finer resolution could still be required for the partly shaved cell grid to converge to the less diluted plume of the σ solution. Strong resolution dependence in z-level grid simulations has been generally observed. Similarly, the study by Legg et al. (2006) shows that isopycnal models also have less sensitivity to resolution than z-level models.

The fully shaved cell grid (Fig. 1.3b) can represent topography accurately. In the current work, simulating overflows did not benefit more from this accurate continuous bottom representation than from general partly shaved cell grid which could contain artificial "stairs" in places, because the fully shaved cell grid is realized by reducing vertical resolution (to match the fixed horizontal resolution). Deciding which kind of shaved cell grid is beneficial appears to be application dependent. The results from the experiments with fully shaved

cell grids confirmed the necessary vertical resolution, O(25 m), for this model configuration.

With an increase in horizontal dissipation, the overflow plume is more diluted and gets more entrained on z-level grids. On the σ grids, increasing the along-σ mixing leads to a slightly thinner plume. But when diffusivity is oriented in the geopotential direction, the plume simulated on the σ grid will also be more diluted. The reason is horizontally aligned diffusion can lead to diapycnal mixing and entrainment. Applying along-σ diffusion on the σ grid can avoid interacting with vertical mixing scheme. To avoid such numerical entrainment, high horizontal diffusivity/viscosity should not be used when simulating overflows on z-level grids, which is also suggested by the work of Tseng and Dietrich (2006). One general remedy is to use isoneutral diffusion.

The Richardson-number-dependent mixing scheme (Pacanowski and Philander, 1981) can approximate vertical mixing well. Its role in mixing tracers to provide necessary entrainment and in downslope Ekman transport is illustrated through sensitivity studies. The vertical mixing coefficient shows a spatially asymmetric structure across the plume with stronger mixing over a thicker BBL at the upslope side of the plume, as shown in Ezer (2005) and Tseng and Dietrich (2006). The Mellor-Yamada turbulence scheme (Mellor and Yamada, 1982) has been shown to be able to approximate vertical mixing properly using the DOME configuration by Ezer (2005). The remaining difference in detailed plume features (e.g., the across-slope tracer distribution) indicates that further research on entrainment approximation is required. Yet final answer can only be found by combining field observations, laboratory studies and model simulations.

Although partly and fully shaved cell grids are not so successful as σ grids in simulating bottom trapped overflows, it has been shown that they can at least reduce grid scale errors induced by artificial "stairs" in the z-level grid (Chapter 3 and 4, also see Adcroft et al., 1997; Pacanowski and Gnanadesikan, 1998). Therefore, their application in OGCM can improve the representation of ocean topography and the ocean circulation. Note that pressure gradient errors on grids with skewed lattices (in σ coordinate models and also in FEOM when σ grid is used) cannot be fully eliminated even with the most sophisticated methods (Ezer et al., 2002). In the partly and fully shaved cell grids the pressure gradient errors exist only in the bottommost elements (when one layer of shaved cells applied), whereas pressure gradient errors pollute solutions in all σ layers in a σ grid. When both the general circulation and dense water formation are to be more accurately simulated, the $z + \sigma$ grid (Fig. 1.2c) is recommended. The number and resolution of σ layers at the bottom can be chosen according to applications.

Chapter 6

Conclusions

Bottom topography determines the physics of many processes in the ocean, yet its proper representation in ocean circulation models still presents a challenge for the modelling community. An approach proposed in this work suggests several solutions which are realized within a new version of FEOM and allow the bottom topography to be represented continuously or partly continuously in the numerical domain. FEOM supports a hybrid or generalized vertical discretization which does not require the number of vertical layers be the same within the model domain. It can work on σ grids and grids combining z and σ levels, and also supports (partly) shaved cell bottom representation within the z-level framework.

The choice of the vertical grids is delegated to the mesh design, so the support for different types of vertical grids and bottom representation is realized within the same numerical core. This is possible because the grid is treated as a collection of elements in FEOM.

The performance of different grid types was studied in this work by simulating the eddy shedding off a Gaussian seamount, lee waves downstream it, the topographic waves in a rotating stratified channel, and dense water overflows under the framework of the DOME configuration. The five grid types explored here include the old-fashion full cell z-level grid, the σ grid, the combined $z+\sigma$ grid, and z-level grids with partly and fully shaved bottom cells.

The main question answered in this work is how these grids perform. Additionally, since the test cases were specially selected among those that are sufficiently well documented in the literature, the intercomparison results can be considered as tests of the overall FEOM performance, which are successfully passed.

The main results of this work are formulated below.

1. The support for hybrid vertical grids is implemented in FEOM. The model as a whole is also developed to be more efficient and versatile for ocean modelling.

2. A nonlocal spline interpolation method is suggested and implemented

for the computation of pressure gradients. By comparing the spurious velocity and kinetic energy caused by pressure gradient errors on σ grids in a standard seamount configuration, this method is shown to be much more accurate than a direct calculation method described in Ford et al. (2004a), and reaches the level of state-of-the-art techniques employed in FD σ coordinate models.

3. It is shown that the $z + \sigma$ and shaved cell grids clearly reduce the pressure gradient errors with respect to the pure sigma grid in the standard seamount configuration.

4. Simulations of steadily forced flow past an isolated seamount show that full cell z-level grids are incapable of producing correct fields of density and vertical velocity. Modifying these grids with (partly) shaved bottom elements improves the grid performance considerably. The partly shaved cell grid can still contain grid-scale noise over the steep part of the topography where vertical walls are allowed. The noise disappears if the whole bottom is continuously represented by employing fully shaved cells. Results obtained with the σ and $z + \sigma$ grids are almost identical, and are also very similar to those obtained on σ grids by others.

5. In the simulation of topographic waves in a rotating stratified channel, the full cell grid produces unrealistic dispersion relation because it cannot resolve gentle slopes at moderate vertical resolution commonly used for the deep ocean. After adding shaved cells to the z-level grid (i.e., to realize continuous bottom representation) the dispersion relation for such topographic waves can be reproduced very accurately.

6. Both σ and $z + \sigma$ grids approximate density-driven overflows in the DOME configuration with very similar skills in terms of plume thickness, downslope propagation distance, entrainment and final density classes. They have much less resolution sensitivity than other grids that we employed. Their results compare well with those obtained with σ and isopycnal models by other authors. The solutions on partly shaved cell grids can approach those on σ grids, yet excessively high horizontal and vertical resolution is required to achieve it.

Discontinuity in the bottom topography representation can indeed influence model simulation results. However, removing the discontinuities of the bottom with the shaved cells does not always solve all problems, as solutions still depend on vertical resolution (for a fixed horizontal mesh). In this respect σ and $z + \sigma$ grids are better suited to problems involving essential dynamics close to bottom as they can easily provide necessary vertical resolution there. Considering the problem of pressure gradient errors, the $z + \sigma$ grids are more beneficial in realistic oceanographic applications.

In addition to vertical discretization and bottom representation, the dynamics can also be affected by the orientation of diffusivity, as spurious diapycnal mixing generated by horizontal or along-sigma diffusion can interact with adopted diapycnal mixing approximations. In the particular case of simulating overflows, along-sigma diffusion is found to be superior to horizontal diffusion simply because isopycnals are mainly parallel to the slope in this case. Neutral physics dominates in the interior of the ocean, so diffusion in the isoneutral direction should be applied in large scale simulations, the functionality of which is available in FEOM.

This work opens perspectives of using FEOM in studies of dense water formation processes in the world ocean. The effects of topographic steering by seamounts and canyons and the influence of tides are to be explored in both an idealized configuration and in a regional model of the Weddell Sea as a continuation of the current work. The coupling of the current model with a sea ice module based on the FE method is under testing. The coupled model is planned to be used for regional studies on the Arctic Ocean and the Southern Ocean.

Appendix A

Primitive equations in general coordinates

This appendix shows the primitive equations in a general coordinate and illustrates some properties of particular coordinate formulations. More background for the coordinate transformation can be found in Haltiner and Williams (1980) and Griffies (2004). Overviews of different models are referred to Haidvogel and Beckmann (1999) and Griffies et al. (2000a).

The hydrostatic primitive equations in a general or hybrid coordinate, (x, y, s), can be written as:

$$D_t \mathbf{u} + f \mathbf{k} \times \mathbf{u} + \frac{1}{\rho_0} \nabla_s p + \frac{g\rho}{\rho_0} \nabla_s z = \mathcal{F} \tag{A.1}$$

$$\partial_s p + g\rho \partial_s z = 0 \tag{A.2}$$

$$\partial_t \eta + \nabla \cdot \int \mathbf{u} \, \partial_s z \, \mathrm{d}s = \mathcal{P} \tag{A.3}$$

$$\partial_t (\partial_s z) + \nabla_s \cdot (\partial_s z \, \mathbf{u}) + \partial_s (\partial_s z \, \dot{s}) = 0 \tag{A.4}$$

$$D_t C = q \tag{A.5}$$

$$\rho = \rho(T, S, z), \tag{A.6}$$

where $\mathcal{F}$ is the horizontal force resulting from stresses, $\mathcal{P}$ is the fresh water source, C stands for potential temperature T or salinity S, q is the corresponding source for tracer C, ∇_s is the horizontal gradient taken along surfaces of constant generalized vertical coordinate s, and the total time derivative of a property ϕ denotes:

$$D_t \phi = \partial_t \phi|_s + \mathbf{u} \cdot \nabla_s \phi + \dot{s} \partial_s \phi. \tag{A.7}$$

Note that the z coordinate equations can be readily recovered from above expressions by setting $s = z$.

By defining a transformation relation $s = \sigma \equiv \sigma(x, y, z)$, one gets the terrain-following or σ coordinate equations. A properly chosen transformation

relation (e.g., Song and Haidvogel, 1994) can provide refined vertical resolution where it is required, for instance, in both the surface and bottom boundary layers. In σ coordinate models, the pressure gradient force in the horizontal momentum equation (A.1) is:

$$\frac{1}{\rho_0}\nabla_z p = \frac{1}{\rho_0}\nabla_\sigma p + \frac{g\rho}{\rho_0}\nabla_\sigma z, \tag{A.8}$$

where $\nabla_z p$ is the horizontal pressure gradient taken along surfaces of constant depth z. On slopes of continental shelves and seamounts, the two terms on the right-hand side of the above expression could be on the same order. In this situation, a very accurate numerical representation of these two terms should be employed in order to obtain an accurate pressure gradient force, otherwise the "pressure gradient error" could cause severe spurious motion. For reviews of the development of σ coordinate models one is referred to Greatbatch and Mellor (1999) and Ezer et al. (2002).

When the vertical coordinate is the potential density, the proxy of entropy, the horizontal momentum equation (A.1) can be written as:

$$D_t \mathbf{u} + f\mathbf{k} \times \mathbf{u} + \nabla_\rho M = \mathcal{F}, \tag{A.9}$$

where $M \equiv p/\rho_0 + \rho g z/\rho_0$ is the Montgomery potential, and the hydrostatic equation becomes

$$\partial_\rho M = \frac{gz}{\rho_0}. \tag{A.10}$$

It is assumed that potential density is equal to in situ density in the above derivation, that is, the equation of state is linear. In this case, the pressure gradient force in the horizontal momentum equation (A.9) consists of only one term, so isopycnal models do not suffer from the problem of pressure gradient errors. The continuity equation (A.4) in the isopycnal model is written as:

$$\partial_t(\partial_\rho z) + \nabla_\rho \cdot (\partial_\rho z \, \mathbf{u}) + \partial_\rho(\partial_\rho z \, \dot{\rho}) = 0, \tag{A.11}$$

which becomes a layer thickness equation for each density class. Isopycnal coordinate models maintains all spurious mixing within density classes, and do not allow spurious diapycnal mixing. This is a distinct advantage of isopycnal coordinate models. For details about the realization of isopycnal coordinate models, one is referred to the descriptions of HIM (`http://www.gfdl.noaa.gov/~rwh/HIM/HIM.html`) and MI-COM (`http://oceanmodeling.rsmas.miami.edu/micom/`).

Each single coordinate has its advantages, but each has particular difficulty in faithfully representing the large scale circulation over climate time scales. Efforts have been made to employ a z or pressure coordinate for the surface boundary layer, an isopycnal coordinate for the ocean interior, and σ coordinate near the bottom in hybrid coordinate models (e.g., HYCOM, Bleck, 2002). One essentially important utility in hybrid coordinate models

is the so-called vertical grid generator (Bleck, 2002, 2006), which determines where different coordinates are located and how particular layer thickness is constrained or made massless.

Appendix B

A list of symbols

Table B.1: Symbols

symbol	meaning
A_h	horizontal viscosity
A_v	vertical viscosity
A_{v0}, α, n	control parameters in the vertical mixing scheme
$\mathbf{B}$	matrix of the bottom stress term in the momentum equation
Bu	Burger number
c	phase speed
c_1	approximate first baroclinic gravity wave speed
C	tracer; stand for T or S
C_d	bottom drag coefficient
$\mathbf{C}$	matrix of the hydrostatic pressure term
d	ocean depth (distance from the surface)
$\mathbf{D}_\Phi$	matrix of the velocity divergence term in the continuity equation
Ek	Ekman number
f	Coriolis parameter
f_1, f_2	tapering functions in the neutral physics scheme
$\mathbf{f_1}, \mathbf{f_2}$	boundary forcing in discrete momentum and elevation equations
$\mathcal{F}$	stress force in the horizontal momentum equation
$F(\sigma)$	the σ grid stretching function
$F_{e,i}$	antidiffusive flux from element e to node i in the FCT scheme
$\mathbf{F}$	Redi diffusive flux, or the full SGS flux
$\mathbf{F}_{skew}$	GM skew flux
Fr	Fround number
g	gravitational acceleration
$\mathbf{G}$	matrix of the surface pressure term in the momentum equation
h_{min}	minimum ocean depth in the model domain
$h(x,y)$	ocean bottom depth
H	vertical length scale
$\mathbf{H}$	matrix of the Laplacian term in the elevation equation
k_x, k_y	zonal and meridional wavenumbers
$\mathbf{k}$	vertical unit vector

Table B.1: Symbols

symbol	meaning
K_h	horizontal diffusivity
K_v	vertical diffusivity
K_I	isoneutral diffusivity
K_D	dianeutral diffusivity
$\mathbf{K}_{Redi}$	Redi diffusion tensor
$\mathbf{K}, \mathbf{K}'$	matrix of the diffusion term in momentum and tracer equations
L	horizontal length scale
$\mathbf{L}$	matrix of the Coriolis term in the momentum equation
M	Montgomery potential
$\{M_j\}$	2D basis functions
M	number of nodes in the 2D mesh
$\mathbf{M}$	mass matrix
$\mathbf{M}_C, \mathbf{M}_L$	consistent mass matrix and lumped mass matrix
$\mathbf{M}_u, \mathbf{M}_\eta, \mathbf{M}'$	mass matrix in equations of momentum, elevation and tracers
$\mathbf{M}_\Phi$	matrix of the left-hand side operator in the continuity equation
$\mathbf{n}$	2D normal unit vector
$\mathbf{n_3}$	3D normal unit vector
N	buoyancy frequency
$\{N_j\}$	3D basis functions
N	number of nodes in the 3D mesh
$\mathbf{N}$	matrix of the advection term in the momentum equation
$\mathbf{N}_s, \mathbf{L}_s$ $\mathbf{C}_s, \mathbf{G}_s$	matrix of the stabilization terms in the momentum equation
$\mathbf{N}'$	matrix of the advection term in tracer equations
$\mathbf{N}'_s$	matrix of the stabilization term in tracer equations
$\mathbf{O}$	matrix of the open boundary term in the elevation equation
$\mathbf{O}_\Phi$	matrix of the open boundary term in the continuity equation
p	hydrostatic (baroclinic) pressure
p^f	full pressure
$\mathcal{P}$	fresh water source
$P^\pm$	sum of positive and negative antidiffusive flux in the FCT scheme
$\mathbf{Px}, \mathbf{Py}$	the x and y components of the pressure gradient forces
q	surface flux for T or S
Q	combination of particular terms in tracer or momentum equations
$\{Q_k\}$	discontinuous piecewise-linear basis functions
Q	the number of discontinuous functions $\{Q_k\}$
$Q^\pm$	admissible variable increment in the FCT scheme
R	rotation matrix
$R^\pm$	bounds for limiting factors in the FCT scheme
$\mathbf{R}, R_x, R_y$	discrete equations' right-hand side and its x and y components
Ro	Rossby number
Ri	local gradient Richardson number
s	general vertical coordinate
S	salinity

Table B.1: Symbols

symbol	meaning
$\mathbf{S}, S_x, S_y$	neutral slope and its x, y components in describing neutral physics
S_{max}, S_d	parameters in the tapering function f_1
$\mathbf{S}$	matrix for the wind stress term in the momentum equation
$\mathbf{S}'$	matrix of the surface flux term in the tracer equation
$\mathbf{S}_\Phi$	matrix for the surface integration term in the continuity equation
t	time
T	potential temperature
$\mathbf{u}$	horizontal velocity
$\mathbf{u}^*$	auxiliary horizontal velocity
$\mathbf{v}$	3D velocity
$\mathbf{v}^*$	advective bolus velocity
u, v, w	the three components of velocity
$\mathbf{u}^{rot}, \mathbf{u}_t, \mathbf{u}_n$	rotated velocity vector and its tangential and normal components
$\mathbf{u}_{OB}^{\perp}$	open boundary velocity
$\mathbf{U}_{OB}^{\perp}$	vertically integrated open boundary velocity
U	general one dimensional velocity
x, y, z	Cartesian directions
$\boldsymbol{x}(\boldsymbol{\xi})$	coordinate mapping between the parent domain and Ω
$\tan\alpha$	topography slope
α, β, d	parameters used in the implicit form of the dynamical equations
α_e	limiting factor in the FCT scheme
γ	parameter controlling the strength of pressure mode stabilization
δ	traveling distance used in describing CG method
δ	fractional height of seamount elsewhere
ϵ	the ratio of the dianeutral to isoneutral diffusivity
ϵ_{AB}	parameter stabilizing the second-order Adams-Bashforth method
ε	parameter determining the antidiffusive flux in the FCT scheme
$\hat{\zeta}/f$	vertically integrated relative vorticity
η	surface elevation
θ	θ method representing the temporal discrete form
θ_1, θ_2	σ grid stretching parameters
κ	skew diffusivity
λ_1	the first baroclinic Rossby radius
μ	Courant number
$\boldsymbol{\xi}, (\xi, \chi, \zeta)$	coordinates in the parent domain
ρ	density
ρ_0	(Boussinesq) mean density
σ	sigma coordinate or grid
τ	wind stress
ϕ	general variable (a tracer or one velocity component)
Φ	potential of vertical velocity
ω	angular velocity
Ω	model's physical domain
Ω^e	element e in the physical domain

Table B.2: Abbreviations

ACC	Antarctic Circumpolar Current
ALE	arbitrary Lagrangian Eulerian
BBL	bottom boundary layer
CBS	characteristic-based split
CG	characteristic-Galerkin
DSO	Denmark Strait Overflow
FCT	flux-corrected transport
FD	finite difference
FE	finite element
FV	finite volume
GLS	Galerkin least-squares
GM	Gent-Mcwilliams
OGCM	ocean general circulation model
PCT	pointwise-corrected transport
RMS	root mean square
SGS	subgrid scale
lhs	left-hand side
rhs	right-hand side

Bibliography

Adcroft, A., Hill, C., Marshall, J., 1997. Representation of topography by shaved cells in a height coordinate ocean model. Monthly Weather Review 125, 2293–2315.

Adcroft, A., Marshall, D., 1998. How slippery are piecewise-constant coastlines in numerical ocean models? Tellus Series a-Dynamic Meteorology and Oceanography 50, 95–108.

Arakawa, A., 1966. Computational design for long-term numerical integration of the equations of fluid motion: Two-dimensional incompressible flow. Part 1. Journal of Computational Physics 1, 119–143.

Babuska, I., 1973. The finite-element method with Lagrangian multipliers. Numerische Mathematik 20, 179–192.

Badia, S., Codina, R., 2006. Analysis of a stabilized finite element approximation of the transient convection-diffusion equation using an ALE framework. Siam Journal on Numerical Analysis 44, 2159–2197.

Beckmann, A., Döscher, R., 1997. A method for improved representation of dense water spreading over topography in geopotential-coordinate models. Journal of Physical Oceanography 27, 581–591.

Beckmann, A., Haidvogel, D. B., 1993. Numerical-simulation of flow around a tall isolated seamount 1. problem formulation and model accuracy. Journal of Physical Oceanography 23, 1736–1753.

Beckmann, A., Haidvogel, D. B., 1997. A numerical simulation of flow at Fieberling Guyot. Journal of geophysical research 102, 5595–5613.

Beckmann, A., Timmermann, R., Pereira, A. F., Mohn, C., 2001. The effect of flow at Maud Rise on the sea-ice cover - numerical experiments. Ocean dynamics 52, 11–25.

Blazek, J., 2001. Computational fluid dynamics: Principles and applications. Elsevier.

Bleck, R., 2002. An oceanic general circulation model framed in hybrid isopycnic-Cartesian coordinates. Ocean Modelling 4, 55–88.

Bleck, R., 2006. Ocean Weather Forecasting: An Integrated View of Oceanography. Springer, Ch. On the use of hybrid vertical coordinates in ocean circulation modeling, pp. 109–126.

Bleck, R., Smith, L. T., 1990. A wind-driven isopycnic coordinate model of the North and Equatorial Atlantic-Ocean 1. model development and supporting experiments. Journal of Geophysical Research-Oceans 95, 3273–3285.

Blumberg, A. F., Mellor, G. L., 1987. A description of a three-dimensional coastal ocean circulation model. In: Heaps, N. S. (Ed.), Three-Dimensional Coastal Ocean Models. Vol. 4 of Coastal and Estuarine Series. American Geophysical Union, pp. 1–16.

Borowski, D., Gerdes, R., Olbers, D., 2002. Thermohaline and wind forcing of a circumpolar channel with blocked geostrophic contours. Journal of Physical Oceanography 32, 2520–2540.

Brasseur, P. P., 1991. A variational inverse method for the reconstruction of general-circulation fields in the Northern Bering Sea. Journal of Geophysical Research-Oceans 96, 4891–4907.

Brezzi, F., 1974. Existence, uniqueness and approximation of saddle-point problems arising from Lagrangian multipliers. R. A. I. R. O. Anal. Numer. R2, 129–151.

Bruce, J. G., 1995. Eddies southwest of the Denmark Strait. Deep-Sea Research Part I - Oceanographic Research Papers 42, 13–29.

Bryan, K., 1969. A numerical method for the study of the circulation of the world ocean. Journal of Computational Physics 4, 347–376.

Campin, J. M., Goosse, H., 1999. Parameterization of density-driven downsloping flow for a coarse-resolution ocean model in z-coordinate. Tellus Series a-Dynamic Meteorology and Oceanography 51, 412–430.

Casulli, V., Walters, R. A., 2000. An unstructured grid, three-dimensional model based on the shallow water equations. International Journal For Numerical Methods In Fluids 32, 331–348.

Cenedese, C., Whitehead, J. A., Ascarelli, T. A., Ohiwa, M., 2004. A dense current flowing down a sloping bottom in a rotating fluid. Journal of Physical Oceanography 34, 188–203.

Chapman, D. C., Haidvogel, D. B., 1992. Formation of Taylor caps over a tall isolated seamount in a stratified ocean. Geophysical and Astrophysical Fluid Dynamics 64, 31–65.

Chapman, D. C., Haidvogel, D. B., 1993. Generation of internal lee waves trapped over a tall isolated seamount. Geophysical and Astrophysical Fluid Dynamics 69, 33–54.

Chassignet, E. P., Arango, H., Dietrich, D., Ezer, T., Ghil, M., Haidvogel, D. B., Ma, C. C., Mehra, A., Paiva, A. M., Sirkes, Z., 2000. DAMEE-NAB: the base experiments. Dynamics of Atmospheres and Oceans 32, 155–183.

Chen, C., Liu, H., Beardsley, R. C., 2003. An unstructured, finite volume, three-dimensional, primitive equation ocean model: Application to coastal ocean and estuaries. Journal of Atmospheric and Oceanic Technology 20, 159–186.

Chu, P. C., Fan, C. W., 1997. Sixth-order difference scheme for sigma coordinate ocean models. Journal of Physical Oceanography 27, 2064–2071.

Codina, R., Coppola-Owen, H., Nithiarasu, P., Liu, C. B., 2006. Numerical comparison of CBS and SGS as stabilization techniques for the incompressible navier-stokes equations. International Journal for Numerical Methods in Engineering 66, 1672–1689.

Codina, R., Soto, O., 1997. Finite element solution of the Stokes problem with dominating Coriolis force. Computer Methods in Applied Mechanics and Engineering 142, 215–234.

Codina, R., Vazquez, M., Zienkiewicz, O. C., 1998. A general algorithm for compressible and incompressible flows. Part III: The semi-implicit form. International Journal for Numerical Methods in Fluids 27, 13–32.

Codina, R., Zienkiewicz, O. C., 2002. CBS versus GLS stabilization of the incompressible Navier-Stokes equations and the role of the time step as stabilization parameter. Communications in Numerical Methods in Engineering 18, 99–112.

Cox, M. D., 1984. A primitive equation three-dimensional model of the ocean. Tech. rep., Geophysical Fluid Dynamics Laboratory.

Cox, M. D., 1987. Isopycnal diffusion in a z-coordinate ocean model. Ocean Modelling 74, 1–5.

Danabasoglu, G., McWilliams, J. C., 1995. Sensitivity of the global ocean circulation to parameterizations of mesoscale tracer transports. Journal of Climate 8, 2967–2987.

Danilov, S., Kivman, G., Schröter, J., 2004. A finite-element ocean model: principles and evaluation. Ocean Modelling 6, 125–150.

Danilov, S., Kivman, G., Schröter, J., 2005. Evaluation of an eddy-permitting finite-element ocean model in the North Atlantic. Ocean Modelling 10, 35–49.

Dietrich, D. E., 1998. Application of a modified Arakawa 'a' grid ocean model having reduced numerical dispersion to the Gulf of Mexico circulation. Dynamics Of Atmospheres And Oceans 27, 201–217.

Dietrich, D. E., Mehra, A., Haney, R. L., Bowman, M. J., Tseng, Y. H., 2004. Dissipation effects in North Atlantic Ocean modeling. Geophysical Research Letters 31.

Dobrindt, U., Schröter, J., 2003. An adjoint ocean model using finite elements: An application to the South Atlantic. Journal of Atmospheric and Oceanic Technology 20, 392–407.

Dupont, F., Straub, D. N., Lin, C. A., 2003. Influence of a step-like coastline on the basin scale vorticity budget of mid-latitude gyre models. Tellus Series a-Dynamic Meteorology and Oceanography 55, 255–272.

Durran, D. R., 1999. Numerical methods for wave equations in geophysical fluid dynamics. Springer.

Engelman, M. S., Sani, R. L., Gresho, P. M., 1982. The implementation of normal and or tangential boundary-conditions in Finite-Element codes for incompressible fluid-flow. International Journal for Numerical Methods in Fluids 2, 225–238.

Etling, D., Gelhardt, F., Schrader, U., Brennecke, F., Kuhn, G., d'Hieres, G. C., Didelle, H., 2000. Experiments with density currents on a sloping bottom in a rotating fluid. Dynamics Of Atmospheres And Oceans 31, 139–164.

Ezer, T., 1999. Decadal variabilities of the upper layers of the subtropical North Atlantic: An ocean model study. Journal of Physical Oceanography 29, 3111–3124.

Ezer, T., 2001. Can long-term variability in the Gulf Stream transport be inferred from sea level? Geophysical Research Letters 28, 1031–1034.

Ezer, T., 2005. Entrainment, diapycnal mixing and transport in three-dimensional bottom gravity current simulations using the Mellor-Yamada turbulence scheme. Ocean Modelling 9, 151–168.

Ezer, T., Arango, H., Shchepetkin, A. F., 2002. Developments in terrain-following ocean models: intercomparisons of numerical aspects. Ocean Modelling 4, 249–267.

Ezer, T., Mellor, G. L., 1997. Simulations of the Atlantic Ocean with a free surface sigma coordinate ocean model. Journal of Geophysical Research-Oceans 102, 15647–15657.

Ezer, T., Mellor, G. L., 2000. Sensitivity studies with the North Atlantic sigma coordinate Princeton Ocean Model. Dynamics of Atmospheres and Oceans 32, 185–208.

Ezer, T., Mellor, G. L., 2004. A generalized coordinate ocean model and a comparison of the bottom boundary layer dynamics in terrain-following and in z-level grids. Ocean Modelling 6, 379–403.

Farhat, C., Geuzaine, P., Grandmont, C., 2001. The discrete geometric conservation law and the nonlinear stability of ALE schemes for the solution of flow problems on moving grids. Journal of Computational Physics 174, 669–694.

Fix, G. J., 1975. Finite-element models for ocean circulation problems. Siam Journal on Applied Mathematics 29, 371–387.

Ford, R., Pain, C. C., Piggott, M. D., Goddard, A. J. H., de Oliveira, C. R. E., Umpleby, A. P., 2004a. A nonhydrostatic finite-element model for three-dimensional stratified oceanic flows. Part I: Model formulation. Monthly Weather Review 132, 2816–2831.

Ford, R., Pain, C. C., Piggott, M. D., Goddard, A. J. H., de Oliveira, C. R. E., Umpleby, A. P., 2004b. A nonhydrostatic finite-element model for three-dimensional stratified oceanic flows. Part II: Model validation. Monthly Weather Review 132, 2832–2844.

Formaggia, L., Nobile, F., 2004. Stability analysis of second-order time accurate schemes for ALE-FEM. Computer Methods in Applied Mechanics and Engineering 193, 4097–4116.

Frickenhaus, S., Hiller, W., Best, M., 2005. FoSSI: the family of simplified solver interfaces for the rapid development of parallel numerical atmosphere and ocean models. Ocean Modelling 10, 185–191.

Fringer, O. B., Gerritsen, M., Street, R. L., 2006. An unstructured-grid, finite-volume, nonhydrostatic, parallel coastal ocean simulator. Ocean Modelling 14, 139–173.

Gent, P. R., McWilliams, J. C., 1990. Isopycnal mixing in ocean circulation models. Journal of Physical Oceanography 20, 150–155.

Gent, P. R., Willebrand, J., McDougall, T. J., McWilliams, J. C., 1995. Parameterizing eddy-induced tracer transports in ocean circulation models. Journal of Physical Oceanography 25, 463–474.

Gerdes, R., 1993a. A primitive equation ocean circulation model using a general vertical coordinate transformation 1. Description and testing of the model. Journal of Geophysical Research-Oceans 98, 14683–14701.

Gerdes, R., 1993b. A primitive equation ocean circulation model using a general vertical coordinate transformation 2. Application to an overflow problem. Journal of Geophysical Research-Oceans 98, 14703–14726.

Gerdes, R., Köberle, C., Willebrand, J., 1991. The influence of numerical advection schemes on the results of ocean general circulation models. Climte dynamics 5, 211–226.

Girton, J. B., Sanford, T. B., 2003. Descent and modification of the overflow plume in the Denmark Strait. Journal of Physical Oceanography 33, 1351–1364.

Gnanadesikan, A., Griffies, S. M., Samuels, B. L., 2007. Effects in a climate model of slope tapering in neutral physics schemes. Ocean Modelling 16, 1–16.

Gorman, G. J., Piggott, M. D., Pain, C. C., de Oliveira, C. R. E., Umpleby, A. P., Goddard, A. J. H., 2006. Optimisation based bathymetry approximation through constrained unstructured mesh adaptivity. Ocean Modelling 12, 436–452.

Greatbatch, R. J., Li, G. Q., 2000. Alongslope mean flow and an associated upslope bolus flux of tracer in a parameterization of mesoscale turbulence. Deep-Sea Research Part I-Oceanographic Research Papers 47, 709–735.

Greatbatch, R. J., Mellor, G. L., 1999. An overview of coastal ocean models. In: Mooers, C. (Ed.), Coastal Ocean Prediction. Vol. 56 of Coastal and Estuarine Studies. American Geophysical Union, Washington, DC,, pp. 31–57.

Griffies, S. M., 1998. The Gent-Mcwilliams skew flux. Journal of Physical Oceanography 28, 831–841.

Griffies, S. M., 2004. Fundamentals of Ocean Climate Models. Princeton University Press.

Griffies, S. M., Böning, C., Bryan, F. O., Chassignet, E. P., Gerdes, R., Hasumi, H., Hirst, A., Treguier, A., Webb, D., 2000a. Developments in ocean climate modelling. Ocean Modelling 2, 123–192.

Griffies, S. M., Gnanadesikan, A., Pacanowski, R. C., Larichev, V. D., Dukowicz, J. K., Smith, R. D., 1998. Isoneutral diffusion in a z-coordinate ocean model. Journal of Physical Oceanography 28, 805–830.

Griffies, S. M., Pacanowski, R. C., Hallberg, R. W., 2000b. Spurious diapycnal mixing associated with advection in a z-coordinate ocean model. Monthly Weather Review 128, 538–564.

Haidvogel, D., Curchitser, E., Iskandarani, M., Hughes, R., Taylor, M., 1997. Global modeling of the ocean and atmosphere using the spectral element method. Atmosphere-Ocean 35, 505–531.

Haidvogel, D. B., Arango, H. G., Hedstrom, K., Beckmann, A., Malanotte-Rizzoli, P., Shchepetkin, A. F., 2000. Model evaluation experiments in the North Atlantic Basin: simulations in nonlinear terrain-following coordinates. Dynamics of Atmospheres and Oceans 32, 239–281.

Haidvogel, D. B., Beckmann, A., 1999. Numerical Ocean Circulation Modeling. Imperial College Press.

Haidvogel, D. B., Wilkin, J. L., Young, R., 1991. A semi-spectral primitive equation ocean circulation model using vertical sigma and orthogonal curvilinear horizontal coordinates. Journal of Computational Physics 94, 151–185.

Haine, T. W. N., Marshall, J., 1998. Gravitational, symmetric, and baroclinic instability of the ocean mixed layer. Journal of Physical Oceanography 28, 634–658.

Hallberg, R., 2000. Time integration of diapycnal diffusion and Richardson number-dependent mixing in isopycnal coordinate ocean models. Monthly Weather Review 128, 1402–1419.

Hallberg, R., Rhines, P., 1996. Buoyancy-driven circulation in an ocean basin with isopycnals intersecting the sloping boundary. Journal of Physical Oceanography 26, 913–940.

Haltiner, G. T., Williams, R. T., 1980. Numerical prediction and dynamic meteorology. John Wiley and Sons.

Ham, D. A., Pietrzak, J., Stelling, G. S., 2005. A scalable unstructured grid 3-dimensional finite volume model for the shallow water equations. Ocean Modelling 10, 153–169.

Haney, R. L., 1991. On the pressure-gradient force over steep topography in sigma coordinate ocean models. Journal of Physical Oceanography 21, 610–619.

Held, I. M., Schneider, T., 1999. The surface branch of the zonally averaged mass transport circulation in the troposphere. Journal of the Atmospheric Sciences 56, 1688–1697.

Holland, D. M., 2001a. Explaining the Weddel Polynya - a large ocean eddy shed at Maud Rise. Science 292, 1697–1700.

Holland, D. M., 2001b. Transient sea-ice polynya forced by environmental flow variability. Progress in Oceanography 48, 475–532.

Hughes, C. W., Killworth, P. D., 1995. Effects of bottom topography in the large-scale circulation of the Southern-Ocean. Journal of Physical Oceanography 25, 2485–2497.

Hughes, T., 1987. The finite element method. Prentice-Hall, Inc.

Iskandarani, M., Haidvogel, D. B., Levin, J. C., 2003. A three-dimensional spectral element model for the solution of the hydrostatic primitive equations. Journal of Computational Physics 186, 397–425.

Ivchenko, V. O., Zalesny, V. B., Drinkwater, M. R., Schröter, J., 2006. A quick response of the equatorial ocean to Antarctic sea ice/salinity anomalies. Journal of Geophysical Research-Oceans 111, C10018.

Jackett, D. R., McDougall, T. J., 1995. Minimal adjustment of hydrographic profiles to achieve static stability. Journal of Atmospheric and Oceanic Technology 12, 381–389.

Jiang, L., Garwood, R. W., 1996. Three-dimensional simulations of overflows on continental slopes. Journal of Physical Oceanography 26, 1214–1233.

Jungclaus, J. H., Hauser, J., Kase, R. H., 2001. Cyclogenesis in the Denmark Strait overflow plume. Journal of Physical Oceanography 31, 3214–3229.

Jungclaus, J. H., Mellor, G. L., 2000. A three-dimensional model study of the Mediterranean outflow. Journal of Marine Systems 24, 41–66.

Käse, R. H., Girton, J. B., Sanford, T. B., 2003. Structure and variability of the Denmark Strait Overflow: Model and observations. Journal of Geophysical Research 108, 3181.

Killworth, P. D., 2001. On the rate of descent of overflows. Journal Of Geophysical Research-Oceans 106, 22267–22275.

Killworth, P. D., Edwards, N. R., 1999. A turbulent bottom boundary layer code for use in numerical ocean models. Journal of Physical Oceanography 29, 1221–1238.

Kliem, N., 2004. A transport corrected finite element advection scheme. Ocean Modelling 7, 1–19.

Kliem, N., Pietrzak, J. D., 1999. On the pressure gradient error in sigma coordinate ocean models: A comparison with a laboratory experiment. Journal of Geophysical Research-Oceans 104, 29781–29799.

Kunze, E., Sanford, T. B., 1996. Abyssal mixing: Where it is not. Journal of Physical Oceanography 26, 2286–2296.

Kuzmin, D., 2000. A high-resolution finite element scheme for convection-dominated transport. Communications in Numerical Methods in Engineering 16, 215–223.

Kuzmin, D., Löhner, R., Turek, S., 2005. Flux-Corrected Transport. Scientific Computation. Springer, Berlin, subtitle: Principles, Algorithms, and Applications.

Kuzmin, D., Turek, S., 2002. Flux correction tools for finite elements. Journal of Computational Physics 175, 525–558.

Labeur, R. J., Pietrzak, J. D., 2005. A fully three dimensional unstructured grid non-hydrostatic finite element coastal model. Ocean Modelling 10, 51–67.

Ladyzhenskaya, O., 1969. Mathematical theory of viscous incompressible flows. Gordon and Breach Science Publishers.

Lane-Serff, G. F., Baines, P. G., 1998. Eddy formation by dense flows on slopes in a rotating fluid. Journal of Fluid Mechanics 363, 229–252.

Lane-Serff, G. F., Baines, P. G., 2000. Eddy formation by overflows in stratified water. Journal of Physical Oceanography 30, 327–337.

Large, W. G., Danabasoglu, G., Doney, S. C., McWilliams, J. C., 1997. Sensitivity to surface forcing and boundary layer mixing in a global ocean model: Annual-mean climatology. Journal of Physical Oceanography 27, 2418–2447.

Le Provost, C., Genco, M.-L., Lyard, F., 1995. Modeling and predicting tides over the World Ocean. In: Lynch, D., Davies, A. (Eds.), Quantitative skill assessment for coastal ocean models. Vol. 47 of Coastal and Estuarine Series. American Geophysical Union, pp. 175–201.

Le Roux, D. Y., Lin, C. A., Staniforth, A., 2000. A semi-implicit semi-Lagrangian finite-element shallow-water ocean model. Monthly Weather Review 128, 1384–1401.

Le Roux, D. Y., Staniforth, A., Lin, C. A., 1998. Finite elements for shallow water equation ocean models. Monthly Weather Review 126, 1931–1951.

Ledwell, J. R., Watson, A. J., Law, C. S., 1993. Evidence for slow mixing across the pycnocline from an open-ocean tracer-release experiment. Nature 364, 701–703.

Legg, S., Hallberg, R. W., Girton, J. B., 2006. Comparison of entrainment in over-flows simulated by z-coordinate, isopycnal and non-hydrostatic models. Ocean Modelling 11, 69–97.

Löhner, R., Morgan, K., Peraire, J., Vahdati, M., 1987. Finite-element flux-corrected transport (FEM-FCT) for the Euler and Navier-Stokes equations. International Journal for Numerical Methods in Fluids 7, 1093–1109.

Losch, M., Heimbach, P., 2007. Adjoint sensitivity of an ocean general circulation model to bottom topography. Journal of Physical Oceanography 37, 377–393.

Losch, M., Sidorenko, D., Beszczynska-Moller, A., 2005. FEMSECT: An inverse section model based on the finite element method. Journal of Geophysical Research-Oceans 110.

Lynch, D. R., Gray, W. G., 1979. Wave-equation model for finite-element tidal computations. Computers & Fluids 7, 207–228.

Lynch, D. R., Ip, J. T. C., Naimie, C. E., Werner, F. E., 1996. Comprehensive coastal circulation model with application to the Gulf of Maine. Continental Shelf Research 16, 875–906.

MacCready, P., Rhines, P. B., 2001. Meridional transport across a zonal channel: Topographic localization. Journal of Physical Oceanography 31, 1427–1439.

Maier-Reimer, E., Mikolajewicz, U., Hasselmann, K., 1993. Mean circulation of the hamburg LSG OGCM and its sensitivity to the thermohaline surface forcing. Journal of Physical Oceanography 23, 731–757.

Marshall, J., Adcroft, A., Hill, C., Perelman, L., Heisey, C., 1997. A finite-volume, incompressible Navier Stokes model for studies of the ocean on parallel computers. Journal of Geophysical Research-Oceans 102, 5753–5766.

McCalpin, J. D., 1994. A comparison of 2nd-order and 4th-order pressure-gradient algorithms in a sigma-coordinate ocean model. International Journal for Numerical Methods in Fluids 18, 361–383.

McDougall, T. J., 1987. Neutral surfaces. Journal of Physical Oceanography 17, 1950–1964.

McDougall, T. J., McIntosh, P. C., 2001. The temporal-residual-mean velocity. Part II: Isopycnal interpretation and the tracer and momentum equations. Journal of Physical Oceanography 31, 1222–1246.

Mellor, G., Häkkinen, S., Ezer, T., Patchen, R., 2002. A generalization of a sigma coordinate ocean model and an intercomparison of model vertical grids. In: Pinardi, N., Woods, J. (Eds.), Ocean Forecasting: Conceptual Basis and Applications. Springer, pp. 55–72.

Mellor, G. L., Ezer, T., Oey, L. Y., 1994. The pressure-gradient conundrum of sigma coordinate ocean models. Journal of Atmospheric and Oceanic Technology 11, 1126–1134.

Mellor, G. L., Oey, L. Y., Ezer, T., 1998. Sigma coordinate pressure gradient errors and the Seamount problem. Journal of Atmospheric and Oceanic Technology 15, 1122–1131.

Mellor, G. L., Yamada, T., 1982. Development of a turbulence closure-model for geophysical fluid problems. Reviews of Geophysics 20, 851–875.

Munk, W. H., Palmen, E., 1951. Note on dynamics of the Antarctic Circumpolar Current. Tellus 3, 53–55.

Nechaev, D., Schröter, J., Yaremchuk, M., 2003. A diagnostic stabilized finite-element ocean circulation model. Ocean Modelling 5, 37–63.

Nithiarasu, P., 2005. An arbitrary lagrangian eulerian (ALE) formulation for free surface flows using the characteristic-based split (CBS) scheme. International Journal for Numerical Methods in Fluids 48, 1415–1428.

Nithiarasu, P., Codina, R., Zienkiewicz, O. C., 2006. The Characteristic-Based Split (cbs) scheme - a unified approach to fluid dynamics. International Journal for Numerical Methods in Engineering 66, 1514–1546.

Olbers, D., Borowski, D., Volker, C., Wolff, J. O., 2004. The dynamical balance, transport and circulation of the Antarctic Circumpolar Current. Antarctic Science 16, 439–470.

Olbers, D., Lettmann, K., Timmermann, R., 2007. Six circumpolar currents - on the forcing of the Antarctic Circumpolar Current by wind and mixing. Ocean Dynamics 57, 12–31.

Özgökmen, T. M., Chassignet, E. P., Paiva, A. M., 1997. Impact of wind forcing, bottom topography, and inertia on midlatitude jet separation in a quasigeostrophic model. Journal of Physical Oceanography 27, 2460–2476.

Pacanowski, R. C., Gnanadesikan, A., 1998. Transient response in a z-level ocean model that resolves topography with partial cells. Monthly Weather Review 126, 3248–3270.

Pacanowski, R. C., Philander, S. G. H., 1981. Parameterization of vertical mixing in numerical-models of tropical oceans. Journal of Physical Oceanography 11, 1443–1451.

Pain, C. C., Piggott, M. D., Goddard, A. J. H., Fang, F., Gorman, G. J., Marshall, D. P., Eaton, M. D., Power, P. W., de Oliveira, C. R. E., 2005. Three-dimensional unstructured mesh ocean modelling. Ocean Modelling 10, 5–33.

Papadakis, M. P., Chassignet, E. P., Hallberg, R. W., 2003. Numerical simulations of the Mediterranean sea outflow: impact of the entrainment parameterization in an isopycnic coordinate ocean model. Ocean Modelling 5, 325–356.

Penduff, T., Barnier, B., Kerbiriou, M. A., Verron, J., 2002. How topographic smoothing contributes to differences between the eddy flows simulated by sigma- and geopotential-coordinate models. Journal of Physical Oceanography 32, 122–137.

Persson, P. O., Strang, G., 2004. A simple mesh generator in MATLAB. Siam Review 46, 329–345.

Phillips, N. A., 1957. A coordinate system having some special advantages for numerical forecasting. Journal of Meteorology 14, 184–185.

Pietrzak, J., Jakobson, J. B., Burchard, H., Jacob Vested, H., O., P., 2002. A three-dimensional hydrostatic model for coastal and ocean modelling using a generalised topography following co-ordinate system. Ocean Modelling 4, 173–205.

Platzman, G. W., 1981. Some response characteristics of finite-element tidal models. Journal of Computational Physics 40, 36–63.

Price, J. F., Baringer, M. O., 1994. Outflows and deep-water production by marginal seas. Progress in Oceanography 33, 161–200.

Rannacher, R., 1992. On chorin projection method for the incompressible Navier-Stokes equations. Lecture Notes in Mathematics 1530, 167–183.

Redi, M. H., 1982. Oceanic isopycnal mixing by coordinate rotation. Journal of Physical Oceanography 12, 1154–1158.

Rhines, P., 1970. Edge-, Bottom-, and Rossby waves in a rotating stratified fluid. Geophysical Fluid Dynamics 1, 273–302.

Schlichtholz, P., Houssais, M. N., 1999. An inverse modeling study in Fram Strait. Part I: dynamics and circulation. Deep-Sea Research Part II-Topical Studies in Oceanography 46, 1083–1135.

Send, U., Marshall, J., 1995. Integral effects of deep convection. Journal of Physical Oceanography 25, 855–872.

Shchepetkin, A. F., McWilliams, J. C., 2003. A method for computing horizontal pressure-gradient force in an oceanic model with a nonaligned vertical coordinate. Journal of Geophysical Research-Oceans 108 (C3), 3090.

Shewchuk, J., 1996. Triangle: Engineering a 2D Quality Mesh Generator and De-
    launay Triangulator. In: Lin, M., Manocha, D. (Eds.), Applied Computational
    Geometry: Towards Geometric Engineering. Vol. 1148 of Lecture Notes in Com-
    puter Science. Springer-Verlag, pp. 203–222.
    URL `http://www.cs.cmu.edu/~quake/triangle.html`

Song, Y. H., Haidvogel, D., 1994. A semiimplicit ocean circulation model using a
    generalized topography-following coordinate system. Journal of Computational
    Physics 115, 228–244.

Song, Y. T., 1998. A general pressure gradient formulation for ocean models. Part I:
    Scheme design and diagnostic analysis. Monthly Weather Review 126, 3213–3230.

Song, Y. T., Chao, Y., 2000. An embedded bottom boundary layer formulation for
    z-coordinate ocean models. Journal of Atmospheric and Oceanic Technology 17,
    546–560.

Song, Y. T., Wright, D. G., 1998. A general pressure gradient formulation for ocean
    models. Part II: Energy, momentum, and bottom torque consistency. Monthly
    Weather Review 126, 3231–3247.

Spall, M. A., 2004. Boundary currents and watermass transformation in marginal
    seas. Journal of Physical Oceanography 34, 1197–1213.

Spall, M. A., Price, J. F., 1998. Mesoscale variability in Denmark Strait: The PV
    outflow hypothesis. Journal of Physical Oceanography 28, 1598–1623.

Stuhne, G. R., Peltier, W. R., 2006. A robust unstructured grid discretization for 3-
    dimensional hydrostatic flows in spherical geometry: A new numerical structure
    for ocean general circulation modeling. Journal of Computational Physics 213,
    704–729.

Tansley, C. E., Marshall, D. P., 2000. On the influence of bottom topography and the
    Deep Western Boundary Current on Gulf Stream separation. Journal of Marine
    Research 58, 297–325.

Treguier, A. M., Held, I. M., Larichev, V. D., 1997. Parameterization of quasi-
    geostrophic eddies in primitive equation ocean models. Journal of Physical
    Oceanography 27, 567–580.

Tseng, Y. H., Dietrich, D. E., 2006. Entrainment and transport in idealized three-
    dimensional gravity current simulation. Journal of Atmospheric and Oceanic Tech-
    nology 23, 1249–1269.

Visbeck, M., Marshall, J., Jones, H., 1996. Dynamics of isolated convective regions
    in the ocean. Journal of Physical Oceanography 26, 1721–1734.

Walters, R. A., 2005. Coastal ocean models: two useful finite element methods.
    Continental Shelf Research 25, 775–793.

Walters, R. A., 2006. Design considerations for a finite element coastal ocean model. Ocean Modelling 15, 90–100.

Walters, R. A., Werner, F. E., 1989. A comparison of two finite element models of tidal hydrodynamics using a North Sea data set. Advances in Water Resources 12, 184–193.

White, L., Deleersnijder, E., Legat, V., 2007. A three-dimensional unstructured mesh finite element marine model, with application to the flow around a shallow-water island. Journal of Geophysical Research submitted.

Willebrand, J., Barnier, B., Boning, C., Dieterich, C., Killworth, P. D., Le Provost, C., Jia, Y. L., Molines, J. M., New, A. L., 2001. Circulation characteristics in three eddy-permitting models of the North Atlantic. Progress In Oceanography 48, 123–161.

Winton, M., Hallberg, R., Gnanadesikan, A., 1998. Simulation of density-driven frictional downslope flow in z-coordinate ocean models. Journal of Physical Oceanography 28, 2163–2174.

Zienkiewicz, O. C., Nithiarasu, P., Codina, R., Vazquez, M., Ortiz, P., 1999. The Characteristic-Based-Split procedure: An efficient and accurate algorithm for fluid problems. International Journal for Numerical Methods in Fluids 31, 359–392.

Zienkiewicz, O. C., Taylor, R. L., 2000. The finite element method, 5th Edition. Vol. 3: Fluid Dynamics. Butterworth-Heinemann.

Acknowledgements